Compressible DNS studies of the boundary layer on a low pressure turbine blade at high incidence

A Thesis

Submitted for the Degree of

DOCTOR OF PHILOSOPHY

by

RAJESH RANJAN

ENGINEERING MECHANICS UNIT
JAWAHARLAL NEHRU CENTRE FOR ADVANCED SCIENTIFIC RESEARCH
(A Deemed University)
Bangalore – 560 064

November 2015

The missing 54

~~~

अनेकसंशयोच्छेदि, परोक्षार्थस्य दर्शकम् ।
सर्वस्य लोचनं शास्त्रं, यस्य नास्ति अन्धैव सः ॥

- हितोपदेश: (~ १४ वीं शती)

It shatters many doubts, reveals what is hidden -
Science is everyone's eye: without it is like being blind.

- Hitopadeśa (~14th Century)

~~~

DECLARATION

I hereby declare that the matter embodied in the thesis entitled "**Compressible DNS studies of the boundary layer on a low pressure turbine blade at high incidence**" is the result of investigations carried out by me at the Engineering Mechanics Unit, Jawaharlal Nehru Centre for Advanced Scientific Research, Bangalore, India under the supervision of **Prof. Roddam Narasimha** and **Prof. S. M. Deshpande**, and that it has not been submitted elsewhere for the award of any degree or diploma.

In keeping with the general practice in reporting scientific observations, due acknowledgment has been made whenever the work described is based on the findings of other investigators.

Rajesh Ranjan

CERTIFICATE

We hereby certify that the matter embodied in this thesis entitled "**Compressible DNS studies of the boundary layer on a low pressure turbine blade at high incidence**" has been carried out by **Mr. Rajesh Ranjan** at the Engineering Mechanics Unit, Jawaharlal Nehru Centre for Advanced Scientific Research, Bangalore, India under our supervision and that it has not been submitted elsewhere for the award of any degree or diploma.

Prof. Roddam Narasimha	**Prof. S. M. Deshpande**
(Research Supervisor)	(Research Co-supervisor)

Acknowledgements

A few words are not enough to acknowledge all the people, with whom I have spent the peak of my youth. I will, however, make an attempt to present a token of appreciation to those who helped me in shaping my thoughts, my personality and my professional career.

First and foremost, I would like to express my sincere gratitude to my research supervisor and a great mentor **Prof. Roddam Narasimha** for his excellent guidance without whose support I cannot imagine having come this far. I admire his passion, scientific brilliance, pragmatic and clear thinking, and his sincere devotion towards science and technology. I feel extremely grateful to have got this opportunity to share the space and time with a great personality like him. His infallible optimism and great love for the nation is an inspiration to many like me. If I have to give one reason for taking so long to finish Ph.D., I would say because I wanted to learn as much as I can from the knowledge, insights and experience from Prof. Narasimha.

I greatly acknowledge my co-supervisor **Prof. S.M. Deshpande** for his support and timely guidance. I thoroughly enjoyed our fruitful scientific as well as other useful discussions during several tea breaks. His approach to explaining a complex problem through simple (sometimes humorous) examples leave a long lasting impact. It has been a fantastic journey working with you, Sir.

This research work would not have taken this shape without the financial support of **GATET** at **GTRE**. My sincere thanks to their members for appreciating the potential of the problem and providing the much-needed support.

It is a pleasure to express my gratitude to **Prof. Wolfgang Rodi, Dr. Jan Wissink** and **Mr. Stephan Stotz** for providing crucial data pertaining to the present work.

I sincerely acknowledge **Dr. Sukumar Chakravarthy** and his team for providing the CFD++ license and valuable technical support. The thesis would have been incomplete without their generous support.

The whole scientific journey would not have been feasible without the support from **CSIR-4PI (Bangalore)** and **C-DAC (Pune)**. I have used their supercomputers exhaustively for massive computations. I would like to express my sincere gratitude to their support staffs.

I would also like to thank all the eminent professors who taught me scientific courses. **Prof. Rama Govindarajan, Prof. Santosh Ansumali, Prof. Ganesh Subramanian, Dr. Kavita Jain, Prof. O.N. Ramesh, Prof. Joseph Matthew** and **Prof. Raghuram Govardhan** have excellently taught me relevant courses and prepared me for this journey. I am amazed by the amount of effort they put in preparing for the courses. Prof. Ramesh also gave me valuable comments and suggestions pertaining to my work. Rama's absence in EMU was always felt. Thanks are due to **Prof. K R Sreenivas**, and **Prof. Meheboob Alam** for their overall help, support and encouragement and their efforts to keep the EMU environment conducive to research.

I thank **Dr. Sunil Sherlekar** for his care and constant enquiry about my career and plans. My association with him is long since Computational Research Laboratories (CRL) days.

It was my great pleasure to interact with the people from **ANURAG, Cray, Intel, Nvidia** and **Calligo Technologies**, who have expressed their interest in my research work. I would like to thank them for the useful interactions.

This section would not be complete without thanking my friends and colleagues who made me feel at home away from home. It was a great fun interacting with **Saikishan, Aarthi, Ponnu, Navaneeth, Jose, Rohith, Croor, Prasanth, Anubhab, Senjuti, Rakshith, Milind, Vybhav, Saurabh, Sachin, Samrat, Srikanth, Vicky, Deepthi, Siddharth, Deepak, Kanwar, Chakri, Ujjayan and Sankalp**. I thoroughly enjoyed those long hours of scientific as well as ideological debates. Special thanks to Saikishan for conferring 'gentlemanship' to me and also helping me with some of the analyses. Ponnu though always opposed the 'gentlemanship' to me, she has always been kind and helping.

I would also like to thank **Manaswini, Vini, Priyanka, Darshana, Pavitra, Arpit, Piyush** for all the amazing dinners and get-togethers that we had. Special thanks to Manaswini for providing me delicious Oriya food (especially dahi-baigan) and for her help with sketches that appeared in the second issue of JNC student magazine Fingerprints.

I have a long list of friends outside JNC who I am thankful to, for their regular encouragement and support in finishing my Ph.D.. From the list, **Bunty, Jagat, Nivedita and Isha** deserve special mention.

A note of acknowledgement to **Big Bang Theory, Ph.D. Comics, Chirstopher Nolan, Indian politicians** (for their mostly silly statements) and **friends in social media**, who helped me in keeping the stress away.

I would also like to thank all the concerned **JNC staff members** for all their help in enabling me to have a trouble-free life both in the hostel and in the campus. **Chandriah** deserves a special mention for the excellent food in canteen.

My sincere thanks to **Gayatri Pariwar** for inculcating positivity inside me, and for the constant inspiration to serve the humanity selflessly. I would to like specially thank a few *parijans:* **Amitabh bhaiya, Ashutosh ji, Somonath bhaiya, Rajiv bhaiya, Madhuri di, Jateen bhaiya, Ravi bhaiya, Neeta tai, Vaishali di, Bhawna di, Ashwini bhaiya, Anil bhaiya, Ashish, Netram, Rohit, and Archana,** with whom I have worked closely on various social projects.

Thanks to **Sarjana family** for keeping the poet inside me alive and awake. I feel fortunate to be in the day-to-day discussions of **Saurabh Sir, Santosh Sir** and **Deepak**, who are like family members to me.

I owe a debt of gratitude to my **parents**, my siblings - **Rakesh and Alpana**, in-laws- **Poonam and Rajesh**, and **rest of the family**. I am proud to mention that without their constant support, encouragement and patience, this journey of five long years would not have been possible. I can only imagine how my father would have answered this recurring question: *Did your son really leave an excellent job to pursue a Ph.D. in India?* I admire his patience and his trust on me. My mother and siblings wanted to see me often. I have not spent more than 50 days with them in last 5 years.

My nephew **Gulshan** and niece **Srishti** deserve a special mention for keeping the child-hood inside me alive. In the moments of stress, it was relaxing to talk to my little niece **Gargi**.

My **in-laws** were extremely supportive and patient when I was writing this thesis. I would like to thank them for trusting me.

Last but not the least, I would like thank my wife **Deepti** for always being there beside me. Her love and care are unmatched. Writing thesis immediately after the wedding is probably not a splendid idea, so I also thank her for the patience.

Finally, I take this opportunity to thank everyone else whom I may have forgotten to personally mention for being an important part of this journey.

Two excellent people with whom I have closely worked- My master's guide **Prof. P J Paul**, and my head at CRL **Dr. Rajendra Lagu** have left untimely for the heavenly abode during my Ph.D. I pay my heartfelt tributes to these wonderful human beings.

India has seen many wars since independence. While it is sad to know about the precious lives from both the sides suffered in such unfortunate wars, I often think about the soldiers and officers of armed forces who go 'missing' after the war is over. This thesis is dedicated to the ***The missing 54***- the missing soldiers/officers whose fates are unknown since 1971 Indo-Pak war.

Abstract

It has been well known for many years that the flow past a turbine blade exhibits a rich variety of boundary layer phenomena, including all the problems that have been accepted as beyond the capability of current turbulence models. These problems include, in particular, transition, relaminarization, and separation; interestingly all three of them may occur simultaneously on the same blade under certain conditions. It therefore seemed worthwhile to investigate how many of the flow properties/characteristics of the turbine blade, especially within the boundary layer, can be captured by DNS.

In this context, the thesis attempts to address the following issues that were found to be important after an extensive literature survey of the field:

- Numerical Issues
  - Accounting for compressibility
  - Addressing skewed-grid concerns near the boundary layer
  - Grid convergence, spatial and temporal resolution
- Fluid-dynamical Issues
  - Effect of high surface curvature on boundary layer flow
  - The behaviour of separation bubbles (if there should be any)
  - Assessment of current DNS results with prevailing theories
  - Characteristics of the turbulent fluctuations in wall shear stress
  - Assessment of RANS and LES results with present DNS results
- Technological Issues
  - Computation of accurate surface pressure distribution
  - Interactions between tripping, transition, relaminarization and retransition
  - Analysis of skin friction and heat transfer fluctuations

The present focus on the boundary layer flow on turbine blades is desirable as it has not received much attention; instead, flow in the passage between successive blades in a stage has been of major concern in most earlier studies. To obtain reliable boundary layer data, a new hybrid grid is used for simulations on the blades, with a fine boundary layer grid on the wall and a general hexahedral grid for the rest of the passage. To the best knowledge of the author, this is the first such boundary layer study using a compressible DNS code.

The new DNS code, named *ANUROOP* (meaning resembling or concordant in Sanskrit, copyright in progress), has been developed in the thesis specially for the purpose. ANUROOP solves 3D compressible Navier-Stokes equations in 3D space and time. It is developed in a finite-volume framework to ensure conservation of relevant quantities as well as compatibility with computational domains in complicated geometries. Second order central differencing based on a kinetic-energy preserving scheme is used for the flux calculation, as it is found to be more robust and has less aliasing error. Boundary conditions based on characteristics are used at the inflow and outflow boundaries to ensure smooth flow. A relaminarized buffer layer (also called 'viscous padding') is used in the vicinity of the outflow from the computational domain to prevent fluctuations due to physical instabilities of the flow. The code is parallelised with standard MPI with optimised communication.

The code has been verified and validated extensively against various free-shear as well as wall-bounded flows, including the Taylor-Green vortex flow, the Sod shock tube problem, and forced, fully developed supersonic turbulent channel flow.

ANUROOP has then been used to simulate flow past the low pressure turbine (LPT) blade T106A at Reynolds number $Re = 51831$ (based on the inlet velocity and axial chord length) and Mach number$M = 0.1$, for which test data are available from Stadtmuller (2002*a*). A typical flow passage between two neighbouring blades was taken as the computational domain, with periodic boundary conditions in the chord-normal and spanwise directions.

The study has yielded the following important insights into LPT blade flow dynamics:

- The grid sensitivity study (with the number of grid elements varying from 25 to 160 million) suggests that streamwise resolution near the high surface curvature region has a significant effect on the computed flow. For example, even a fundamental bulk parameter such as the pressure distribution on the blade surface was found be sensitive to resolution. This suggests a strong coupling between the boundary layer and outer flows.

- Very close to the leading edge, the curvature is too high for Prandtl's boundary layer theory to be applicable. DNS results in this region were then compared against higher

order boundary layer theory that includes the curvature effect and good agreement was found.

- The low and medium resolution simulations predict a single mean 'short' separation bubble both near the leading and trailing edges of the suction side. The total velocity contours for these simulations show multiple transitions on the suction side of the blade where the flow is relatively much more complex than on the pressure side. The flow becomes transitional after the leading edge separation, but it never becomes fully turbulent with the intermittency reaching upto 0.9. The favourable pressure gradient downstream relaminarizes the flow. In the relaminarization region of the blade, DNS results compare favourably with the two-layer quasi-laminar theory.

- For the highest resolution simulation, the leading edge separation bubble on the suction side disappears and the flow remains laminar till it separates near the trailing edge to form a 'long' mean separation bubble.

From an engineering perspective, the peak heat flux for instantaneous flow is found to be significantly higher than the mean value in the transition region. RANS simulations and LES were also performed for the same flow using the available commercial code CFD++. The RANS calculations without the presence of transition models do not at all predict separation in this current set-up. Simulations with Langtry and Menter's $\gamma - Re_\theta$ model provide better predictions of the flow but are substantially different from the experiment, particularly on the suction side where the flow is quite complex. Results with hybrid RANS/LES simulations however are promising, and such tools can be useful in engineering applications.

The story of a flow journey

This is the story of a remarkable journey
that she embarked on in her life-
Despite coming from a 'rough' background,
she looked quite polite.

When she started ascent on a blade,
it was low Reynolds number-
She didn't know what was coming,
but it only made her stronger.

Oh! how hard was the tiresome task
climbing up a curved wall-
But she took all the needed care,
so she doesn't get a 'stall'.

But before she could go much farther,
her journey reached a difficult stage-
She got thrown away from the wall,
as she crossed the leading edge.

All the eye-witnesses said
It was due to adverse pressure-
But the thing all of them did ignore
Was the presence of high curvature.

Determined to finish her journey
she waited for the 'gradient' to fall-
And after several failed attempts
she got reattached to the wall.

But I am very sorry to say
she was no longer the same kind
Recent struggles made her perturbed
and she now had a 'turbulent' mind.

What a 'transition' that was!
unimaginable was her anger-
The heat flux jumping all of five times,
skin-friction also surging in number.

Thank God for the next stage,
where the pressure ahead got favourable-
And the intermittency went down so,
that she looked now pretty stable.

She had completed most of her journey,
before she began to stumble-
Tripped again by adverse pressure
she fell into another 'bubble'.

And it was the same story once again-
Disturbances, fluctuations, transition-
But she completed her arduous journey,
shining with bravery and aspiration.

That's the story about her so far,
but the journey is never complete-
She is now a wavy 'wake',
set to achieve yet another feat.

...

Now if you are sitting in a plane,
and this story is chilling your spine-
Just look outside your window
all of it is happening in your LP turbine.
.....

Table of contents

List of figures

List of tables

Nomenclature

Roman Symbols

B	Body force
P	Pitch of the blade
S	Span of the blade
K	Launder's Pressure gradient parameter = $\frac{\nu}{U(x)^2}\frac{\mathrm{d}\,U(x)}{\mathrm{d}\,x}$
k	Thermal conductivity
P	Pressure gradient parameter = $\frac{h^2}{\nu}\ \frac{\Delta u}{\Delta x}$
c	Speed of sound
e	Internal Energy
E	Energy
f	Flux
E	Total energy
L	Length
l	Chord length of the blade
p	Pressure
q	Heat Flux
T	Temperature
V	Velocity

R	Specific gas constant
M	Mach number
Nu	Nusselt number
Pr	Prandtl number
Re	Reynolds number
s	Distance along the chord
H	Shape factor = $\delta^\star/\theta$
t	Time
x, y, z	Streamwise,wall-normal and spanwise global coordinates

Greek Symbols

α	Angle of attack
α_s	Aspect ratio of 2D shock tube
α_T	Temperature ratio between free-stream and wall
β_1	Incidence angle for blade
δ	Boundary Layer Thickness
$\delta^\star$	Displacement thickness of the boundary layer
β_{geo}	Geometric incidence angle for blade
β_s	Stagger angle
θ	Momentum Thickness
Ω	Computational Cell Volume
Γ	Cell Area
Δ	Interval
η	Distance normal to the chord
ε	Dissipation rate of turbulent kinetic energy

γ	Gas Constant = c_p/c_v
γ	Intermittency
κ	Curvature
Λ	Spectral radius
λ	Eigen values
Λ_p	Pressure gradient parameter = $-\frac{dp}{dx}\frac{\delta}{\tau_0}\frac{h^2}{\nu}\ \frac{\Delta u}{\Delta x}$
μ	Dynamic viscosity
ν	Kinematic viscosity
ω	Vorticity
Φ	Viscous heat generation rate
π	$\simeq 3.14\ldots$
ψ	Riemann Invariants
ρ	Fluid density
τ	Viscous stress tensor

Superscripts

$.^\star$	Dimensional quantity
$\bar{.}$	Mean quantity
$.'$	Fluctuating quantity
$\tilde{.}$	Favre-averaged quantity
$.''$	Favre fluctuations
$.^+$	Quantity in wall units

Subscripts

$._{bf}$	Boundary Face
$._f$	Face

$\cdot_\infty$ Free-stream Quantity

$\cdot_\infty$ Free Stream

$\cdot_{inv}$ Inviscid

$\cdot_L$ Left

$\cdot_\perp$ Normal

$\cdot_R$ Right

$\cdot_{ref}$ Reference Values

$\cdot_v$ Viscous

$\cdot_c$ Centerline

$\cdot_{VD}$ van-Driest Transformation

$\cdot_g$ Ghost Cell

$\cdot_{rms}$ Root-Mean-Square of a variable

$\cdot_w$ Wall

Other Symbols

c_f Co-efficient of friction

c_p Co-efficient of pressure

δ_{ij} Kronecker delta

$\Delta s^+, \Delta\eta^+, \Delta z^+$ Grid spacing in wall units in streamwise,wall-normal and spanwise directions

Δt Time-step

s_i^o Entropy of species i

h_i Enthalpy of species i

k_t Turbulent kinetic energy defined as $\overline{u_i u_i}/2$

l_{ax} Axial chord length

M_τ Friction Mach number $= \frac{u_\tau}{\langle a_w \rangle}$

M_c Centerline Mach number

∇ Gradient operator

$\nabla.$ Divergence operator

Q_j Total enthalpy

Re_τ Reynolds number based $\langle \rho_w \rangle$ and u_τ

Re_c Centerline Reynolds number

S_k Sutherland's constant for thermal conductivity

S_μ Sutherland's constant for viscosity

τ_w Wall shear stress

l_t Turbulent length scale

u_t Turbulent velocity scale

μ_t Turbulent eddy viscosity

u_τ Friction velocity $= \sqrt{\frac{\tau_w}{\langle \rho_w \rangle}}$

u_i Cartesian velocity component in i^{th} direction

U_t Velocity tangential to the wall as distance Δy

x_i Cartesian axis in i^{th} direction (x, y, z)

y^+ Non-dimensional wall distance

$\langle \phi \rangle$ Mean of ϕ

Acronyms / Abbreviations

$1D$ One Dimensional

$2D$ Two-dimensional in Mean

$2d$ Two-dimensional in Fluctuations

$3D$ Three-dimensional in Mean

$3d$ Three-dimensional in Fluctuations

BL Boundary Layer

LE Leading Edge

TE Trailing Edge

CDF Cumulative Distribution Function

$DDES$ Delayed Detached Eddy Simulation

DES Detached Eddy Simulation

DNS Direct Numerical Simulation

LES Large Eddy Simulation

$FSTI$ Free-Stream Turbulence Intensity

FVM Finite Volume Method

GG Green-Gauss

HPC High Performance Computing

HPT High Pressure Turbine

$JNCASR$ Jawaharlal Nehru Centre for Advanced Scientific Research

KEP Kinetic Energy Preserving

$KFVS$ Kinetic Flux Vector Splitting

LPT Low Pressure Turbine

MPI Message Passing Interface

ODE Ordinary Differential Equation

PDE Partial Differential Equation

PDF Probability Density Function

$RANS$ Reynolds Averaged Navier-Stokes

SR Successive Ratio

TVD Total Variation Diminishing

Chapter 1

Introduction, Background and Motivation

The gas turbine is an integral part of the power generation system in most of the aviation industry. The overall efficiency of an engine depends chiefly on the efficiency of the gas-turbine, which in turn depends on efficient blade designs. According to a recent report by Jahanmiri (2011), a 1% improvement in the efficiency of a low pressure turbine (LPT) results in savings of about USD52,000 per year on a typical airliner.

The turbo-machinery industry strives to increase turbine blade loading in order to reduce weight and total cost. It has been constantly realized that lack of proper understanding of the complicated flow over these blades is impeding efforts to improve the aero-dynamic design of blades. Also the life of a turbine blade is directly related to the fluctuating heat transfer rates on its surface. Based on a report by Reed (1985), Narasimha (1991) notes that a 25% difference in heat transfer rates on a turbine blade can mean an order of magnitude difference to its life. Moreover, one study shows that as much as 70% on the suction side of a typical turbine blade could be transitional (Narasimha 1991). This phenomenon is directly related to the instantaneous peak heat transfer rate on a blade, which in turn is related to the life of the blade and the efficiency of the gas-turbine in general. These observations make flow past a blade, especially in the harsh and highly disturbed environment characteristic of turbomachinery, a crucial problem in fluid-dynamics that needs to be understood.

1.1 The Turbine Blade as Fluid-dynamical Zoo

Figure 1.1 (due to J. Coupland, from an untraceable reference), shows the sketch of typical fluid-dynamical phenomena that may occur in the harsh environment of a turbine blade.

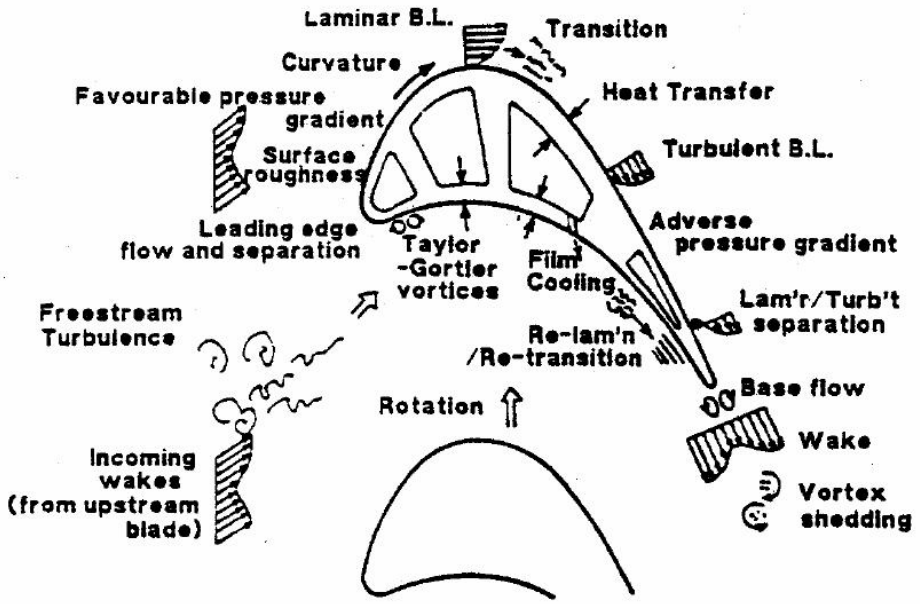

Fig. 1.1 The Turbine Blade as Fluid-dynamical Zoo

Depending on the shape, camber and curvature of the blade, we see these phenomena occurring on the blade under different working conditions (Mayle 1991; Hodson & Howell 2005). Of these, separation, transition and relaminarization have been recognized as major challenges not yet met by current turbulence models (Spalart 2015); all of these may occur jointly or separately on an LPT blade. We briefly describe each of these phenomena below.

Separation

Boundary layer separation is one of the most striking phenomena on flows in the LPT blades. A boundary layer may separate in an adverse pressure gradient region if the near wall fluid does not have sufficient momentum to overcome it.

The mode of separation on a blade depends on whether the upstream flow is laminar or transitional. Usually in transitional mode separation, reattachment is accelerated due to vortex-shedding and transitional shear layer. Laminar mode separation may occur in separation bubbles, classified as 'short' or 'long' based on its effect on the pressure distribution (Gaster 1969). As shown in Fig. 1.2, unlike a long bubble, a short bubble has only local effect and does not alter the rest of the pressure distribution. Short bubbles occur at moderate Reynolds number (*Re*) and mild adverse pressure gradients (and hence vortex-shedding is sufficient to bring reattachment), whereas long bubbles require low *Re* and strong adverse pressure gradients.

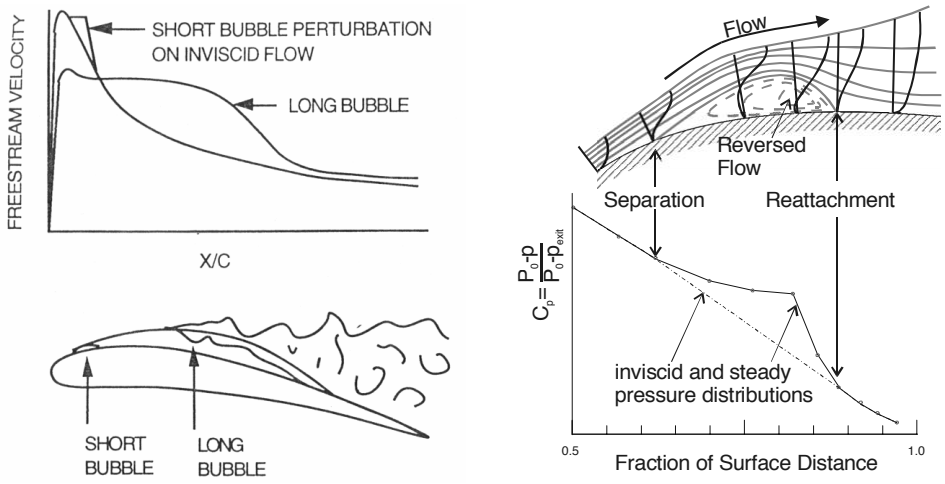

Fig. 1.2 Left: Short and long separation bubbles (reproduced from Malkiel & Mayle (1995)). Right: Schematic of short separation bubble plotted on measured static pressure coefficient in aft region of T106 blade suction surface (reproduced from Hodson & Howell (2007))

In an LP turbine, short bubbles are predominantly present. As reported in Hodson & Howell (2007), for a high lift turbine blade (such as T106), short bubble may occur in the aft region of the suction side for $10^5 \leq Re \leq 4 \times 10^5$. At lower Re, the blade is susceptible to long separation.

Some designers prefer a 'short' bubble at the LE to make the downstream flow transitional and hence avoid the greater losses due to possible long laminar separation in the aft region of the blade. Separation-induced-transition is another area of active research, and is seen as a challenge for the numerical modelling community working with turbulence and transition models.

Transition

Laminar-turbulent transition of the boundary layer is an important phenomenon that occurs on a turbine blade. Narasimha & Dey (1989) have presented schematic diagram of the various stages of natural transition from laminar to turbulent flow on a flat plate as shown in Fig. 1.3. The first sign of transition to turbulence is 2-D instability (Tollmien-Schlichting waves) followed by 3-D instability. The 3D instabilities were first discovered by Klebanoff *et al.* (1962) in the form of spanwise waviness in the amplitude. The theory for this instability was proposed by Herbert (1984) who showed that a laminar BL carrying relatively high amplitude T-S waves, would experience a new instability through the appearance of transverse harmonic variations of disturbance amplitude. These transverse waves develop into hairpin eddies (lambda vortices).

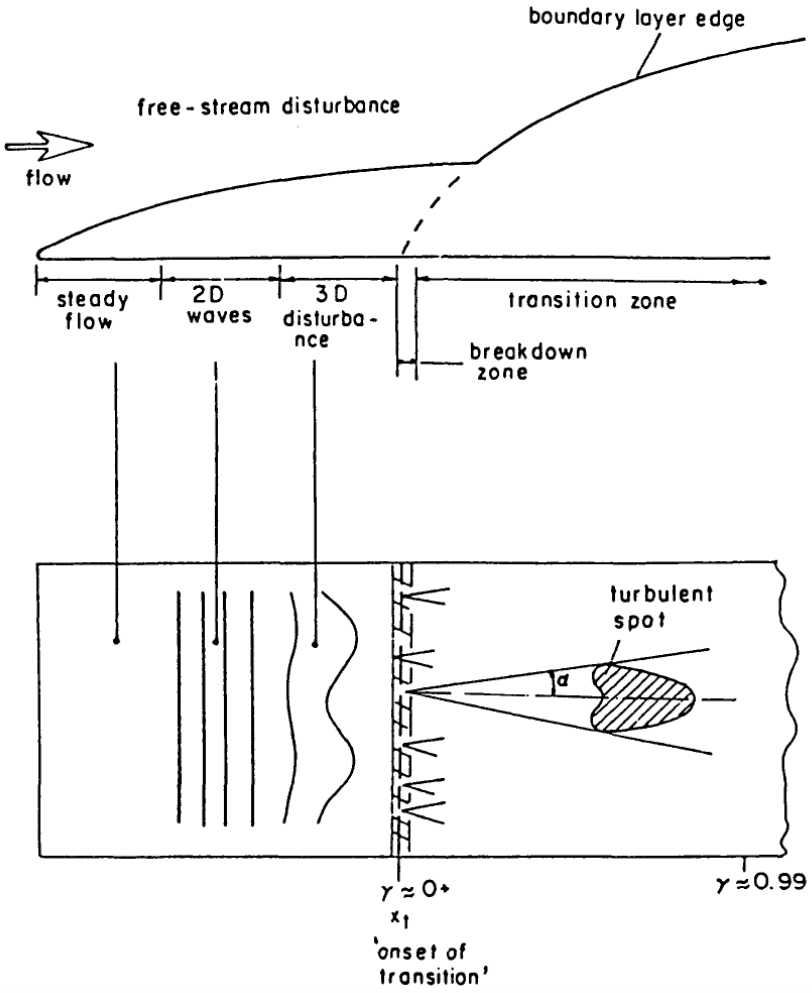

Fig. 1.3 Schematic diagram of transition from laminar to turbulent flow. α and γ respectively denote spot spread angle and intermittency. For high-turbulence intensity, the instability stages may get bypassed. (Reproduced from Narasimha & Dey (1989))

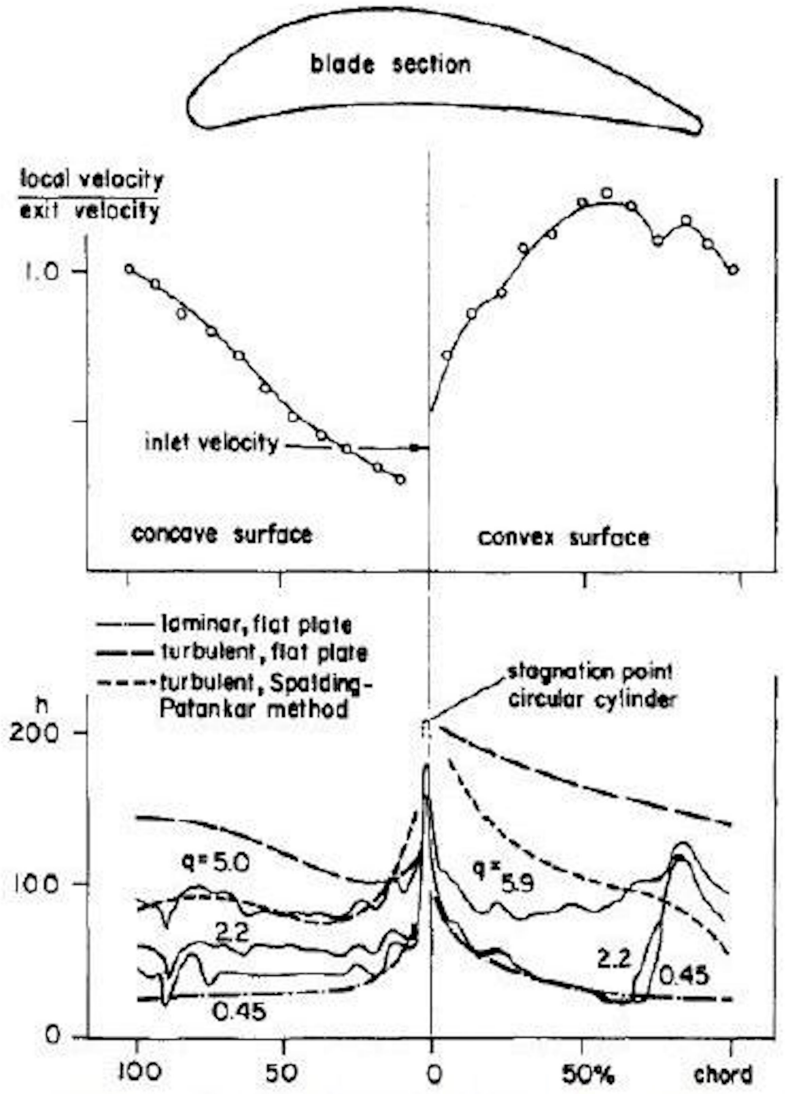

Fig. 1.4 Heat transfer rate on a turbine blade (based on Turner (1971)). From top to bottom: Blade section; External velocity distribution on blade surface; Local heat transfer coefficient (in $CHU/ft^2h^\circ C$) along chord at turbulence levels $q = 0.45, 2.2, 5.0$ and 5.9% (Reproduced from Narasimha (1985))

In the later highly non-linear stages of evolution towards turbulence, so called breakdowns occur in the region of peak amplitude in the lambda vortices. The breakdown appear in the form of 'bursts', which basically have an element of randomness in their structure. These bursts grow into what Emmons (2012) called turbulent spots, which travel downstream growing in area along wedges. Eventually the spots overlap each other, leading to a fully turbulent flow. In this process flow is intermittent, switching every now and then from laminar to turbulent states. The fraction of time that the flow is turbulent is known as intermittency, which varies from 0 at transition onset to unity in fully developed turbulent flow. This picture was confirmed by Schubauer & Klebanoff (1956). The propagation of spots and the number of spots formed per unit time and spanwise distance at the onset of transition, and their propagation characteristics, depend on the pressure gradient imposed on the BL.

For a turbine blade, the transition may be natural, bypass or due to separated flow, depending on the flow conditions such as free-stream turbulent intensity (FSTI) and wake disturbance from upstream stages. Bypass transition is observed if the disturbance level is high, in which the early instability stages as explained above may get bypassed. For separated-flow transitions in laminar separation bubbles, this onset of transition may be within the bubble.

Transition is particularly important for turbine blade flow studies, because the peak heat-transfer rate on the blade depends on the location of the onset of transition. Thus, from the designer's perspective, data on transition are very useful for efficient blade design.

Narasimha (1985) has presented heat-transfer rates on an internally cooled turbine blade at different turbulence levels based on a report by Turner (1971). Figure 1.4 shows how the peak heat-transfer rate on the blade depends on the transition zone, which is strongly influenced by complex interactions between pressure distribution, curvature, and free-stream disturbances. The blade profile, shown at the top, has strong favourable pressure gradients on both sides of the surface. On the convex side, the onset of transition moves rapidly forward as turbulence level increases and at 5.9%, around 80% of the surface is in the transition zone. Also the peak heat-transfer rate on the convex side (which occurs at the end of the transition zone) is significantly higher than it would have been if flow were turbulent from the leading edge. The heat-transfer rate for the fully turbulent flow was calculated by the methods of Patankar & Spalding (1968).

Relaminarization

Relaminarization or reverse transition occurs when a turbulent or transitional boundary layer, reverts to a laminar or quasi-laminar state under the influence of a strong favourable pressure gradient. Incidently, relaminarization on turbine blades was found very early, and was first

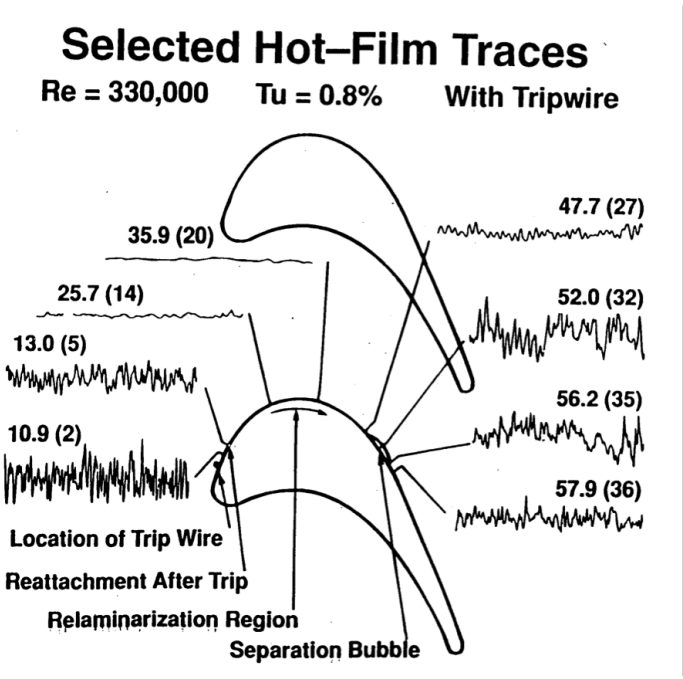

Fig. 1.5 Relaminarization on a turbine blade (Due to D. Wisler (1993). Reproduced from LaGraff (2007))

documented by Wilson & Pope (1954) while studying the heat-transfer co-efficients on gas turbine blades. Relaminarization under strong pressure gradients can be characterized by two visible aspects: (1) Thinning of the boundary layer and (2) decrease in skin-friction and heat-transfer co-efficients.

In the relaminarization region, the Reynolds shear stress does not die down completely as in a perfectly laminar flow, but becomes negligible compared to that of the pressure gradient (Narasimha & Sreenivasan 1973). Relaminarization may sometimes lead to multiple transitions on a turbine blade, as the relaminarized flow could experience retransition to turbulence when the favourable pressure gradient diminishes.

In an experiment by Wisler (LaGraff 2007), relaminarization is clearly observed on the suction side of the blade (see Fig. 1.5) . The hot film traces show that the flow that was turbulent near the leading edge (due to tripping) becomes calmer as it goes through a favourable pressure gradient. The flow again becomes transitional as it encounters a separation bubble (see Fig. 1.5), which acts like a trip to trigger transition. Multiple transitions have also been observed on swept wings Mukund *et al.* (2012).

1.2 RANS, LES, DNS

Conventional CFD tools like RANS and LES may be satisfactory if the interest is in features related to the bulk parameters of a turbulent shear flow, however phenomena like transition, boundary-layer separation, relaminarization etc., which involve large departures from standard fully-developed turbulent flow, cannot be captured by such models. It was suggested by Narasimha in Minnowbrook I 1993 Workshop on End-Stage Boundary Layer Transition (LaGraff 2007) that in such situations it is worth-while to have DNS studies of flow past the turbine blade. The supporting argument was that, despite the complicated flow on the blade, the Reynolds number (in the range of 2×10^4 to 5×10^5) is manageable enough to do a DNS. Figure 1.6 shows a snapshot from the presentation made by Narasimha at Minnowbrook II, LaGraff & Ashpis (1998), where this proposal was revisited.

With the recent boom in computing power and advances in more accurate numerical schemes (Honein & Moin 2004; Jameson 2008; Shoeybi *et al.* 2010), the trend is now slowly changing towards doing DNS to understand complex flows of the kind discussed above. DNS is being identified as one of the promising tools that can significantly help to understand the flow over these blades and to draw important conclusions which, in turn, can help development of improved blade designs. However, due to the complexity of blade geometry and the wide prevalence of transitions from laminar to turbulent flow as well as the reverse, most DNS simulations are still limited in general to flow over relatively simple geometries like flat plates (Wissink & Rodi 2009) or circular cylinders (Venema *et al.* 2011; Wissink & Rodi 2011; Wissink & Rodi 2011, 2008), which at best mimic some features of the flow over turbo-machinery blades. This is perhaps because of lack of adequate numerical schemes with the desired accuracy, and difficulty in implementation of boundary conditions in unstructured grids.

A few DNS results (Kehinde 2003; Wissink *et al.* 2006; Wissink & Rodi 2006; Zaki *et al.* 2010; Rai 2011) have been reported for flow over turbo-machinery blades (in compressors as well as turbines); however most of them have been carried out assuming incompressible flow, and also detailed boundary layer analysis is lacking. Since the beginning of the present work, two more investigators (Michelassi *et al.* 2015; Garai *et al.* 2015) have reported compressible DNS studies on LP turbine blades. An exhaustive list of DNS on LP turbine blades is given in section 1.4.

With a few investigators (Stadtmuller 2002*a*; Liu & Rodi 1994*b*,*a*; Stieger *et al.* 2003; Stieger & Hodson 2004, 2005; Choi *et al.* 2004) doing experiments on flow over turbine blades at relatively low Reynolds numbers of order 10^5 (suitable for a DNS study), and providing important data to compare with, a full-fledged DNS should be the preferred

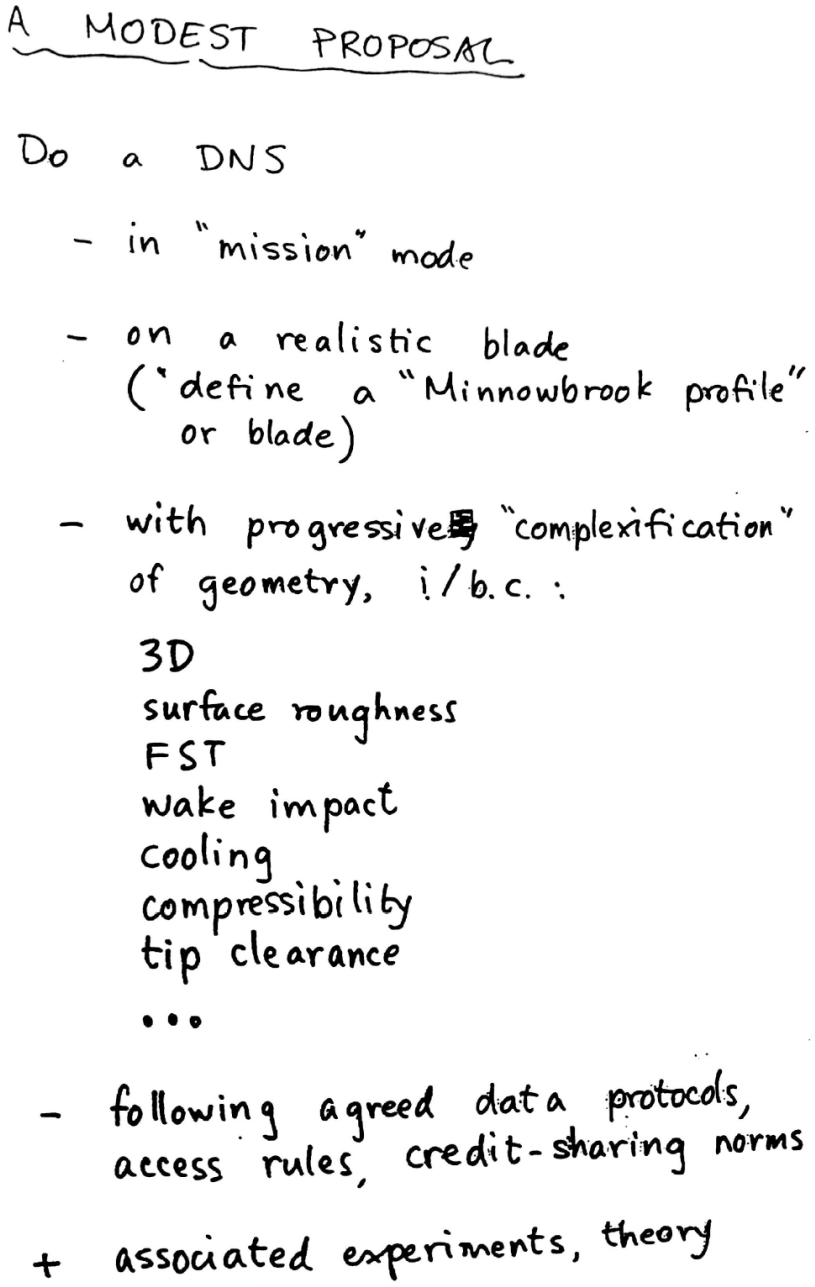

Fig. 1.6 Proposal for a DNS study of turbine blade flow, Minnowbrook-II. (reproduced from LaGraff & Ashpis (1998))

technique to enhance our understanding of such complex flows. Section 1.3 provides details of a few experimental studies in the open literature for which DNS/LES are attempted.

1.3 Experimental Studies

Table 1.1 lists the experimental studies reported in the literature on fluid-dynamical studies of LPT blades. The list includes only the experiments at low to moderate *Re* that are amenable to a DNS study with currently available computational power, and is therefore not exhaustive.

1.3.1 The T106 Cascade

The T106 high-lift LPT blade represents the mid-section of the Pratt & Whitney PW2037 LPT, and has been the subject of many experimental and computational studies (Tables 1.1 , 1.2). Stadtmuller (2002*a*,*b*) has performed experiments on a cascade at two design conditions of the 2D blades of T106 at different solidities: The T106A cascade has a pitch-to-chord ratio $p/l = 0.799$ and represents design conditions (Stadtmuller 2002*a*), and T106D-EIZ cascade has $p/l = 1.05$ representing off-design conditions (Stadtmuller 2002*b*). These experiments have been performed on a 7-blade cascade in the High Speed Cascade Wind Tunnel facility at Universität der Bundeswehr München, Germany. Tests have been carried out at a relatively low *Re* (6×10^4 based on exit velocity and chord length of the blade) so that experimental data are suitable for DNS study. Separation is reported near the trailing edge (TE) of the suction side for experiments with and without upstream-wake impingement on the turbine blade.

These experiments on the T106A provide the basis for the DNS study reported in this thesis. Further details on these experiments are given in Chapter 4 with the major parameters describing the test set-up.

Stieger & Hodson (2004) have performed detailed experiments to understand the transition mechanism in a highly loaded blade. Incoming wakes interact with the separated shear layer to form roll-up vortices by the inviscid Kelvin-Helmholtz (K-H) mechanism. These vortices then breakdown into turbulent flow and get advected along the blade. The experiments are performed at relatively high $Re(= 1.6 \times 10^5)$ compared to Stadtmuller (2002*a*).

1.3.2 MTU Cascade

Liu & Rodi (1994*a*,*b*) conducted experiments on a linear turbine cascade with incoming unsteady wakes. The wakes are generated by a set of parallel cylinders mounted on a belt moving across the free-stream upstream of the blade. *Re* was kept at $72,000$ based on axial

Table 1.1 Experiments on LPT blades

Group	**Ref.**	**Blade**	**Re**	**Remarks**
Stadtmuller (2002)	Stadtmuller (2002*a*,*b*); L Hilgenfeld (2003)	T106A, T106D	51,800 & 500,000[a]	Experimental data at low *Re* for wake-induced transition. Separation at TE
Stieger et. al (2003)	Stieger *et al.* (2003); Stieger & Hodson (2004, 2005)	T106A	160,000[a]	At low *Re* and low FSTI, wake triggers K-H instability that breaks into turbulent flow & gets convected
Liu & Rodi (1994)	Liu & Rodi (1994*b*,*a*)	MTU	72,000[b]	BL on suction side becomes transitional under wake disturbances. Wake passing freq. increases heat transfer
Volino (2002)	Volino (2002*a*,*b*, 2003)	Pak-B	25,000-300,000[c]	Increasing *Re* & FSTI makes transition move upstream. For low *Re*, no reattachment and no transition
Choi et. al (2004)	Choi *et al.* (2004)	No name	15,700-105,000[b]	Flow-separation at LE is enhanced as the *Re* decreases but gets suppressed with increasing FSTI

[a] based on axial chord length and exit velocity
[b] based on axial chord length and inlet velocity
[c] based on the suction surface wetted length and exit velocity

chord and inlet velocity, and the wake Strouhal number was in the range 0 to 7.36 to help understand the effect of wake passing frequency on transition. The boundary layer (BL) on the suction side becomes transitional under wake disturbances, while on the pressure side it always remains laminar. Increasing wake passing frequency causes the onset of transition to move upstream and results in significant increase in the heat transfer.

1.3.3 PakB Cascade

Pak-B airfoil shape is designed by Pratt & Whitney, and the cascade geometry is representative of modern LPT designs. It has been subjected to many experimental and computational studies (see Volino (2002*a*) for a partial list till 2002).

Volino (2002*a*,*b*) conducted experiments for a range of *Re*, from 25,000 to 200,000 based on suction surface length and exit velocity, and two different free-stream turbulence intensity levels (FSTI = 0.5%, 9%). The onset of transition is near the beginning of BL attachment following separation at the leading edge, and varies strongly with *Re* and FSTI. For lowest *Re* cases (25,000 and 50,000), separated BL at leading edge did not attach and transition was not seen for either low or high FSTI.

For higher *Re*, transition began in the shear layer over the separation bubble, causing BL to reattach. With increase in *Re* and FSTI, transition moves upstream.

Öztürk & Schobeiri (2007) have recently performed experiments on Pak-B at $Re = 110,000$ with different FSTI as well as varying wake-passage frequencies, in particular to understand the behaviour of separation bubbles under such disturbances. Separation dynamics is governed by periodic unsteady wake if time-averaged turbulent fluctuations is below maximum wake fluctuation. Above it, the dynamics is governed by flow turbulence that causes suppression of the separation bubble.

1.3.4 Others

Choi *et al.* (2004) have performed experiments at $15,700 \leq Re \leq 105,000$ to study the effect of free-stream turbulence on heat-transfer and pressure distribution on a turbine blade. The blade subjected to study has a chord-length of 22.68 cm, radial span of 25.4 cm and blade spacing of 17.01 cm. It is reported that flow-separation at leading edge is enhanced as the *Re* decreases but gets suppressed with increasing turbulence intensity. Local Nusselt Number and local heat-transfer coefficient increase with increasing *Re* and turbulent intensity.

This could also have been a good case for our computational study, but we could not get access to full details. The request for the data on blade geometry was denied, even though the paper(Choi *et al.* 2004) promises availability as follows:

> "The details of the blade geometry are not provided here. But the interested reader can either contact the corresponding author for the details or digitize directly from the true geometry shown in Fig. 1."

1.4 DNS Studies

This section considers the DNS studies performed on different LPT blades by various workers. The literature is full of RANS studies on different blades and also a few LES, but the current list is strictly limited to 3D DNS studies that focus on understanding the complex flow on the blade and implications for engineering parameters. A non-exhaustive list of LES and RANS simulations is given in chapter 6.

Table 1.2 lists the DNS studies on LP turbine blades along with corresponding blade and experiment. Important simulation and numerical parameters such as *Re*, grid size and resolution in wall-units ($\Delta x^+, \Delta y^+, \Delta z^+$) are given, where-ever available. Important purpose and outcome of the studies are briefly mentioned.

These studies can be broadly categorized in four types by the kind of inlet used:

- No inlet disturbance (clean)
- With free-stream turbulence (FSTI)
- With incoming wakes (wake)
- With wakes + free-stream turbulence (wake+FSTI)

The terms given in the parenthesis above are used throughout this thesis to refer to respective inlets used in DNS studies.

The first DNS study was performed by Wu & Durbin (2001) at $Re = 1.48 \times 10^5$ and inflow angle $\beta_1 = 37.7$ deg on the T106A blade. The simulation was performed on a moderate grid of 57 million points with incoming wakes. The main focus of the study was on resolving the distorted wake in the passage between the blades. Presence of longitudinal vortices along the pressure side of the blade was reported, and confirmed later by the DNS results of Wissink (2003) and Wissink *et al.* (2006).

In the DNS study of Kalitzin *et al.* (2003), flow past the T106A has been simulated at the same *Re* and β_1 as in Wu & Durbin (2001), but to understand the influence of grid turbulence and wakes separately on the flow. Both grid turbulence and wakes lead to by-pass transition in the adverse pressure gradient region on the suction side, however grid turbulence was not as effective as wakes in inducing boundary-layer instabilities. Grid turbulence does however increase turbulent kinetic energy in the passage towards the trailing edge of the pressure side.

Table 1.2 DNS on LPT blades

Authors	**Blade**	**Ref. expt.**	**Re**	**Grid size**	ΔX^+	ΔY^+	ΔZ^+	**Remarks**
Wu & Durbin (2001)	T106	Stadtmuller (2002)	1.48×10^5[a]	$1152 \times 384 \times 128 \approx 57$ M	-	-	-	Impinging wakes induce formation of longitudinal vortices
Michelassi *et al.* (2002); Wissink (2003)	T106A	Stadtmuller (2002)	51,800[a]	$1014 \times 266 \times 64 \approx 17$ M	10	0.8	3	Comparison with RANS, LES. Effects of wake on laminar separation
Kalitzin *et al.* (2003)	T106A	Stadtmuller	1.48×10^5[a]	$1152 \times 576 \times 128 \approx 85$ M	28	2.3	1.9	Inflow turbulence causes bypass transition
Wissink *et al.* (2006)	T106A	Stieger & Hodson (2003,05)	51,831[a]	$1014 \times 266 \times 64 \approx 17$ M	-	-	-	Wakes cause K-H instability. Transition happens inside KH-rolls
Wissink & Rodi (2006)	T106A	Stadtmuller (2002)	51,800[a]	$1014 \times 260 \times 64 \approx 17$ M	-	-	-	K-H instability crucial in early transition to turbulence for separated flow
Wissink & Rodi (2006)	MTU	Liu & Rodi (1994a,b)	72,000[a]	$1254 \times 582 \times 128 \approx 93$ M	25	1.5	15	FSTI triggers by-pass transition in the adverse pressure gradient region
Michelassi *et al.* (2015)	T106A	Stadtmuller (2002)	59,634[b]	$274176 \times 66 \approx 18$ M	10	1.4	11	Compressible. Effect of inlet turbulence on transition & wake
Garai *et al.* (2015)	T106A	Stadtmuller (2002)	60,000[b]	30.72 M[c]	-	-	-	Compressible. Validation study for high order DG method

[a] based on inlet velocity

[b] based on exit velocity

[c] For DG, Degree of Freedoms are converted to equivalent grid points for comparisons with FV and FD. $(n/p) \times (n/p) \times (n/p)$ DG grid roughly equivalent to $n \times n \times n$ FV, FD grid (Nogueira *et al.* 2009)

Michelassi *et al.* (2002); Wissink (2003) have performed a DNS study of flow past T106A at $Re = 51,831$ and $\beta_1 = 45.5^0$. The set-up used is the same as in the experiments of Stadtmuller (2002*a*). Simulations have been performed for clean inlet as well as with wake but no FSTI, and are compared with the experimental data available. On the pressure side where flow is relatively simple, the pressure coefficient matches well with the experimental data. However on the suction side there is a considerable difference in the match (see chapter 5). The reasons reported for this difference are: (a) uncertainties concerning exact inflow angle in the experiment, and (b) assumption of incompressible flow in the governing DNS equations. Separation bubbles have been found on the suction side at LE as well as TE. It is to be noted that in the experiment only one separation near the TE is reported. The LE separation bubble is short and unstable, and disturbances due to it get damped out downstream by the favourable pressure gradient. The presence of periodically impinging wakes was responsible for suppressing the TE separation bubble intermittently. The separated shear layer near TE rolls up due to K-H instability, and fluctuating kinetic energy gets produced in these rolls. The parameters used in the present DNS study are the same as in Wissink (2003) except for the fact that the present simulations are performed using compressible set-up.

Wissink *et al.* (2006) performed DNS of flow past T106A at the same Re and β_1 as Wissink (2003), but to understand the effect of large and small scale fluctuations in the incoming wake. Separation is again found both at LE and TE. Impinging wakes trigger K-H instability in the TE separated shear layer. Transition to turbulence in this shear layer depends on the presence of small-scale fluctuations. The onset of transition moves upstream in the presence of the wake, but is chiefly due to the presence of small-scale fluctuations.

Wissink & Rodi (2006) calculated the heat transfer on a heated MTU blade using DNS, which was set-up to simulate the experiments of Liu & Rodi (1994*b*,*a*). The simulations were performed to study the influence of impinging wakes and background fluctuations on local heat transfer and boundary layer development. On the suction side, for the case without free-stream turbulence, the boundary layer remains laminar. However with periodic wakes and fluctuations, the initial laminar flow becomes transitional in the adverse-pressure gradient region (downstream along the blade). The heat-transfer also increases significantly in this region.

Recently Sandberg *et al.* (2015); Michelassi *et al.* (2015) and Garai *et al.* (2015) have revisited the experiments by Stadtmuller (2002*a*) to validate their numerical methods developed for DNS and also to gain fresh insights. They have respectively used compact finite difference in multiblock structured grids, and Discontinuous-Galerkin (DG) spectral-element approaches to solve the compressible flow on the T106A blade. They have presented superior match of pressure with experimental results, as compared to Wissink (2003), though there is

unanimity on the presence of separation bubble at the LE for the clean (with no inlet disturbance) case. This issue is highlighted in chapter 5. A detailed study of inflow disturbances is presented in Michelassi *et al.* (2015), where it is shown that the presence of background turbulence and/or incoming wakes helps reduce the size of the separation bubble or even suppress it.

The author of this thesis was the first one to perform a compressible DNS of flow past an LPT blade (Ranjan *et al.* 2013, 2014), to the best of the author's knowledge. A study of the very significant impact that resolution has on the solution was presented at an IUTAM Symposium (Ranjan *et al.* 2016). The details of these simulations and the analyses form the essential contents of this thesis and are described in chapters 4, 5 and 6.

1.5 The present DNS Approach

Our approach in this work is to conduct a systematic and detailed DNS study of flow past the LPT blade T106A with a well-validated compressible code. A new DNS code, named ANUROOP has therefore been developed by the author for this purpose. Unlike in previous works, the focus here is on detailed studies of the boundary layer on the blade, rather than on flow in the passage between the blades. The grid topology and resolution have been selected accordingly.

DNS has been performed for a simple set-up of passage between two consecutive blades. The simulation parameters are chosen according to the experimental details given in Stadtmuller (2002*a*). A grid-resolution study is performed and results are compared against available experimental and computational results. The three aspects described in section 1.1, such as separation, transition and relaminarization, are studied in some detail to broadly reflect on flow regimes on an LP turbine blade. The effects of curvature are also analysed. The instantaneous flow is compared with the mean flow for skin-friction co-efficient as well as the heat-flux.

Finally RANS and LES simulations are performed using commercial code CFD++ to understand the scope and limitation of such approaches in complex turbine blade flows.

The thesis has been organised in the following way.

- Numerical algorithm employed in development of present DNS code has been described in detail in Chapter 2
- Chapter 3 contains validation and verification studies performed on the code
- Numerical and computational aspects of simulations on T106A blade are covered in Chapter 4

- Chapter 5 describes interesting findings on flow past LPT blade on fluid-dynamical aspects
- RANS and LES simulations are described in Chapter 6. Engineering parameters such as skin-friction and heat flux are also given in this chapter
- Final concluding remarks are given in Chapter 7

Chapter 2

Numerical Methodology

A new DNS code has been developed for the present study of flow past turbine blades. This chapter formulates the governing equations and describes the methodology adopted in the DNS code along with brief details on its implementation. Specific features of the code, such as spatial and temporal discretization, boundary conditions, parallelization etc., are also documented in this chapter.

2.1 The DNS Code ANUROOP

In DNS, the entire set of physical equations governing the flow under consideration are solved without resorting to any dynamical modeling or approximation. The only approximation involved is due to numerical implementation, where the partial differential equations (PDEs) are converted to ordinary differential equations (ODEs) and then solved on the computer using linear algebra techniques. Since all the scales of the turbulent flow are resolved in a typical DNS with adequate resolution, the requirement on computational power is generally very high.

Further, the choice of the grid and the computational scheme depend on the kind of problem being solved. Spectral methods, because of their accuracy, are historically a preferred choice for performing DNS. However their ability is generally limited to simple geometries and to problems where the grid on the computational domain is relatively simple and structured.

For more practical engineering flows in computational domains with complicated geometry, DNS is yet to become an established analysis tool. This is partly because of very high computational power requirement (Re is generally high) in practical flows. Nevertheless, unlike RANS and LES, there is not much literature available on the numerical schemes most

suitable for such DNS studies. Hence the choice of most suitable numerical method for DNS studies is still a debatable topic.

Flow past gas turbine blades is perhaps one of the more widely studied practical engineering problems because of the moderate computational power requirement (because of relatively low *Re*), and the degree of complexity in the flow that puts it beyond the RANS codes in common studies. In the open literature (see chapter 1), most of these simulations (except for very recent ones) solve incompressible Navier-Stokes equations (thereby ignoring compressibility effects), and are performed using the Finite Volume Method (FVM). FVM has the advantage of being able to work on grids in computational domains with complicated geometry.

As the compressibility effect is one of the major reasons given in earlier simulations (see chapter 1) for the poor match in pressure co-efficients on the suction side between the DNS and experiments, it was decided to write a compressible code for the current study. A new code named ANUROOP (meaning resembling or concordant in Sanskrit) was thus developed by the author to solve the 3D compressible Navier-Stokes equations in 3D space and time. At the time that the present code was developed (Ranjan *et al.* 2013), there was no published compressible DNS study in the open literature; however the compressible flow studies have appeared since then (Sandberg *et al.* 2015; Michelassi *et al.* 2015; Garai *et al.* 2015).

ANUROOP is developed in the FVM framework because of the following advantages: (1) FVM can be used in domains of complicated geometry. (2) FVM solves the equations in conservative form and hence becomes a natural choice for solving compressible equations which demand accurate conservation as an essential requirement. Also the current study focuses on the boundary layer flow on the turbine blades and not on the passage flow, which was the major interest in eariler studies. For this purpose, a new hybrid grid is used for simulations on the blades, with a fine boundary layer grid on the wall and a general hexahedral grid for the rest of the passage.

2.2 3D Compressible Navier-Stokes Equations

The Navier-Stokes equations are the governing equations in fluid flow in aircraft gas turbines and express conservation of mass, momentum, and energy. The assumptions commonly made in deriving these equations are stated and the modeling of various thermodynamic, and transport properties is briefly described below. The compressible continuity, momentum and

energy equations in dimensional form are given by:

$$\frac{\partial \rho}{\partial t} + \frac{\partial (\rho u_j)}{\partial x_j} = 0 \tag{2.1a}$$

$$\frac{\partial (\rho u_i)}{\partial t} + \frac{\partial (\rho u_i u_j)}{\partial x_i} = -\frac{\partial p}{\partial x_i} + \frac{\partial \tau_{ij}}{\partial x_j} \tag{2.1b}$$

$$\frac{\partial (\rho E)}{\partial t} + \frac{\partial (\rho u_j H)}{\partial x_j} = \frac{\partial}{\partial x_j}(u_i \tau_{ij}) - \frac{\partial}{\partial x_j} q_j \tag{2.1c}$$

where ρ and u_i are density and velocity vector components ($i = 1,2,3$) respectively; E and H are total energy and total enthalpy per unit mass respectively, given by:

$$E = e + K = c_v T + \sum_{i=1}^{3} \frac{u_i u_i}{2}$$

$$H = E + \frac{p}{\rho}$$

where e is the internal energy and K is the kinetic energy of the gas. To close the above set of equations, they must be supplemented by an equation of state which, for a perfect gas, is:

$$p = \rho R T \tag{2.2}$$

The viscous stress tensor and the heat flux vector are given respectively by:

$$\tau_{ij} = \mu \left[\frac{\partial u_i}{\partial x_j} + \frac{\partial u_j}{\partial x_i} - \frac{2}{3} \delta_{ij} \frac{\partial u_k}{\partial x_k} \right] \tag{2.3}$$

$$q_i = -k \frac{\partial T}{\partial x_i} \tag{2.4}$$

The co-efficients μ and k are viscosity and thermal conductivity respectively, which vary with the local temperature T and are assumed to follow Sutherland's law -

$$\frac{\mu}{\mu_0} = \left(\frac{T}{T_0} \right)^{1.5} \left(\frac{T_0 + S_\mu}{T + S_\mu} \right) \tag{2.5a}$$

$$\frac{k}{k_0} = \left(\frac{T}{T_0} \right)^{1.5} \left(\frac{T_0 + S_k}{T + S_k} \right) \tag{2.5b}$$

where μ_0 and k_0 are reference values of viscosity and thermal conductivity at a given reference temperature T_0, and S_μ and S_k are the Sutherland constants for viscosity and thermal conductivity respectively. Typical values used for the Sutherland constants for air

are $S_\mu = 110.4^\circ$ K and $S_k = 194.4^\circ$ K. These correlations are accurate up to 2% in the temperature range of 160° K to 1000° K (Sutherland 1893).

2.2.1 Non-dimensionalization

In fluid dynamics simulations, the above equations are often solved in non-dimensional form, which helps setting up the simulation in terms of the non-dimensional numbers that govern the physics of the flow, for example the Reynolds number (Re), Prandtl number (Pr) and Mach number (M). The variables in the equations can be non-dimensionalized with reference values (represented by subscript ref) and scales as given below :

$$
\begin{aligned}
& x_i \rightarrow L^\star_{ref} \\
& u_i \rightarrow U^\star_{ref} \Rightarrow t \rightarrow \frac{L^\star_{ref}}{U^\star_{ref}} \\
& \rho \rightarrow \rho^\star_{ref} \Rightarrow p \rightarrow \rho^\star_{ref} {U^\star_{ref}}^2 \\
& T \rightarrow T^\star_{ref} \\
& \mu \rightarrow \mu^\star_{ref}
\end{aligned}
$$

This leads to a set of non-dimensional conservation equations given by

$$\frac{\partial \rho}{\partial t} + \frac{\partial (\rho u_j)}{\partial x_j} = 0 \tag{2.6a}$$

$$\frac{\partial (\rho u_i)}{\partial t} + \frac{\partial (\rho u_i u_j)}{\partial x_i} = -\frac{\partial p}{\partial x_i} + \frac{1}{Re}\frac{\partial \tau_{ij}}{\partial x_j} \tag{2.6b}$$

$$\frac{\partial (\rho E)}{\partial t} + \frac{\partial (\rho u_j H)}{\partial x_j} = \frac{1}{Re}\frac{\partial}{\partial x_j}(u_i \tau_{ij}) + \frac{1}{(\gamma - 1) M^2_{ref} RePr}\frac{\partial}{\partial x_j} q_j \tag{2.6c}$$

And the equation of state takes the form

$$p = \frac{1}{\gamma M^2_{ref}} \rho T \tag{2.7}$$

In the above, $Re = \rho^\star_{ref} U^\star_{ref} L^\star_{ref} \Big/ \mu^\star_{ref}$ is the Reynolds number and $Pr = \mu_{ref} c_p \big/ k_{ref}$ is the Prandtl number. Reference mach number M_{ref} is $U^\star_{ref} \Big/ c^\star_{ref}$, where $c^\star_{ref}$ is the speed of sound based on reference temperature $T^\star_{ref}$ and is equal to $\sqrt{\gamma R T^\star_{ref}}$, where $\gamma = \dfrac{c_p}{c_v}$ is the ratio of specific heats at constant pressure and at constant volume.

When the specific flow velocity cannot be defined, for example in a shock-tube, it is useful to non-dimensionalize the equations with reference speed of sound ($c^{\star}_{ref}$) rather than reference flow velocity ($U^{\star}_{ref}$). In that case the energy equation and the equation of state take the form as given below, respectively:

$$\frac{\partial(\rho E)}{\partial t}+\frac{\partial(\rho u_j H)}{\partial x_j}=\frac{1}{Re}\frac{\partial}{\partial x_j}(u_i\tau_{ij})+\frac{1}{(\gamma-1)RePr}\frac{\partial}{\partial x_j}q_j$$

$$p=\frac{1}{\gamma}\rho T$$

Note that Re is here defined based on $c^{\star}_{ref}$, i.e. $Re=\rho^{\star}_{ref}c^{\star}_{ref}L^{\star}_{ref}/\mu^{\star}_{ref}$.

2.3 The Flow-solver Algorithm

It was decided to solve the underlining governing equations using cell-centered Finite Volume Method (FVM). FVM is flexible, robust and allows the solution of flow problems in domains with a complicated geometry. The flux calculations in FVM are local and no separate formulation is needed for structured and unstructured grids. This is useful for solving wall-bounded flows past a complicated surface geometry where different grid topologies can be used for the boundary layer and the external flow. Further, since FVM solves the equations in conservative form, it is useful for solving compressible flow equations where conservation of energy is a prime requirement.

1D Finite Volume

The Navier-Stokes in one-dimension can be written as

$$\frac{\partial}{\partial t}\mathbf{U}(x,t)+\frac{\partial}{\partial x}\mathbf{f}(x,t)=0 \tag{2.8}$$

or,

$$\mathbf{U}_t+\mathbf{f}_x=0$$

where

$$\mathbf{f}=\mathbf{f}_{inv}+\mathbf{f}_v$$

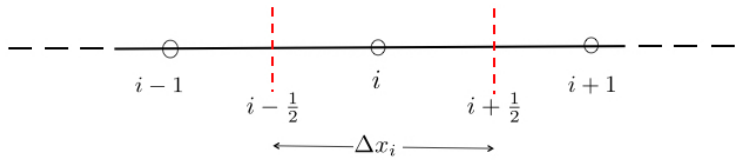

Fig. 2.1 Schematic of 1D finite volume domain

$$\mathbf{U} = \begin{pmatrix} \rho \\ \rho u \\ e \end{pmatrix}, \ \mathbf{f_{inv}} = \begin{pmatrix} \rho u \\ \rho u^2 + p \\ (e+p)u \end{pmatrix}, \ \mathbf{f_v} = \begin{pmatrix} 0 \\ \tau_{xx} \\ \tau_{xx}u - q_x \end{pmatrix}$$

and,

$$e = \frac{P}{\gamma - 1} + \frac{\rho u^2}{2}, \ \tau_{xx} = \frac{4}{3}\mu\frac{\partial u}{\partial x}, \ q_x = -k\frac{\partial T}{\partial x}$$

Figure 2.1 shows a schematic of a typical grid for a finite volume treatment of a 1D flow problem. The mid-computational control volume has the cell-center at i and is surrounded by neighbour cells, which have centers at $i-1$ and $i+1$. In a cell-centered finite volume, the physical variables are stored at the cell-centers and the fluxes are calculated on all the faces of the cells, e.g. faces $i-\frac{1}{2}$ and $i+\frac{1}{2}$ for cell i in a cartesian system. Now, integrating eqn. 2.8 for the volume element i in Fig. 2.1,

$$\begin{aligned} \int_{x_{i-\frac{1}{2}}}^{x_{i+\frac{1}{2}}} (\mathbf{U}_t + \mathbf{f}_x)\, dx &= 0 \\ \implies \frac{\partial}{\partial t}\int_{x_{i-\frac{1}{2}}}^{x_{i+\frac{1}{2}}} \mathbf{U}\, dx + \int_{x_{i-\frac{1}{2}}}^{x_{i+\frac{1}{2}}} \mathbf{f}_x\, dx &= 0 \end{aligned}$$

Defining the cell-averaged value of a quantity U as $\overline{\mathbf{U}_i} = \dfrac{1}{\Delta x_i}\displaystyle\int_{x_{i-\frac{1}{2}}}^{x_{i+\frac{1}{2}}} \mathbf{U}\, dx$, the above equation becomes

$$\Delta x_i \frac{\partial \overline{\mathbf{U}}}{\partial t}|_i + (\mathbf{f}_{i+\frac{1}{2}} - \mathbf{f}_{i-\frac{1}{2}}) = 0$$

This removes the spatial dependence and the PDE converts to an ODE in time,

$$\frac{d\overline{\mathbf{U}}}{dt}|_i \;=\; -\frac{(\mathbf{f}_{i+\frac{1}{2}} - \mathbf{f}_{i-\frac{1}{2}})}{\Delta x_i}$$

On a computer, this ODE can be solved using an appropriate time-marching scheme for the entire computational domain. For example, for explicit time-marching (generally preferred in time-accurate calculations), we take

$$\overline{\mathbf{U}}_i^{n+1} \;=\; \overline{\mathbf{U}}_i^n - \frac{\Delta t}{\Delta x_i}\left(\mathbf{f}_{i+\frac{1}{2}}^n - \mathbf{f}_{i-\frac{1}{2}}^n\right)$$

Appropriate boundary conditions are imposed at the boundaries.

3D Finite Volume

The idea of 1D finite volume can be extended to 3D with few complications. The equation 2.1 can be expanded in 3D as follows:

$$\frac{\partial \mathbf{U}}{\partial t} + \frac{\partial \mathbf{f}}{\partial x} + \frac{\partial \mathbf{g}}{\partial y} + \frac{\partial \mathbf{h}}{\partial z} \;=\; 0 \tag{2.9}$$

$$\Longrightarrow \frac{\partial \mathbf{U}}{\partial t} + \frac{\partial (\mathbf{f}_{inv} - \mathbf{f}_v)}{\partial x} + \frac{\partial (\mathbf{g}_{inv} - \mathbf{g}_v)}{\partial y} + \frac{\partial (\mathbf{h}_{inv} - \mathbf{h}_v)}{\partial z} \;=\; 0$$

where

$$\mathbf{U} = \begin{pmatrix} \rho \\ \rho u \\ \rho v \\ \rho w \\ e \end{pmatrix}$$

$$\mathbf{f_{inv}} = \begin{pmatrix} \rho u \\ \rho u^2 + p \\ \rho uv \\ \rho uw \\ (e+p)u \end{pmatrix}, \mathbf{g_{inv}} = \begin{pmatrix} \rho v \\ \rho uv \\ \rho v^2 + p \\ \rho vw \\ (e+p)v \end{pmatrix}, \mathbf{h_{inv}} = \begin{pmatrix} \rho w \\ \rho uw \\ \rho vw \\ \rho w^2 + p \\ (e+p)w \end{pmatrix}$$

and

$$\mathbf{f_v} = \begin{pmatrix} 0 \\ \tau_{xx} \\ \tau_{xy} \\ \tau_{xz} \\ \tau_{xx}u + \tau_{xy}v + \tau_{xz}w - q_x \end{pmatrix}, \mathbf{g_v} = \begin{pmatrix} 0 \\ \tau_{xy} \\ \tau_{yy} \\ \tau_{yz} \\ \tau_{xy}u + \tau_{yy}v + \tau_{yz}w - q_y \end{pmatrix}, \mathbf{h_v} = \begin{pmatrix} 0 \\ \tau_{xz} \\ \tau_{yz} \\ \tau_{zz} \\ \tau_{xz}u + \tau_{yz}v + \tau_{zz}w - q_z \end{pmatrix}$$

and

$$e = \frac{P}{\gamma - 1} + \frac{\rho(u^2 + v^2 + w^2)}{2}$$

$$\tau_{xx} = 2\mu\frac{\partial u}{\partial x} - \frac{2}{3}\mu\nabla.\vec{u},\ \tau_{yy} = 2\mu\frac{\partial v}{\partial y} - \frac{2}{3}\mu\nabla.\vec{u},\ \tau_{zz} = 2\mu\frac{\partial w}{\partial z} - \frac{2}{3}\mu\nabla.\vec{u}$$

$$\tau_{xy} = \mu(\frac{\partial u}{\partial y} + \frac{\partial v}{\partial x}),\ \tau_{yz} = \mu(\frac{\partial v}{\partial z} + \frac{\partial w}{\partial y}),\ \tau_{zx} = \mu(\frac{\partial w}{\partial x} + \frac{\partial u}{\partial z})$$

$$q_x = -k\frac{\partial T}{\partial x},\ q_y = -k\frac{\partial T}{\partial y},\ q_z = -k\frac{\partial T}{\partial z}$$

Now, equations 2.9 can be written as:

$$\frac{\partial \mathbf{U}}{\partial t} + \nabla.\vec{\mathbf{F}} = 0 \tag{2.10}$$

where, $\vec{\mathbf{F}} = (f \quad g \quad h)$ is the same as defined in eqn. 2.9.
Integrating for a computational cell volume Ω_i,

$$\int_{\Omega_i} (\frac{\partial \mathbf{U}}{\partial t} + \nabla.\vec{\mathbf{F}}) d\Omega \; = \; 0$$

Now using the Gauss divergence theorem,

$$\frac{\partial}{\partial t} \int_{\Omega_i} \mathbf{U}.d\Omega + \oint_{S_i} \vec{\mathbf{F}}.d\vec{\mathbf{S}} \; = \; 0$$

Here $\vec{\mathbf{S}}$ is the face area normal vector for cell i.
Defining the cell-averaged quantity as $\overline{\mathbf{U}}_i = \frac{1}{\Omega_i} \int_{\Omega_i} \mathbf{U}.d\Omega$ and denoting integral as the algebraic sum over all the faces, we get-

$$\Omega_i \frac{d\overline{\mathbf{U}}_i}{dt} + \sum_J F_{\perp J} \Delta S_{\perp J} \; = \; 0$$

so,

$$\frac{d\overline{\mathbf{U}}_i}{dt} \; = \; -\frac{1}{\Omega_i} \sum_J F_{\perp J} \Delta S_J \tag{2.11}$$

For explicit time-integration,

$$\overline{\mathbf{U}}_i^{n+1} \; = \; \overline{\mathbf{U}}_i^n - \frac{\Delta t}{\Omega_i} \sum_J F_{\perp J}^n \Delta S_J \tag{2.12}$$

Equation 2.11 is often written as

$$\frac{d\overline{\mathbf{U}}}{dt} \; = \; -\mathbf{R}(\mathbf{U}) \tag{2.13}$$

where $\mathbf{R}(\mathbf{U}) \; = \; \frac{1}{\Omega_i} \sum_J F_{\perp J} \Delta S_{\perp J}$ is called the residual.

Note that the implementation of the finite volume doesn't depend on the topology of the grid, but only on the information of the neighbour cells. This makes it a good choice for computational domains with complicated geometries.

2.3.1 Spatial Discretization

The calculations of inviscid and viscous fluxes at grid points require numerical schemes which are not only sufficiently accurate but also stable and robust. Viscous terms generally add stability to the equations and hence do not require any special treatment, except for a suitable method to calculate gradients in an unstructured grid setup. Calculation of inviscid terms however involves solving the Riemann problem and hence requires special treatment. The following description provides the details of the numerical schemes used in ANUROOP for invsicid and viscous flux calculations.

Inviscid Flux Calculation

For high fidelity simulations like DNS, we require numerical schemes that are non-dissipative and have small aliasing errors, and yet stable and robust. Upwind schemes that use biased-differencing based on directions of characteristic waves are stable and robust, but generally dissipative and hence not considered a suitable choice for DNS. Central-difference schemes, on the other hand, are non-dissipative but have been found to be generally unstable because they do not conserve kinetic energy in the discrete sense. Morinishi *et al.* (1998) have shown that for incompressible Navier Stokes a skew-symmetric formulation of the non-linear advective terms in a central-difference scheme conserves kinetic energy in the discrete sense. The skew-symmetric formulation is also shown to result in smaller aliasing errors and would hence be more robust (Blaisdell *et al.* 1996). For incompressible flows, this idea has been used to develop kinetic-energy conserving central difference schemes for structured (Morinishi *et al.* 1998) and later for unstructured (Mahesh *et al.* 2004) grids.

Recently this idea was extended to compressible Navier-Stokes to conserve kinetic energy in the discrete sense by Jameson (2008), and this scheme is implemented in ANUROOP. This scheme, known as the kinetic energy preserving (KEP) scheme, provides semi-discrete approximations to compressible Navier-Stokes equations in conservative form in which kinetic energy is discretely preserved. KEP scheme for compressible flow is well verified and validated in the literature for various 2D DNS studies, including the shock tube (Jameson 2008; Allaneau & Jameson 2009), plunging airfoils (Allaneau & Jameson 2010), and flow past circular cylinder (Shoeybi *et al.* 2010). In ANUROOP, the KEP scheme is implemented for solving three-dimensional flow past a turbine blade.

Viscous Flux Calculation

In the cell-centered finite-volume scheme, the calculation of the viscous and conduction terms need gradients of velocity and temperature at the face of the volume element. In a

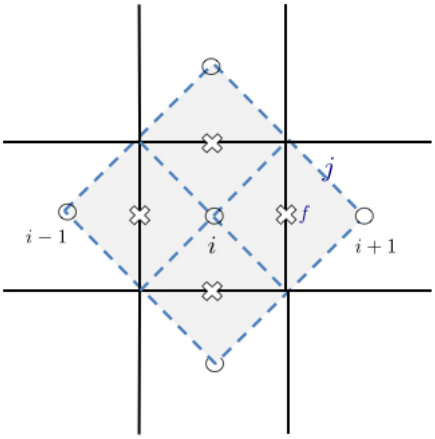

Fig. 2.2 Co-volume for calculation of gradients at face-centers

structured grid, these gradients can be calculated easily using values at the cell-centers on either side of the face - either by using simple finite-differences or taking the average of the cell gradients. In unstructured grids, however, either a least-squares approach or the Green-Gauss method is generally used. In ANUROOP, the Green-Gauss (GG) method is implemented to calculate face gradients. An auxillary volume (called co-volume) is formed around each face connecting the cell-centroids and the face nodes as shown in Fig. 2.2. At the bondaries half co-volumes are constructed; faces of this co-volume are called co-faces. Now using GG, the gradient of a quantity Φ at a face f will be given by

$$\nabla\Phi_f = \frac{\Sigma\Phi_j\vec{\mathbf{A}}_\mathbf{j}}{\Omega_f} \tag{2.14}$$

where Ω_f is the volume of the co-volume encircling face f; Φ_j and $\vec{\mathbf{A}}_\mathbf{j}$ are the averaged values of Φ at co-faces and the face-normal areas of the co-faces of the co-volume respectively.

To implement this scheme, values at the nodes (cell-vertices in this case) are needed as the physical variables are updated and stored at the cell-centers. Typically, area-weighted average or inverse area-weighted average interpolations are used to get the values at nodes. A more accurate method for interpolation on unstructured grids is the pseudo-Laplacian weighted average (see Holmes *et al.* (1989) for details) as suggested by Rausch *et al.* (1992) and Frink (1994). In ANUROOP, the pseudo-Laplacian weighted average is used for cell to node interpolation except at the boundaries, where the area-weighted average replaces it. At the boundaries there is not enough connectivity information to accurately calculate the pseudo-Laplacian weights for averaging .

2.3.2 Time Discretization

Subbareddy & Candler (2009) have proposed a fully discrete kinetic energy consistent finite-volume scheme, where an implicit extension of the Crank-Nicholson scheme has been used to conserve kinetic energy in time. However, this proposal entails substantial increase in the cost of computing fluxes and of higher storage requirements.

A more economical option is to use a total-variation-diminishing (TVD) scheme that does not allow kinetic energy to grow rapidly. Runge-Kutta 3 scheme based on Shu & Osher (1988) is one such scheme that has been used widely because of lower computation and storage requirements. The scheme also offers large scalability with ease of parallelization (Allaneau & Jameson 2009) and hence is suitable for DNS studies. In ANUROOP, this scheme is implemented as given below. For equation 2.13,

$$\frac{dU}{dt} + R(U) = 0$$

it takes

$$\begin{aligned} U^{(1)} &= U^{(n)} - \Delta t\, R(U^{(n)}) \\ U^{(2)} &= \frac{3}{4}U^{(n)} + \frac{1}{4}U^{(1)} - \frac{1}{4}\Delta t\, R(U^{(1)}) \\ U^{(n+1)} &= \frac{1}{3}U^{(n)} + \frac{2}{3}U^{(1)} - \frac{2}{3}\Delta t\, R(U^{(2)}) \end{aligned}$$

Calculation of Time Step

The time-step in an explicit scheme is restricted by the charcteristics of the underlying equations and also the grid. For an explicit scheme to be stable, the maximum time-step is calculated using the Courant-Friedrichs-Lewy (CFL) condition. This condition ensures that the flow on the stencil of a grid respects the physics. For the 1D Euler equations, the CFL condition for time step is given by

$$\Delta t = \sigma \frac{\Delta x}{|\Lambda|}$$

where $\Delta x/|\Lambda|$ is the time needed for information to propagate on a grid of size Δx with velocity Λ, and σ is a positive coefficient, known as the CFL number.

For Euler flows, Λ corresponds to the maximum eigen value in the convective flux Jacobian. For viscous flows, the spectral radius of the viscous flux Jacobian needs to be included in the calculation of maximum Δt as the flow in the boundary layer can severely restrict the maximum allowable time-step.

In ANUROOP (2D as well as 3D), the computation of maximum allowable time step follows the method given by Blazek (2005) for unstructured grids,

$$\Delta t_i = \sigma \frac{\Omega_i}{(\Lambda_{inv} + C\,\Lambda_v)_i} \tag{2.15}$$

Here Λ_{inv} and Λ_v represent a sum of Euler and viscous spectral radii of all the faces over all control volumes, and are given by:

$$(\Lambda_{inv})_i = \sum_{J=1}^{N_F} (|\vec{v}_{ij}.\vec{n}_{ij}| + c_{ij})\,\Delta S_{ij}$$

$$(\Lambda_v)_i = \frac{1}{\Omega_i} \sum_{J=1}^{N_F} \left[max\left(\frac{4}{3\rho_{ij}}, \frac{\gamma_{ij}}{\rho_{ij}}\right) \left(\frac{\mu}{Pr}\right)_{ij} (\Delta S_{ij})^2 \right]$$

Here $\vec{v}_{ij}.\vec{n}_{ij}$ and c_{ij} are the normal velocity and speed of sound on face J of cell i respectively; ΔS_{ij} and Ω_i are geometrical parameters representing area of face F and volume of cell i containing all such faces.

The constant C that multiplies the viscous spectral radius Λ_v is taken as 4 (recommended for central schemes), and the CFL number is kept below 1 for the time-stepping through out the computation.

2.4 Boundary Conditions

Figure 2.3 shows the computational domain used for flow past turbine blades. The computational domain for the blade is periodic in pitchwise as well spanwise directions. The blade surface is taken as an isothermal, no-slip wall.

Inlet, outlet, wall and periodic boundary conditions between the blades are implemented in ANUROOP. The values of primitive variables at the boundary are updated every time-step using the boundary conditions. All the boundary conditions are imposed by adding ghost cells (see Fig. 2.3)). For periodic boundary conditions, the values at the first interior cells of the first boundary are copied to corresponding ghost cells in the other periodic boundary and vice versa.

For wall, inlet and outlet, the details of the boundary conditions implemented in ANUROOP are given below.

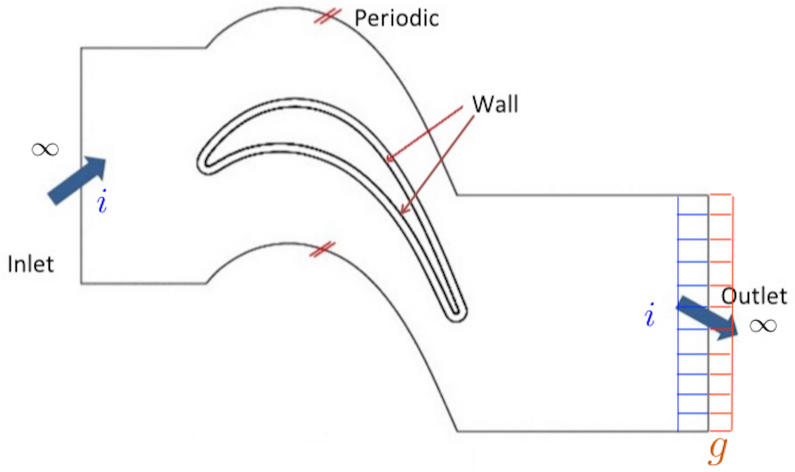

Fig. 2.3 Boundary conditions in computational domain of DNS of flow past a blade. i and g represent interior and ghost cells respectively. Ghost cells are applied at all the boundaries. ∞ represents values at free-stream.

2.4.1 Wall Boundary Condition

For the wall, a mirror boundary condition has been used, where the variables in the interior cells next to the boundary are mirrored appropriately to corresponding ghost cells and an average is taken to get the value at the wall face. For a no-slip stationary isothermal wall, the ghost values are as follows:

$$\begin{aligned} u_g &= -u_i \\ v_g &= -v_i \\ w_g &= -w_i \\ T_g &= 2 \times T_w - T_i \end{aligned}$$

where subscript i, and g stand for interior and ghost cells respectively. T_w is the imposed wall temperature.

The wall flux is obtained from the values at the wall, which is obtained after averaging the interior and ghost values as given above. The density is obtained using the continuity equation.

2.4.2 Inlet/Outlet Boundary Condition

The treatment of flow at the inlet and outlet is critical, since in the simulation an infinite flow domain is restricted to a finite computational domain. An improper boundary condition may

lead to unphysical oscillations near the boundary, which with progress in time may either lead to blow up of the code or give spurious results. It is necessary to avoid the reflection of the outgoing waves (from the computational domain) to ensure smooth inflow/outflow. To do this, primitive variables at the boundary can be extrapolated using characteristics variables (known as Riemann invariants) as given in Hirsch (1988). This implementation is popularly known as the Characteristics boundary condition or Non-reflecting boundary condition (NRBC) in the literature.

Since the propagation of waves is associated with hyperbolic equations, the viscous part in the Navier-Stokes Equations is dropped in calculating the wave characteristics. Poinsot & Lele (1992) have extended NRBC to include the effect of the viscous part in extrapolation of characteristic variables to get an altered pde near the boundary (this boundary condition is called NSCBC - Navier-Stokes Characteristics Boundary Condition). However the implementation of NSCBC is not straight forward for unstructured grids, as it requires gradients of primitive variables near the boundary. Also, since the viscous effect is not very prominent near the inflow/outflow faces, NRBC is commonly used in the literature (Bhaskaran (2010); von Kaenel (2003)) to get variables in these regions. As the details of NRBC are given in Hirsch (1988), only the implementation in ANUROOP is summarized here.

The Riemann invariants are calculated based on the values at the interior cells of the boundaries or the far-field values, depending on whether the characteristics point inwards or outwards.

For 3D Euler equations there are 5 eigen values (characteristics) of the Jacobian matrix, given by

$$\lambda_1 = u_\perp + c \tag{2.16a}$$

$$\lambda_{2,3,4} = u_\perp \tag{2.16b}$$

$$\lambda_5 = u_\perp - c \tag{2.16c}$$

where the subscript $\perp$ indicates the velocity normal to the boundary face, given by $\vec{\mathbf{u}} \cdot \vec{\mathbf{n}}$. Here $\vec{\mathbf{n}}$ is the outward normal.

These eigen values determine whether the wave is entering or leaving the domain. At the subsonic inlet ($-1 \leq M_\perp < 0$; $u_\perp < 0, c > 0, u_\perp < c$), there is one right-running wave ($u_\perp + c > 0$) and two left-running waves ($u_\perp < 0$, $u_\perp - c < 0$). At the subsonic outlet ($0 \geq M_\perp < 1$; $u_\perp > 0$, $c > 0$, $u_\perp < c$), there are two right-running waves ($u_\perp > 0$, $u_\perp + c > 0$) and one left-running wave ($u_\perp - c < 0$). The invariants corresponding to the right-running wave are calculated based on the values at the interior cells and those corresponding to the

left-running wave are calculated based on far-field values, as given below.

Subsonic inflow boundary

$$\psi_1 \equiv \psi_{1i} = \frac{2c_i}{\gamma-1} + u_{\perp i} \tag{2.17a}$$

$$\psi_2 \equiv \psi_{2\infty} = \frac{p_\infty}{\rho_\infty^\gamma} \tag{2.17b}$$

$$\psi_3 \equiv \psi_{3\infty} = \frac{2c_\infty}{\gamma-1} - u_{\perp\infty} \tag{2.17c}$$

Subsonic outflow boundary

$$\psi_1 \equiv \psi_{1i} = \frac{2c_i}{\gamma-1} + u_{\perp i} \tag{2.18a}$$

$$\psi_2 \equiv \psi_{2i} = \frac{p_i}{\rho_i^\gamma} \tag{2.18b}$$

$$\psi_3 \equiv \psi_{3\infty} = \frac{2c_\infty}{\gamma-1} - u_{\perp\infty} \tag{2.18c}$$

After the invariants are known, the values at the boundary face are thus extrapolated as

$$\begin{aligned} u_{\perp bf} &= \frac{\psi_1+\psi_3}{2} \\ c_{bf} &= \left(\frac{\gamma-1}{4}\right)(\psi_1-\psi_3) \\ \rho_{bf} &= \left(\frac{a_f^2}{\gamma\psi_2}\right)^{\frac{1}{\gamma-1}} \\ p_{bf} &= \frac{\rho_f a_f^2}{\gamma} \end{aligned}$$

$u_{\perp bf}$ is then again back-transfomed to get all 3 components of velocity at the boundary.

For the simulations with inflow turbulence, the turbulent fluctuations are superimposed on the mean value of the velocities as obtained from the boundary condition.

2.5 Parallelization

The code has been parallelized using standard Message Passing Interface (MPI). The open-source package METIS from Karypis Lab (see Karypis & Kumar (1998) for details) is used for dividing the computational domain into subdomains to run the code in parallel. METIS

does optimization of load as well as communication-balancing while dividing the grid into subdomains. Separate grid files are then written for each subdomain using the output by METIS. To each of the subdomains one processor is assigned. Ghost cells are added in each subdomain to store the variables passed by communicating subdomains.

In the present simulation for flow past an LPT blade, METIS is used on the 2D grid in the 2D computational domain, and then each subdomain is extruded in the spanwise direction for a specified number of intervals. A separate pre-processor (ANUROOP-Pre) is written that takes a 2D grid and returns a 3D grid divided into subdomains, along with ghost-cell information.

2.6 Concluding Remarks

This section describes the governing equations that are used to solve the flow past a turbomachinery blade. The compressible Navier-Stokes equations with proper non-dimensionalization are solved in a finite volume framework. Choosing this framework allows us to use arbitrary grids for flow over complicated geometries like turbine or compressor blade shapes. The numerical treatment of the energy equation respects the preservation of kinetic energy in space. Runge-Kutta 3 is used for time-stepping, so it makes the overall scheme semi-kinetic energy preserving. This scheme is found to be stable and robust for various kinds of problems. Separate codes for 2D and 3D flows have been developed. The code has been parallelized using standard MPI.

Chapter 3

ANUROOP: Validation and Verification

This chapter describes the verification and validation exercises carried out for ANUROOP. These exercises test the code for stability, accuracy and robustness of the schemes used. Validation study has been performed for 1D, 2D and 3D problems, for which separate codes are developed using same numerical schemes. Validation cases include problems with Mach number ranging from 0.1 to 1.5.

3.1 Flow past NACA0012 Airfoil

DNS of flow past NACA 0012 airfoil is performed for $Re = 10^5$ and angle of attack $\alpha = 4^\circ$. This verification case is the same as that described in Shan *et al.* (2005). This case study is to verify whether the code is able to capture the basic features of the boundary layer flow present at this angle of attack, for example, vortex shedding and Kelvin-Helmholtz (K-H) instability. This is important as boundary layer separation and transition are commonly found in engineering flows including in particular flow past turbine blades, and K-H instability is considered as the primary mechanism for triggering laminar boundary layer separation.

Figure 3.1(a) shows the computational domain as well as the grid used for the simulation. The upstream boundary is 3 chords away, whereas the downstream boundary is 2 chords away. The total grid size is 232800 and quadrilateral elements are used to make the grid. Simulation was initialized with uniform flow and without any external disturbance.

The signs of K-H instability can be seen in the axial-velocity contours of the simulation in Fig. 3.1(b). It is to be noted that this instability is generated purely because of the shear layer present, and by a self-excitation mechanism in the absence of any external disturbance in the simulation. However, the inherent numerical noise always present in a code would be sufficient to excite the necessary instabilities in the present case. These perturbations manifest later as vortex shedding behind the airfoil, as shown in the spanwise vorticity

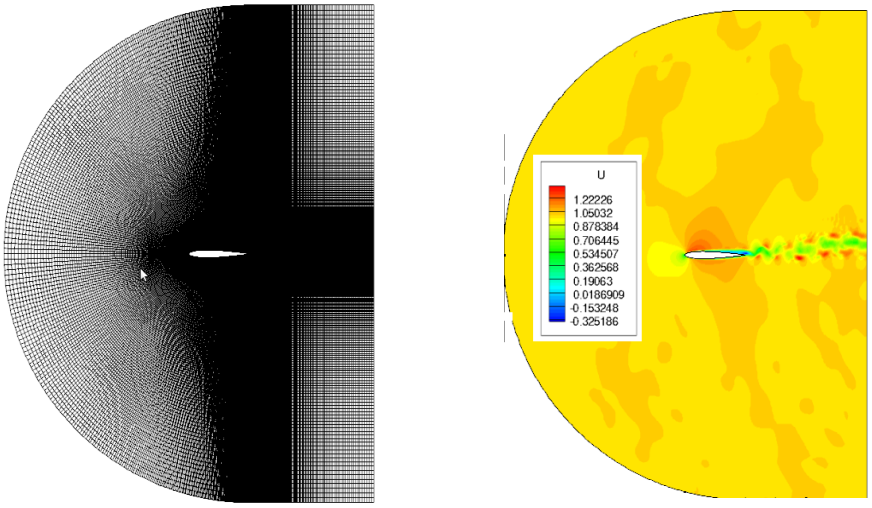

(a) (b)

Fig. 3.1 DNS of NACA 0012 airfoil. (a) Grid. (b) x-velocity contour. Note the signs of K-H instability in (b)

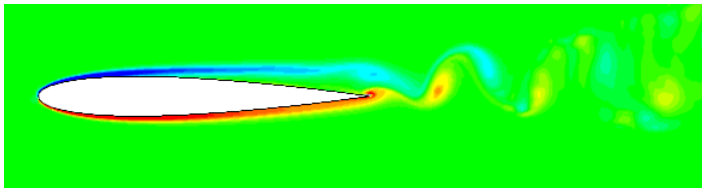

Fig. 3.2 Vorticity contours plot on NACA 0012. Vortex shedding can be noticed

contour plot in Fig. 3.2. At this point of time, the boundary layer separation is observed between $x/C = 0.38$ to $x/C = 0.845$.

3.2 The Sod Shock Tube

The Sod shock tube (Sod 1978) is one of the simplest cases to test the stability and accuracy of a compressible CFD code, and its shock-capturing ability. Figure 3.3 shows the schematic of the shock tube. Gases in the tube are separated by a diaphragm in the central plane, across which there is an initial jump in pressure and density. The length of the shock tube has been taken as 1 ($x = 0$ to $x = 1$), so that the initial discontinuity is at $x = 0.5$. The diaphragm bursts at $t = 0$, allowing the formation of the shock, contact discontinuity and expansion waves.

Conditions formulated by Sod (1978) have been used in the present case to solve this shock tube problem. The conditions on the left and right side of the shock-tube at $t = 0$ are given in Table 3.1.

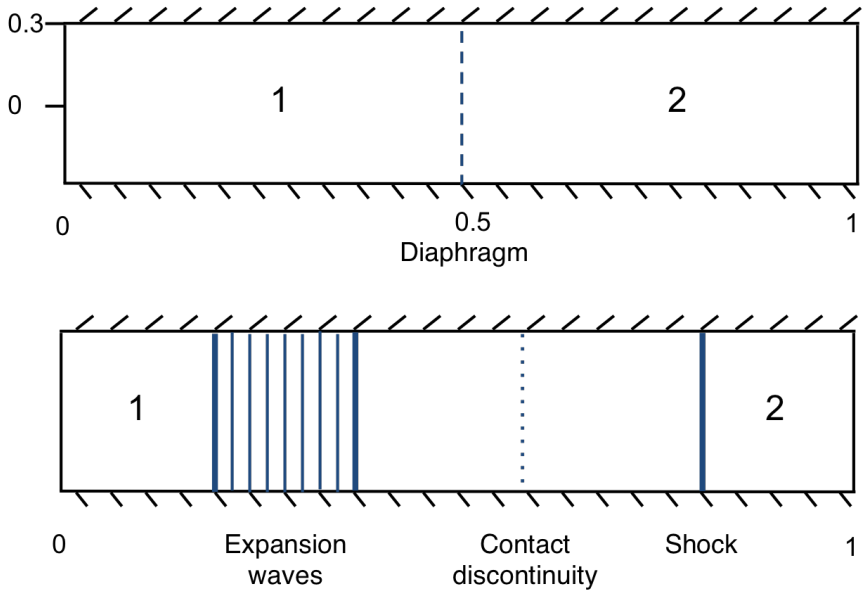

Fig. 3.3 Schematic of flow in a shocktube: Top: At $t = 0$, two gases at different pressures are separated by a diaphragm at the middle of the tube; Bottom: Generation of shock, expansion waves and contact discontinuity after the diaphragm breaks

For the one-dimensional (1D) shock-tube problem, an analytical solution (for inviscid flow) is available at any given time. The governing Euler equations are solved using the method of characteristics and Rankine-Hugoniot conditions. DNS computed solutions can be compared against analytical solutions to check the accuracy of the scheme.

For the simulations, since the initial velocity on either side of the tube is zero, the non-dimensionalized velocity in the equations is based on the speed of sound (see chapter 2). The shock tube length and the variables on the left side have been used as scales for non-dimensionalizing all quantities.

Table 3.1 Initial conditions for Sod shock tube

Variable	**left**	**right**
ρ	1.0	0.125
p	1.0	0.1
u	0.0	0.0

First 1D simulations have been performed to check the accuracy and stability of the KEP scheme used in the code. Later 2D simulations were performed to simulate a more complex set-up that gives more details about the structure of the shock.

3.2.1 1D DNS

1D simulations were performed for $Re = 25000$ using mesh cells ranging from 128 to 4096. Figures 3.4 and 3.6 show the variations of state variables at non-dimensional time $t = 0.2136$, respectively for coarse (512 cells) and fine (4096 cells) mesh simulations as compared with exact analytical results. Figures 3.5 shows zoomed view of Fig. 3.4 for better insight.

Results with coarse mesh simulations show oscillatory behavior near the discontinuities. This is because the physical viscosity ($1/Re$) near the discontinuity is not sufficient to stabilize the scheme . Unlike upwind schemes (Roe, VanLeer, KFVS etc.), the KEP scheme is based on central differencing, and hence at a coarse resolution numerical dissipation is not enough to damp out the oscillations. The shock has to be resolved with sufficient number of grid points to get a stable and accurate solution. For example, these oscillations disappear when the simulation is performed for 4096 mesh cells (see Fig. 3.6). Finally, Fig. 3.7 shows the comparison between solutions obtained with KEP and KFVS schemes. Being an upwind scheme, KFVS has enough numerical dissipation to obtain a non-oscillatory solution even with a very coarse grid (256 cells). However the solutions with KEP are much sharper, as is particularly visible in the vicinity of the shock. This is expected because KEP is much less dissipative compared to KFVS.

3.2.2 2D DNS

Two-diemsional (2D) simulations were performed for two Reynolds numbers, namely $Re = 2500$ and $Re = 25000$, based on the separation between two parallel walls h. As shown in Fig. 3.3, the shock-tube has an aspect ratio of $\alpha_s = h/L = 0.6$, where L is the length of the shock-tube. The set-up is the same as in Allaneau & Jameson (2009)). This is to ensure that the boundary layer on either side of the tube does not interfere with the flow at the centerline, so that the computed values at the centerline can be compared against 1D analytical results.

Only half of the domain was simulated and symmetry boundary condition was used at the centerline. The grid used for both Re simulations is the same, with 1024 cells in the x-direction and 128 cells in y-direction. The grid is stretched in the y-direction such that $\Delta y_{min} = \alpha_s/4000$. No-slip isothermal wall boundary condition was used at the top, while symmetry boundary condition was used at the bottom of the computational domain i.e. the centerline of the shock tube.

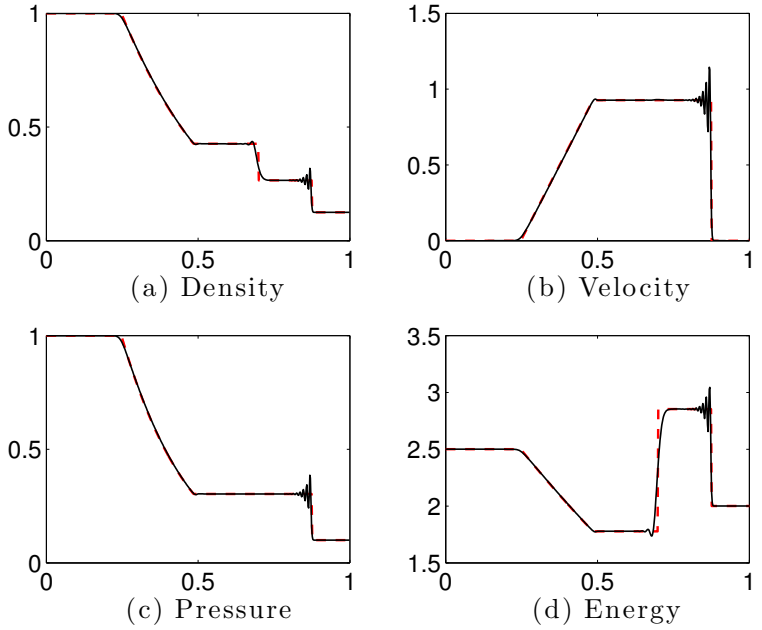

Fig. 3.4 1D Shock tube at $t = 0.2136$, $Re = 25000$: Red - Exact inviscid, Black - Computed using KEP Scheme(coarse mesh): 512 mesh cells

Figures 3.8 and 3.9 show a comparison of 2D shock tube results at the centerline with the exact inviscid solution at time $t = 0.213$. The results for $Re = 2500$ are smooth but results for $Re = 25000$ are highly oscillatory especially in the vicinity of the shocks. This suggests that the grid resolution used is sufficient for numerical stability for the $Re = 2500$ case (high viscosity) but not for $Re = 25000$. As shown in the 1D study in section 3.2.1, this instability will vanish at sufficiently fine resolution.

Alternative way to get a stable shock solution without oscillations using KEP (but without fully resolving the shock), is to use a dissipation switch near the discontinuities. Ducros *et al.* (1999) have suggested use of a pressure fluctuation sensor to detect the discontinuity, and then employ an appropriate (preferably 4^{th} order) dissipative flux, to be used at those points to get a smooth solution. Our main study of the flow past a LPT blade is subsonic (maximum Mach number 0.4), so the need to use such dissipative flux was not felt.

Figure 3.10 shows the pattern of flow through the shock tube as obtained from $Re = 25000$ simulations.Though unresolved, these patterns yield insights into boundary layer flow in the shock tube. These patterns strongly resemble those obtained by Allaneau & Jameson (2009) with their KEP scheme but with a finer grid. Allaneau & Jameson (2009) have given plausible physical explanations of these patterns, which we shall briefly outline now.

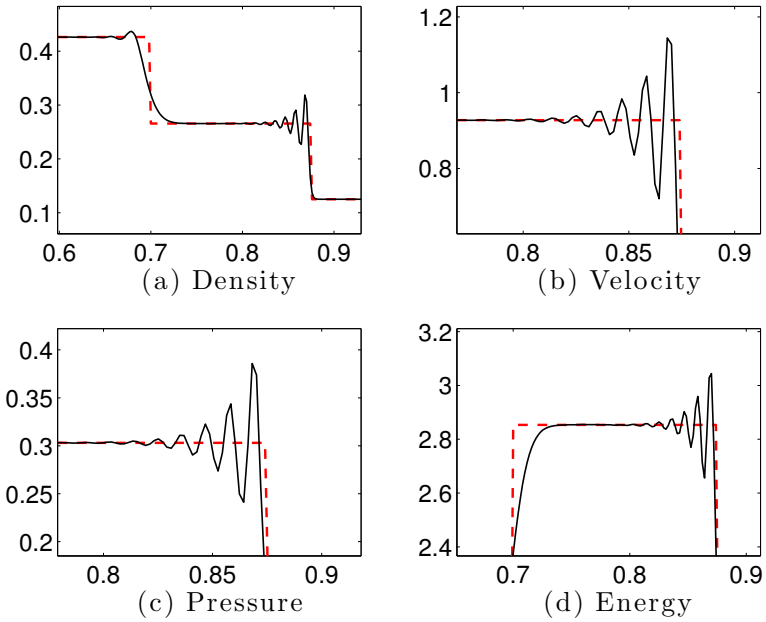

Fig. 3.5 Zoomed view of 1D Shock tube at $t = 0.2136$, $Re = 25000$: Red - Exact inviscid, Black - Computed using KEP Scheme(coarse mesh): 512 mesh cells. Note the fluctuations near the shock due to coarse resolution

The boundary layer on the wall is curved as may be seen in x-velocity (u) contours in Fig. 3.10. Pressure waves develop at the base of expansion and depression waves start at the base of the shock. These waves start in the boundary layer and are spread in the pseudo-steady (contact discontinuity) area. The shapes of these waves are clearly visible in the pressure contours. These structures are rendered visible by the very low numerical dissipation present in the KEP scheme.

Simulations were also carried out with unstructured triangular-element grids in the computational domain of the shock tube with aspect ratio of $\alpha_s = h/L = 0.3$ at $Re = 25000$. This was done to check the accuracy and stability of the code, as well as the implementation of schemes particular to unstructured grids (like gradient calculation using Green-Gauss). A moderate grid of size 0.2 million was used. The results at the centerline are compared against analytical results and are shown in Fig. 3.11. The kink in the plots near $x = 0.55$ is due to waves emanating from boundary layers crossing each other at this point due to low aspect ratio used in the simulation. The results confirm that the unstructured grid simulations are reliable.

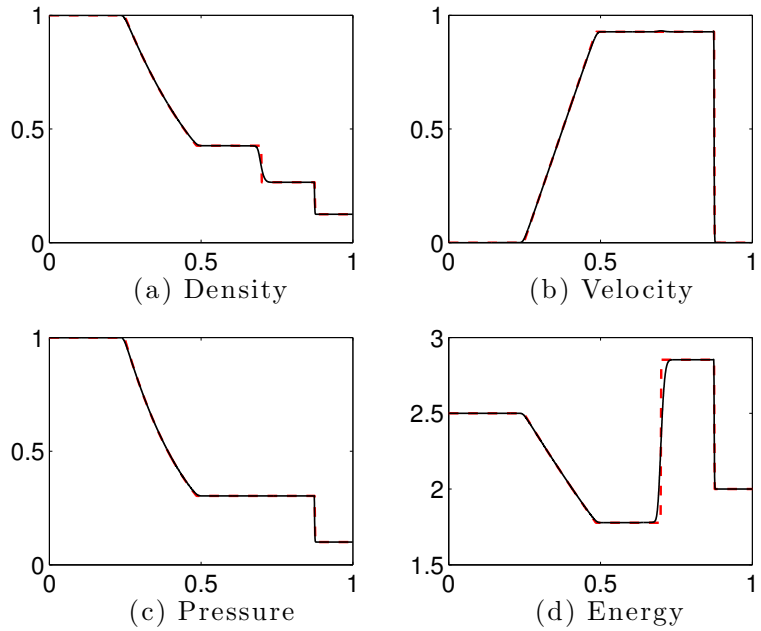

Fig. 3.6 1D Shock tube at $t = 0.2136$, $Re = 25000$: Red - Exact inviscid, Black - Computed using KEP Scheme: 4096 mesh cells

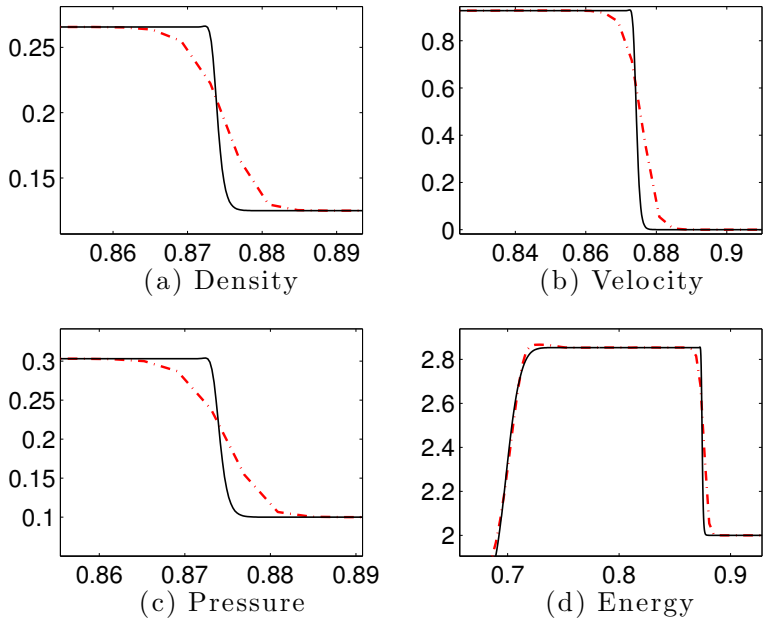

Fig. 3.7 Computed solutions of 1D Shock tube at $t = 0.2136$, $Re = 25000$: Red - KFVS Scheme (256 cells), Black - KEP Scheme (4096 cells). Unlike KEP, KFVS scheme is stable even for coarse grid. However results with KEP are much sharper near the shock

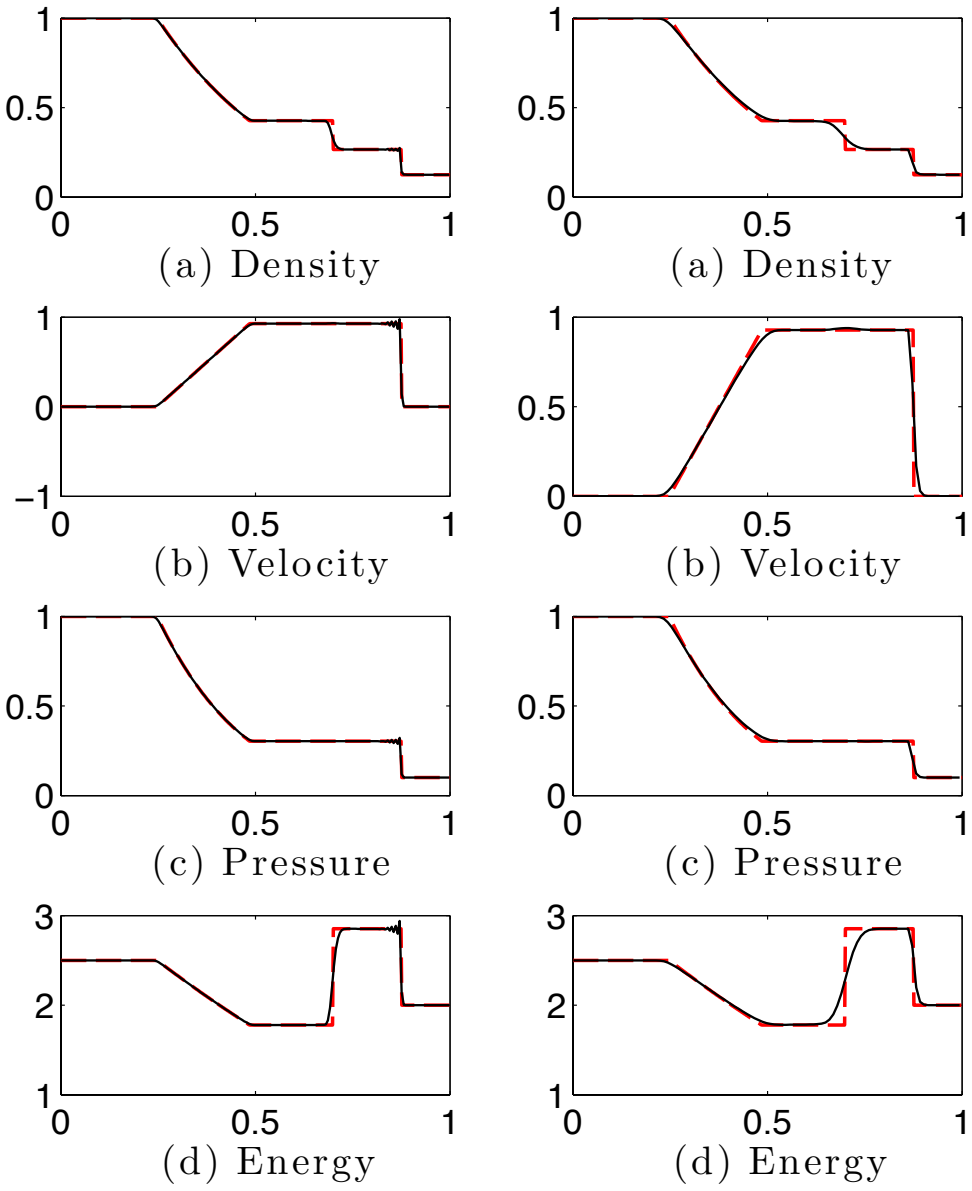

Fig. 3.8 2D Shock tube using KEP Scheme: variables plotted at the centerline of the tube at $t = 0.213$. Left: $Re = 25000$, Right: $Re = 2500$, Red - Exact inviscid, Black - Computed results

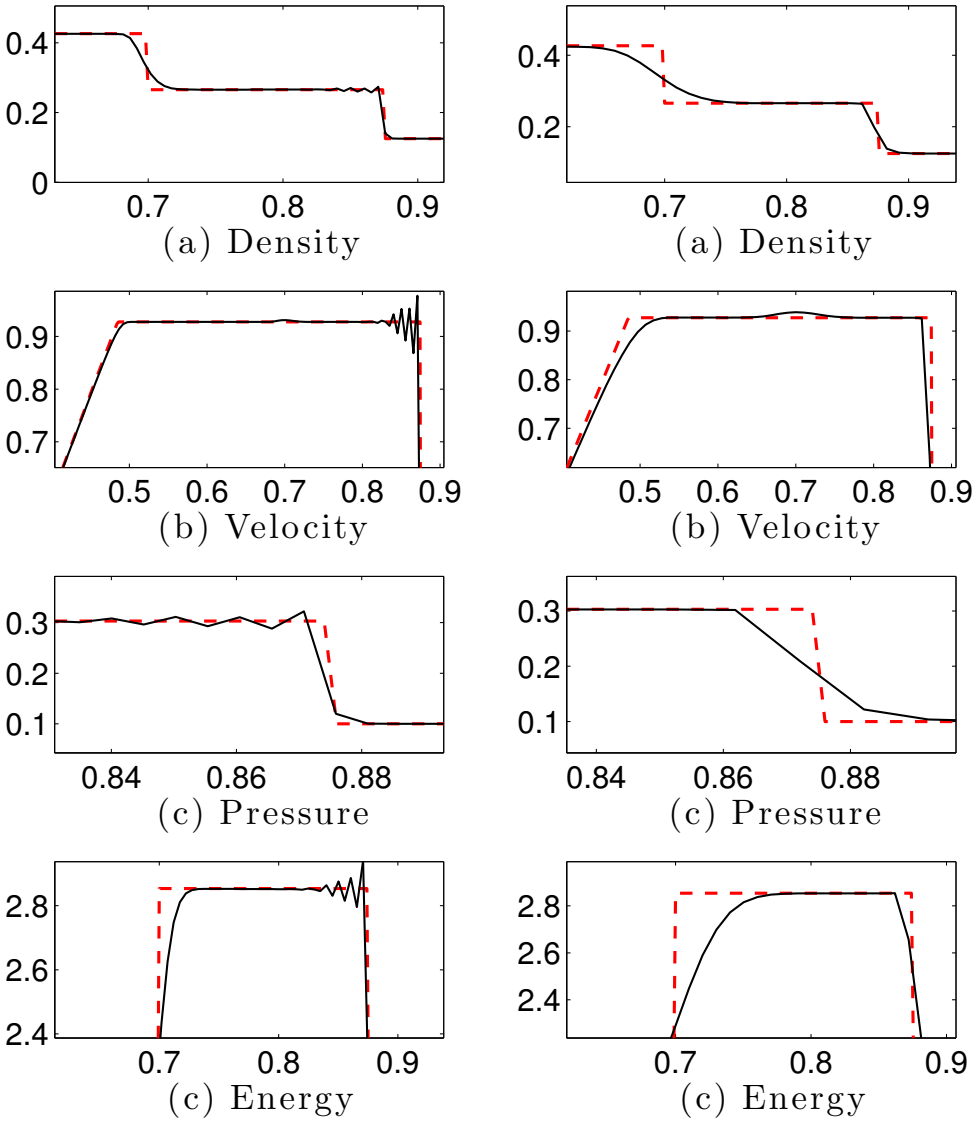

Fig. 3.9 2D Shock tube using KEP Scheme(Zoomed view): variables plotted at the centerline of the tube at $t = 0.213$: Left: $Re = 25000$, Right: $Re = 2500$, Red - Exact inviscid, Black - Computed results. Same grid used for both the simulations. Note the fluctuations near the discontinuities for $Re = 25000$. For $Re = 2500$, the results are smooth.

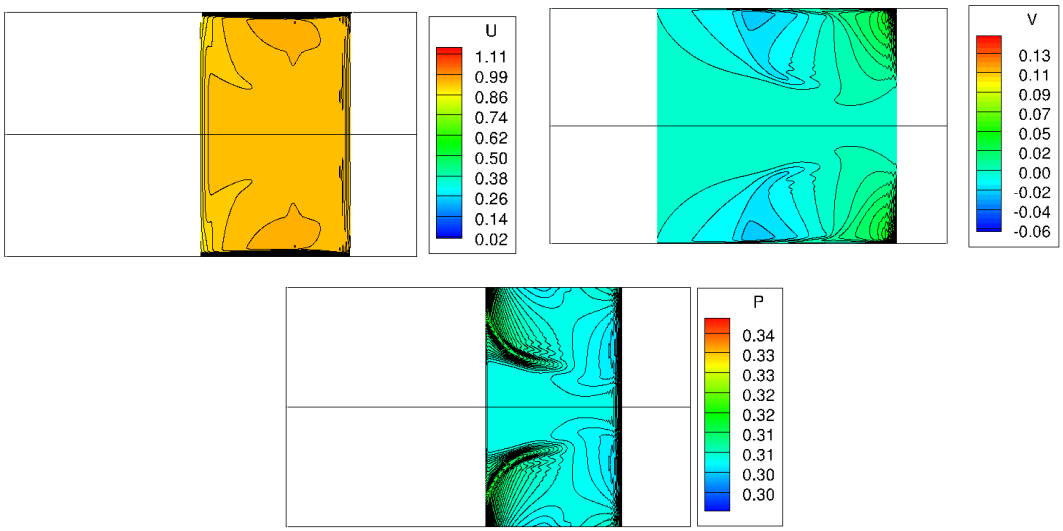

Fig. 3.10 Contours of velocity components u, v and pressure p for 2D Shock tube. $Re = 25000$

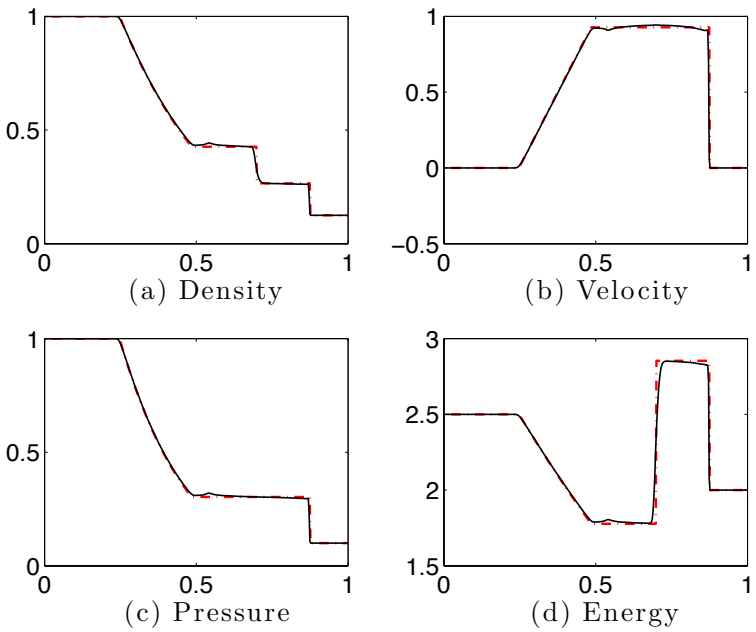

Fig. 3.11 2D Shock tube using KEP Scheme with unstructured grid: variables plotted at the centerline of the tube at $t = 0.213$. Red - Exact inviscid, Black - Computed results

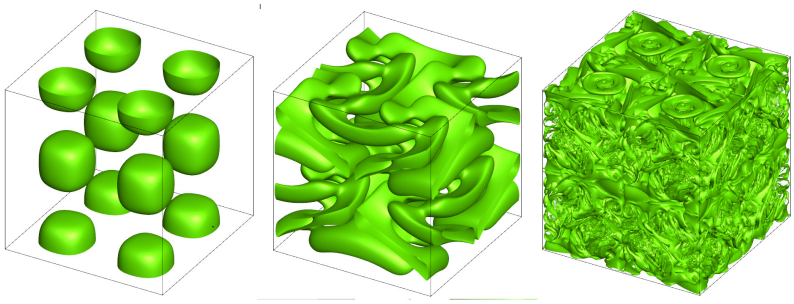

Fig. 3.12 Iso-surfaces of vorticity magnitude at t = 0.5, 2.0 and 13.0

3.3 The Taylor-Green vortex

The Taylor-Green vortex is an unsteady flow problem of a decaying vortex in a box proposed by G. I. Taylor and George Green. The flow inside a periodic box is initialized by simple perturbations of sines and cosines with zero-mean representing counter-rotating vortices, which decay with time at a rate governed by viscosity. An exact closed form solution can be constructed in 2D in the incompressible limit. The same problem in 2D can be extended to 3-D flows in the weakly compressible limit. Figure 3.12 shows the stages of the flow as time progresses. The pressure is initialized, as above, at a value corresponding to the solution of the pressure Poisson equation. The flow first goes transitional and later becomes fully turbulent, with the generation of small scales. Since there is no energy input, the flow soon starts decaying as in unforced homogeneous turbulence.

This is a good validation problem for a DNS code with simple initial and boundary conditions. In the present study, 3D DNS was performed to assess the robustness and temporal accuracy of the ANUROOP code, particularly the ability of the KEP scheme to capture the evolution of kinetic energy accurately.

3.3.1 Computational Setup

The Taylor-Green vortex flow is the evolution of a rotational velocity field in a triply-periodic cube $0 \leq x,y,z \leq 2\pi$, from the initial conditions:

$$
\begin{aligned}
u(0;x,y,z) &= U_{\text{ref}} \sin x \cos y \cos z \\
v(0;x,y,z) &= -U_{\text{ref}} \cos x \sin y \cos z \\
w(0;x,y,z) &= 0 \\
\rho(0;x,y,z) &= \rho_{\text{ref}} \\
p(0;x,y,z) &= p_0 + \frac{\rho_{\text{ref}} U_{\text{ref}}^2}{16} (\cos 2x + \cos 2y)(\cos 2z + 2)
\end{aligned}
$$

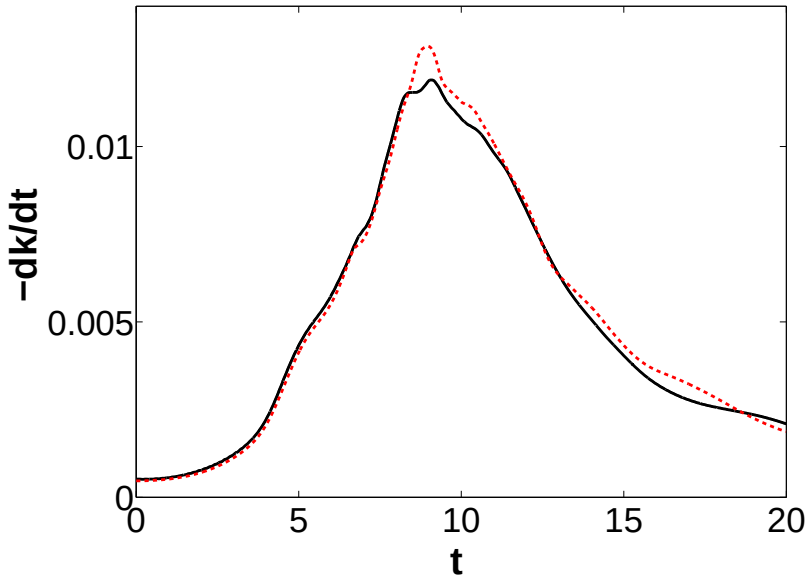

Fig. 3.13 Kinetic energy dissipation rate, compared with a 512^3 pseudo-spectral simulation Hillewaert (2012)(dashed lines)

Flow parameters set for the simulation are $Re = 1600$ based on the box length and the speed of sound, and $M = 0.1$. The initial Mach number M gives the value of p_0. The grid chosen for the current simulation is 256^3. The flow has been allowed to develop till $t = 13.0$, where t is the non-dimensional time based on L_{ref}/U_{ref}. This set-up allows comparisons with the earlier benchmark DNS (Hillewaert 2012) performed using psuedo-spectral method with 512^3 grid.

3.3.2 Results and Discussion

Figures 3.12, 3.13, 3.14 present results for the $Re = 1600$ simulation. Figure 3.12 shows iso-surfaces of vorticity magnitude ($|\bar{\omega}|$) as the flow evolves in time. It illustrates the cascade process, in which multiple scales are generated from a single initial large scale into very small scales due to non-linear interaction of eddies.

The kinetic energy of the system decays due to viscous dissipation. Figure 3.13 shows the rate of decay of kinetic energy as compared with the benchmark pseudo-spectral DNS results by Hillewaert (2012) on a 512^3 grid. The overall match is good and the maximum decay rate at $t \approx 9$ is captured. The peak on the decay rate predicated in the current simulation is slightly lower compared to the reference simulation. This may be due to the fact that the grid size used in current simulation is one-eighth of that used in the pseudo-spectral simulation. The temporal resolution here is also governed by the grid resolution.

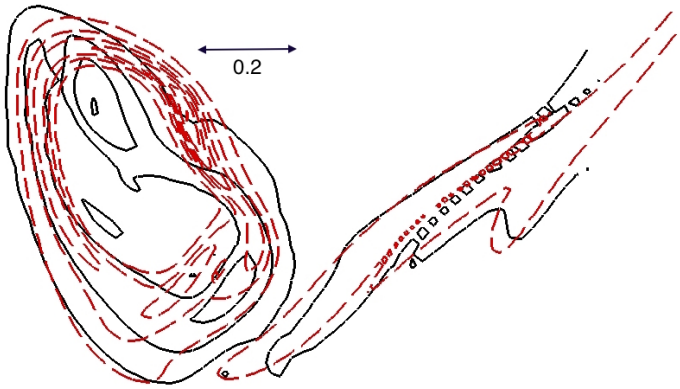

Fig. 3.14 Contours of non-dimensional vorticity magnitude of 5, 10 and 15 at $t = 8.0$ on one of the periodic faces ($x = 0$), compared with a 512^3 pseudo-spectral simulation Hillewaert (2012)(dashed lines)

Figure 3.14 shows contours of the non-dimensional vorticity magnitude on one of the periodic faces at $t \approx 9.0$ when dissipation is near maximum. The structures obtained in the current simulation are strikingly similar to those obtained by Hillewaert (2012).

Several other test simulations have been made over a range of $Re = 1000 - 3000$ to check the stability of the present semi kinetic-energy preserving central scheme. The simulations progressed without any difficulty in all cases, confirming the robustness of the code.

3.4 Supersonic Turbulent Channel Flow

DNS of compressible channnel flow has been performed to test the code against wall-bounded flows at finite Mach number. Past studies by Coleman *et al.* (1995) for an isothermal supersonic channel flow offer a good case for validation of the present code. Two plates separated by a width of $2H$ constitute the channel in which the fluid flows as shown in Fig. 3.15. The flow is statistically homogeneous in the streamwise (x) as well as spanwise(z) directions, and is driven by a body-force that keeps the mass-flux constant. Though this is just a validation exercise, results are presented in some detail.

3.4.1 Computational Setup

Problem Formulation

The main parameters governing the flow are Mach number and Reynolds number. Of the various cases described in Coleman *et al.* (1995), the one chosen here for the validation is at $M = 1.5$ and $Re = 3000$ (based on centerline velocity, viscosity at wall temperature, and

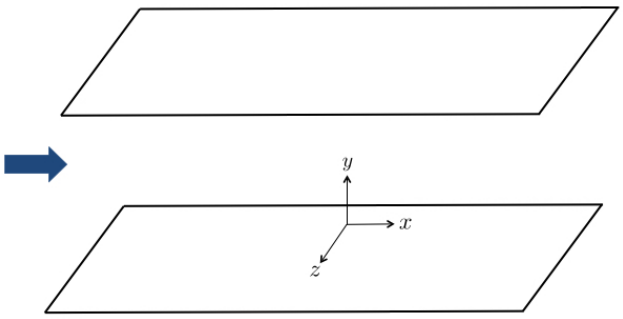

Fig. 3.15 Computational domain for channel flow

channel half-height H). Pr is kept constant at 0.7 throughout the flow and the viscosity of the fluid taken to vary according to the power law $\mu \propto (T/T_w)^{0.7}$, where T_w is the prescribed (constant) wall temperature.

Body-force terms have been added as sources in the momentum and energy equations in eqn. 2.9. The body force is varied with time to keep stream-wise mass-flux constant. Thus, the change in body-force after every iteration is given by-

$$\Delta B = \frac{(\int \rho u dy dz)_{\text{new}} - (\int \rho u dy dz)_{\text{old}}}{\int \rho dy dz} \tag{3.1}$$

Geometry and Grid

Figure 3.15 shows the computational domain used for the channel flow. The sides of the domain are $L_x = 2\pi, L_y = 2, L_z = 4\pi/3$. There are 100 grid points chosen in each direction to make the grid. The grid is uniform in streamwise (x) and spanwise (z) directions but stretching is used along wall-normal direction y to obtain a sufficiently fine grid to capture the turbulent boundary layer near the wall. The stretching is done using the hyperbolic tangent function as follows-

$$y_j = \frac{\tanh[c(2(j-1)/(n_y-1)-1]}{\tanh(c)} \tag{3.2}$$

where n_y is the total number of grid-points in the y-direction and c is a constant taken as 1.7 (as in Subbareddy & Candler (2009)). The range of y spans -1 to $+1$ with $y = 0$ at the centerline of the channel.

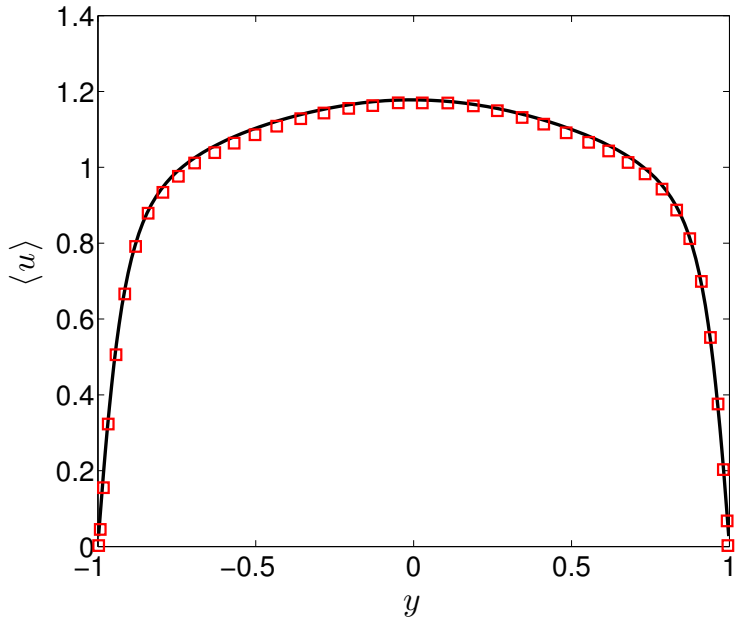

Fig. 3.16 Mean velocity profile. Symbols are values from Coleman *et al.* (1995) simulation

The simulation has been initialized with a parabolic laminar velocity profile superimposed with zero-mean white noise perturbations.

3.4.2 Results and Discussion

Instantaneous quantities have been time- and span-averaged to get the mean values. Favre-averaging that accounts for density variations is used to obtain the mean as follows:

$$\tilde{\phi} = \frac{\langle \rho \phi \rangle}{\langle \rho \rangle}$$

Here '˜' and '⟨⟩' denote Favre averaging and Reynolds averaging respectively. The fluctations around the mean are given by:

$$\phi'' = \phi - \tilde{\phi}$$

Mean streamwise velocity is shown in Fig. 3.16, compared with the spectral simulation results of Coleman *et al.* (1995). The figure shows good agreement between the two.

Table 3.2 compares various parameters computed from mean results, against the Coleman *et al.* (1995) simulation. The mean centerline velocity is 1.178 which is very close to the value 1.175 obtained by Coleman *et al.* (1995). Other variables listed in the table at the centerline as well as wall also show good match.

Table 3.2 Comparison of mean quantities with Coleman *et al.* simulation

Case	**Current simulation**	**Coleman *et al.***
$\langle u_c \rangle$	1.178	1.175
$\langle \rho_c \rangle$	0.979	0.980
$\langle T_c \rangle$	1.391	1.378
M_c	1.498	1.502
Re_c	2746	2760
$\langle \rho_w \rangle$	1.343	1.355
M_τ	0.081	0.082
Re_τ	216	222

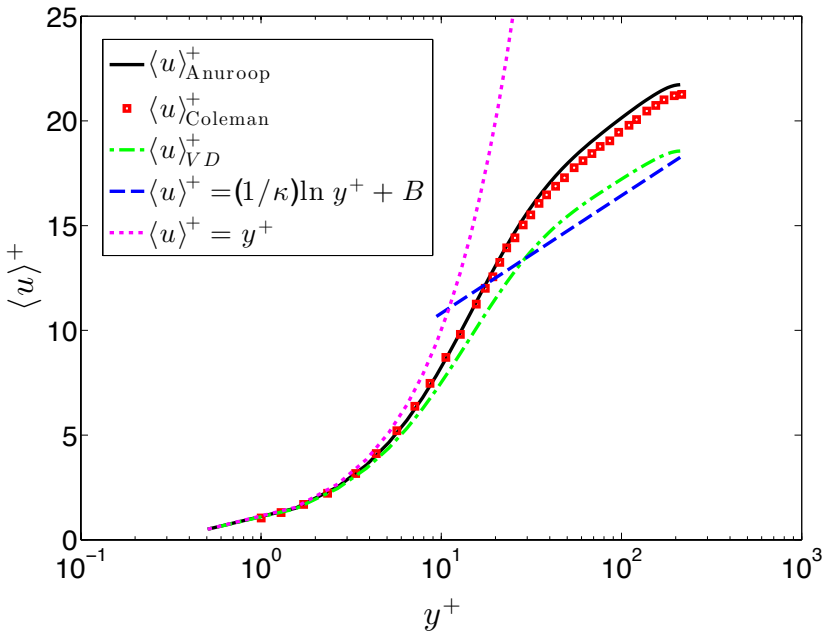

Fig. 3.17 Mean streamwise velocity profile in wall variables and the Van Driest transformation compared with incompressible law of the wall: $u_{wall} = y^+$, $u_{\log} = \frac{1}{0.41} ln y^+ + 5.2$

Figure 3.17 shows the mean velocity distribution in wall variables; u normalized by friction velocity u_τ and y with ν/u_τ. Present DNS results compare well with Coleman *et al.* (1995) results. The results are also compared with incompressible law of the wall for turbulent flows, which states that in the viscous sublayer region

$$u_{\text{wall}} = y^+ \tag{3.3}$$

and in the log-law region

$$u_{\log} = \frac{1}{k}\ln y^+ + B \tag{3.4}$$

In the literature, one will find slightly different values for the constants that appear in the above equations. The values so quoted would be in the neighbourhood of the following numbers:
Extent of viscous sublayer

$$y^+ < 5$$

Extent of log-law region

$$y^+ > 40,\ y/H < 0.2$$

Von Kármán constant

$$k = 0.41$$

Intercept

$$B = 5.2$$

(These numbers are taken from Davidson (2015)).

The region between the viscous sublayer and beginning of the log-law region ($5 < y^+ < 40$) is known as the buffer layer. This is the transition region where viscosity-dominated flow changes to turbulence-dominated flow, and none of the laws mentioned above is applicable in this region. The outer layer begins at $y^+ > 50$, where the effects of viscosity on mean parameters begin to be negligible and extends to $y/H = 1$. This region is governed by velocity-defect law due to Von Kármán (1931), who also proposed the log-law (Eqn. 3.4). The log-law region however satisfies both the law of the wall and outer defect law (the overlap region). Coles (1956) after careful study of boundary layer data later proposed a single universal law for turbulent wall-bounded flows, known as law of the wake, that accounts for law of the wall, log-law and velocity-defect law in respective regions.

In both ANUROOP and Coleman *et al.* (1995) simulations, $< u >^+$ agrees well with the law of the wall in the viscous sublayer, however in the log-law region, both differ from the log-law significantly. For the high mach number flows, where density variation is very high,

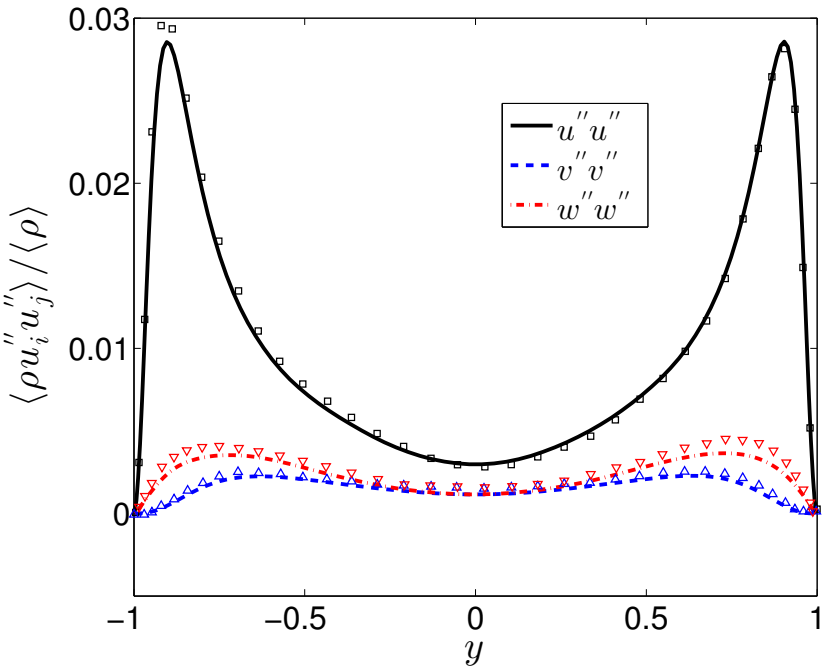

Fig. 3.18 Turbulent normal stresses ($\langle \rho u'u' \rangle$). Symbols are values from Coleman *et al.* (1995) simulation

variables are not expected to follow the incompressible laws. However a density-weighted transformation of mean velocity, known as the Van Driest transformation, can be used to enable this comparison. This transformation is given as:

$$\langle u \rangle^+_{\mathrm{VD}} = \int_0^{\langle u \rangle^+} \left(\frac{\langle \rho \rangle}{\rho_w} \right)^{\frac{1}{2}} d\langle u \rangle^+ \tag{3.5}$$

This transformed velocity is expected to satisfy the incompressible log law (Bradshaw (1977))

$$\langle u \rangle^+_{\mathrm{VD}} = \frac{1}{k} \ln y^+ + B \tag{3.6}$$

The above law is also plotted in Fig. 3.17 and it can be noted that this transformation brings the profile closer to incompressible log-law, however in the overlap region ($5 < y^+ < 10$) the agreement becomes worse. Wei & Pollard (2011) argue that a power law is a slightly better and less dependent on Mach number than the log-law in this region.

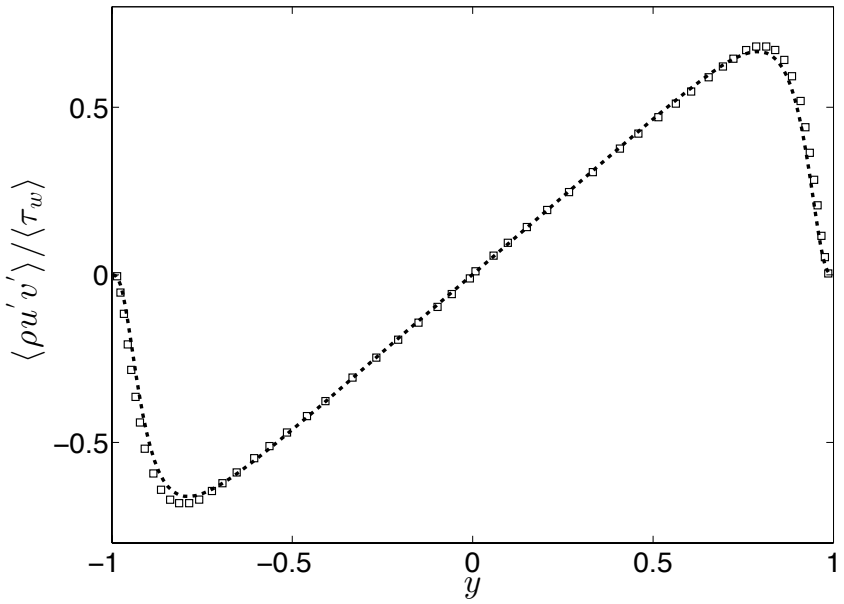

Fig. 3.19 Reynolds stress normalized by the wall-shear stress. Symbols are values from Coleman *et al.* (1995) simulation

Higher Order Statistics

Higher order statistics are obtained using the Favre-averaged fluctations. Figure 3.18 compares the mean turbulent normal stresses $\langle \rho u' u' \rangle$ for 3-velocity components with Coleman *et al.* (1995). Reynolds stress normalized by wall-shear stress is plotted in Fig. 3.19. Both these plots show a very good match with Coleman *et al.* (1995) results. This confirms the ability of ANUROOP to accurately predict the higher-order statistics for a wall-bounded turbulent flow.

Finally for the sake of completeness, the two-point correlation in the streamwise and spanwise directions for density and three velocity components close to the wall are plotted in Fig. 3.20. As observed in Coleman *et al.* (1995), the spanwise correlation is roughly equivalent to the incompressible results (Fig. 2 in Kim *et al.* (1987)) but greater coherence in seen in streamwise correlation because near-wall streaks become more aligned as the Mach number increases. This alignment is again visible in the wall normal vorticity contour very near to the wall as shown in Fig. 3.21. This picture is strikingly similar to that given in Coleman *et al.* (1995) and shows near-wall streaks getting aligned due to high Mach number effects compared to the meandering in incompressible flows (Kim *et al.* 1987).

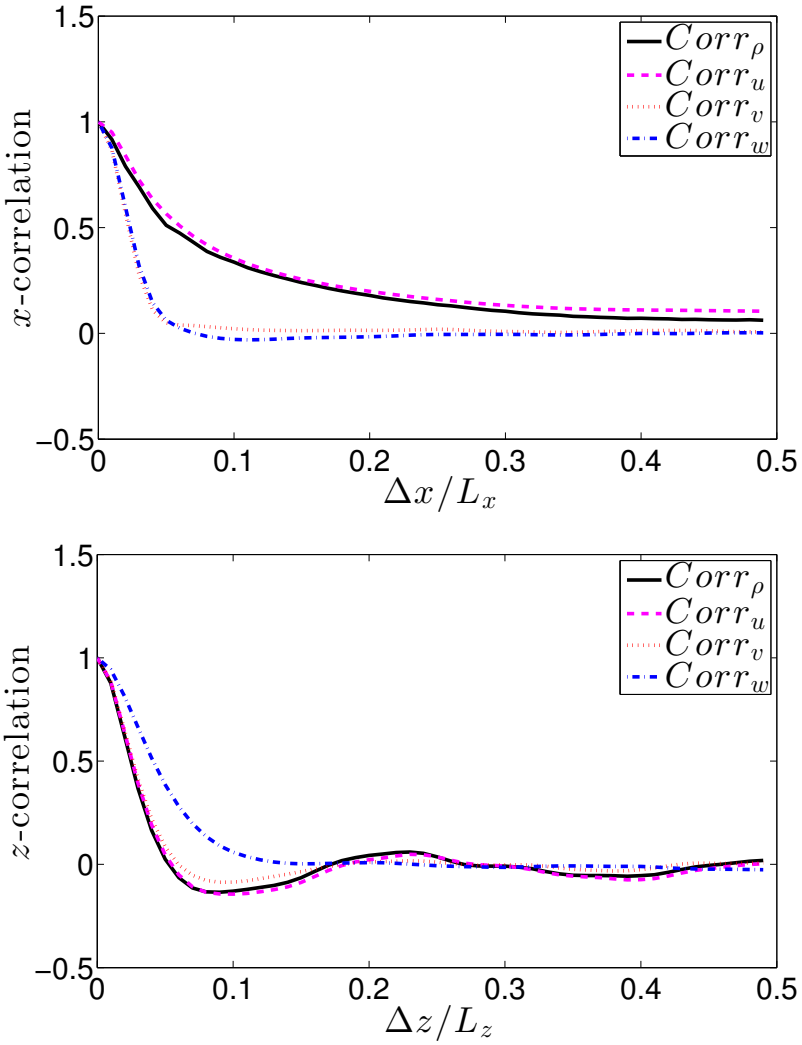

Fig. 3.20 Two-point correlation for density and three velocity components at a distance of 0.04 from the bottom wall, ; Top: Streamwise; Bottom: Spanwise

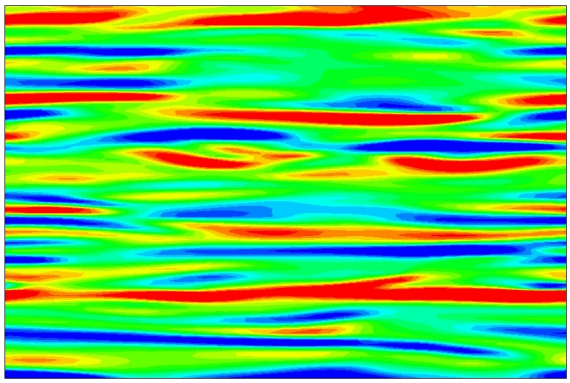

Fig. 3.21 Contours of wall normal vorticity on $x-z$ planes a distance of 0.04 from the bottom wall

3.5 Concluding Remarks

A rigorous validation of code ANUROOP is performed using several test cases that include a shock tube, the Taylor Green vortex and fully developed turbulent channel flow. The code has been found to be robust in all these three studies. The results are compared with the data available in the literature to ascertain the accuracy of the code for further DNS studies. Particularly, the verification of the code for the kinetic energy evolution with time (Taylor Green vortex) and the validation of turbulent statistics for channel flow impart confidence that the code can be used for a more complex problem like the flow past a turbine blade, which is the focus of this thesis.

Chapter 4

LPT Simulations: Numerical and Computational Aspects

This chapter describes the numerical and computational aspects of the simulation of flow past an LPT blade using ANUROOP. The experiment, on which the present DNS study is based, is also described in detail.

4.1 Experimental Details of Test Case

The experiments reported by Stadtmuller (2002*a*) provide the flow parameters used in the present DNS study. The tests were performed at the High Speed Cascade Wind Tunnel of the Universität der Bundeswehr, München, Germany. The purpose of this study was to provide test data at low *Re* suitable for DNS studies. Relevant geometric data of the T106A blade used in the cascade (see Fig. 4.1) are given below:

Chord Length	l	=	100 mm
Axial Chord Length	l_{ax}	=	85.86 mm
Blade Height	h	=	176 mm
Pitch ratio	t/l_{ax}	=	0.9306
Stagger Angle	β_s	=	59.28°

Figure 4.1 also shows the set-up used for for the experiment on the T106 blade. The cascade consists of 7 blades and uses the blade at the center for the main measurements. Static

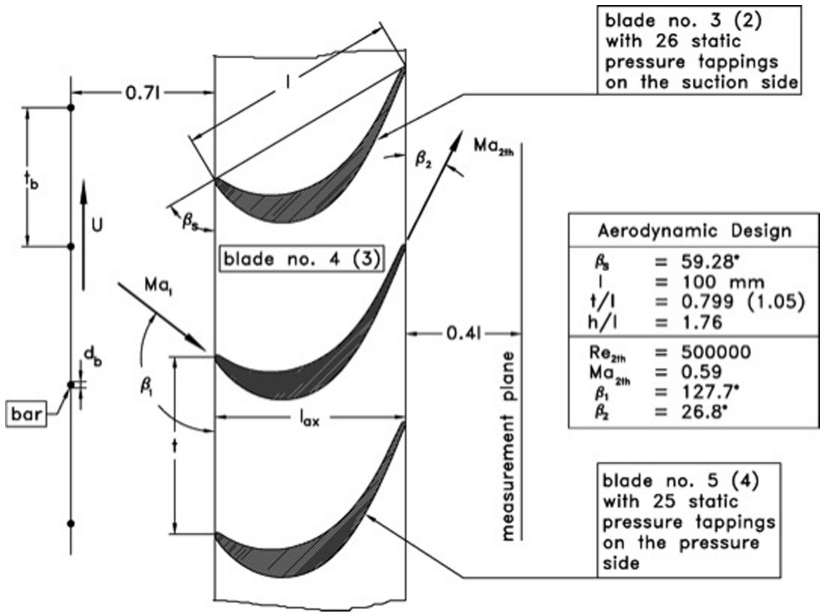

Fig. 4.1 Sketch of experiment performed by Stadtmuller on T106A cascade (Reproduced from Stadtmuller (2002*a*))

pressure tappings were used on adjacent blades for profile loading measurements. The boxes in the figure list the geometric and aerodynamic parameters at design point conditions, which are different from those at the operating point investigated for the reported measurements, according to Stadtmuller (2002*a*).

The experiments were performed in a steady upstream flow (no disturbances) as well as with upstream wakes created by a moving bar wake-generator. However, the present computational study confines itself to steady-state measurements. The detailed description of the present test set-up can be found in Stadtmuller (2002*a*). The parameters from these experiments are given in Table 4.1. Note that only exit parameters were measured in the experiments, and the reference Mach and Reynolds numbers at the inlet are calculated using isentropic relations assuming isentropic expansion between inlet and exit.

The surface pressure measurements and hot-film traces indicate a separation bubble on the suction side surface close to TE, however it not clear whether the bubble reattaches before the TE. Also there is considerable uncertainty over the exact inlet angle that must be used for the computational study. This is because the wake generator ahead of the cascade changes the geometric inflow angle ($\beta_{geo} = 37.7°$) considerably. Based on RANS simulations and 3D hot wire measurements, Stadtmuller (2002*a*) has estimated the real inlet flow angle as 45.5°. The report also mentions the uncertainty in the estimates of the background free-stream turbulence intensity (FSTI), and once again a RANS study was performed to estimate the actual turbulence level.

Table 4.1 Parameters from Stadtmuller (2002*a*) experiment (Steady-state measurements)

Parameter		**Exit (2)**	**Inlet (1)**
Static pressure (Pa)	p	6950	7340
Total pressure (Pa)	p_t	7770	7770
Total temperature ($^\circ K$)	T_t	312.9	312.9
Reynolds number	$Re_{l_{ax}}$	51800	-
Mach Number	M	0.404	0.286
Geomteric inlet flow angle ($^\circ$)	β_{geo}	-	37.7

Accurate information on these two parameters (inflow angle and FSTI) is crucial for comparisons with any computational results, but unfortunately no other experimental data (at low enough *Re* for carrying out DNS) is available to us in the open literature. Fortunately however, this experiment has been the basis for many DNS studies (though at relatively lower resolution) listed in chapter 1, and hence enough computational results are available for comparisons with the present work .

4.2 Simulation Details

In the absence of precise data on experimental conditions, the literature on computational studies provides some useful estimates for parameters to be adopted in the present simulations. DNS by Wissink (2003) provides a full set of parameters except for the mach number (which was not relevant for his work as incompressible flow was assumed). This set is adopted for the present computational studies. The inlet Mach number was hence decided by iterative DNS simulations at low resolution at which the outlet Mach number achieved is the same as in the experiments. The full set of parameters adopted for the computational studies are given in Table 4.2. Note that *Re* here is based on inlet flow velocity and axial chord length of the blade.

Table 4.2 Parameters used in simulations

Parameter		Value
Inlet flow angle (°)	β_1	37.7 - 45.5
Inlet Reynolds number	$Re_{l_{ax}}$	51800
Inlet Mach Number	M_1	0.15
Inlet temperature	T_1	300

On the surface of the blade, no-slip isothermal boundary condition has been imposed. For most of the simulations, the temperature of the blade wall T_w is taken as 1.1 of the incoming flow temperature T_∞.

Apart from using a completely compressible formulation, the present DNS differs from previous studies in its major focus on the boundary layer on the blade surface than on the passage between the blades. To achieve this, a different kind of grid topology is essential. This is described in detail in the next section.

Because of the focus on the boundary layer, it is appropriate to call the present DNS as "Boundary Layer DNS" as the full Navier-Stokes equations in the whole domain (including the boundary layer) have been solved. This distinction is useful because of the debate in the literature about the 'exact' definition of DNS, and the resolution needed for a simulation to be called as DNS. As pointed out by Spalart *et al.* (2011):

> "No DNS is exact, and the appropriate resolution depends on the purpose of the study, including the region of interest, the quantities of interest, and probably other features."

4.2.1 Computational Domain

The computational domain, illustrated in Fig. 4.2, covers the flow around a blade with periodic boundary conditions that simulate the row of blades at top and bottom. All the dimensions are scaled on the axial chord length (l_{ax}) and free-stream velocity (U_∞). The parameters governing the flow and all other quantities are also non-dimensionalised based on these scales.

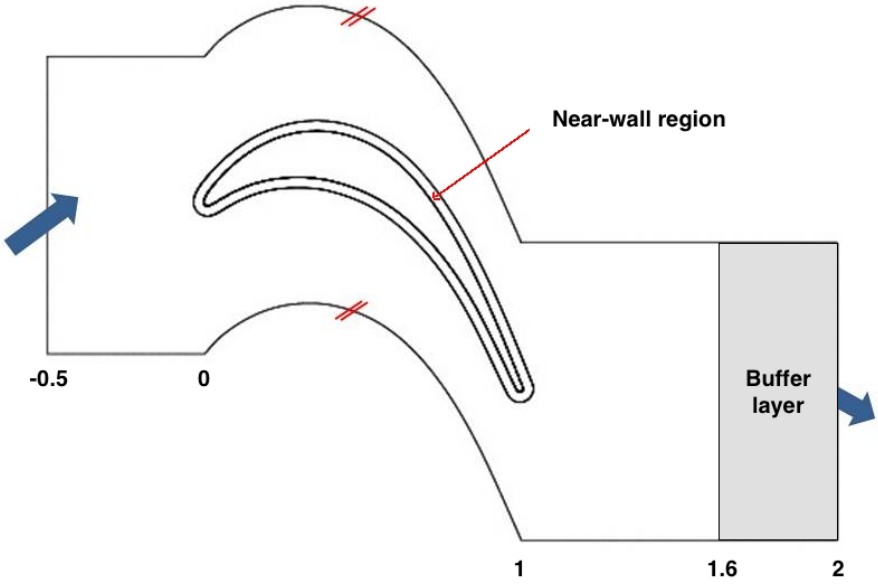

Fig. 4.2 Schematic of the computational domain used for flow past T106A blade

The outflow plane is located at a distance of one axial chord l_{ax} downstream of the TE, and the inflow plane is at a distance of half the axial chord upstream of the LE. The pitch between the blades is $p = 0.9306\, l_{ax}$ or $0.799\, l$, and periodic boundary conditions are applied everywhere on the boundary in the pitchwise y-direction as well as the spanwise z-direction. As already mentioned, a no-slip isothermal boundary condition is applied at the blade surface.

The domain shown for the mid-section of the blade is extruded in the spanwise direction for $0.2 l_{ax}$, which has been found in earlier studies to be sufficient for obtaining the mean 2D flow at the mid-section. Characteristics-based boundary conditions (see chapter 2) are used at inflow and outflow. A relaminarizing buffer layer, defined in section 5.6, is used adjacent to the outflow plane as shown in Fig. 4.2.

Uniform flow hits the inflow plane at the inflow angle β_1 given in Table 4.2. Some of the simulations have been performed with FSTI, the uniform flow being superimposed with appropriate turbulent fluctuations (which are solutions of pre-computed homogeneous isotropic turbulence) before they hit the inflow.

4.2.2 Grid Topology

The elliptic scheme used in earlier work (Wu & Durbin (2001); Kalitzin *et al.* (2003); Wissink (2003); Wissink *et al.* (2006); Michelassi *et al.* (2002)) offers little control over grid generation in the interior. Kalitzin *et al.* (2003) have reported a large number of skewed elements in the passage near the TE using this scheme, due to strong curvature of the blade and requirement of periodicity in the pitchwise direction. Their results near the LE also exhibit the effect of singularity in the mesh due to a forced H-mesh. Wissink (2003) has reported the effect of streamwise resolution on the accuracy with which the separation bubbles can be resolved.

Because of these observations and the present emphasis on the boundary layer, more control and flexibility on the grid near to the wall was sought on the following three aspects:

- Orthogonal mesh without any singularity near the blade wall
- Control on boundary layer grid with respect to the first grid-point near the wall and the successive ratio (SR) between consecutive grid elements in the wall-normal direction
- Control on streamwise resolution without unduly increasing the overall grid size

It is difficult to meet all these requirements in the elliptic mesh approach, especially because of the periodicity of the mesh elements in the y-direction. To meet the above requirements, it is useful to first divide the domain into two regions: 'near-wall' and 'outer' (Fig. 4.2). The commercial meshing tool Gambit 2.4.6, the pre-processor of ANSYS® Fluent 6.3.26, is then used to form a grid in the 2D face, which was then extruded in 3D using an in-house preprocessor. The co-ordinates of the mid-section of the T106A blade, given in Stadtmuller (2002*a*), are imported into Gambit. The edge is created from these vertices using NURBS (Non-Uniform Rational B-Spline) with degree 3. NURBS gives a high degree of smoothness in defining a curve such that its second derivative is zero at the endpoints.

The curve is then split into pressure and suction sides, and each side is further split into 3 parts: LE, mid-section and TE. This was done to get control on the distribution of mesh elements to be assigned near the high curvature regions (LE and TE) and on the rest of the blade. A geometric distribution is used near the edges and a bi-geometric distribution is used in the middle with a defined successive ratio between each mesh division (Table 4.3 and Fig. 4.3). The mesh parameters were chosen to ensure that there is no abrupt jump between neighbouring segments.

The computational domain is then built around this blade. In the near-wall region, an orthogonal mesh is built using the boundary layer tool available in Gambit by specifying

the first grid point away from the wall, the successive ratio and the number of rows. These parameters are listed in Table 4.3.

Figure 4.4 shows this grid near the LE and TE respectively. Note that this mesh fits nicely to the body and there is no singularity at either leading or trailing edge.

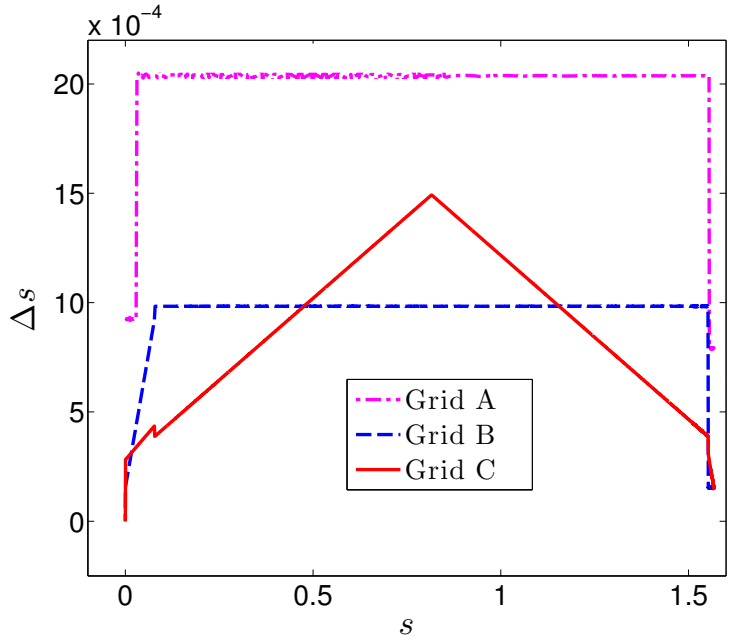

Fig. 4.3 Mesh spacing in suction side boundary layer (streamwise)

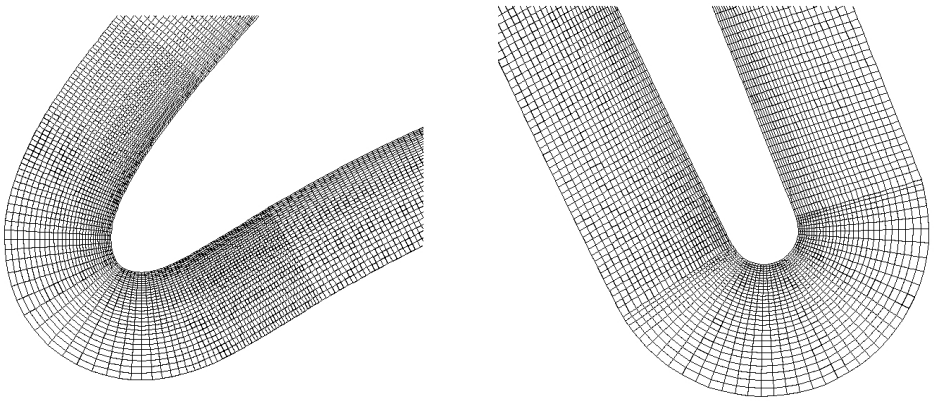

(a) (b)

Fig. 4.4 Boundary layer grid near (a) leading edge, (b) trailing edge

After the near-wall mesh is ready, the outer region is filled with quadrilateral elements ensuring proper mesh distribution along the rest of the edges. Periodicity is enforced in

Table 4.3 Grid used in simulations. N_s: Total no. of elements on 2D section of the blade, N_{nw}: No. of rows in the near-wall region, $\Delta\eta_1$: First wall distance, SR: successive ratio, NWT: Total thickness of near-wall region. Δs^+, $\Delta\eta^+$, Δz^+ are distances in wall units in streamwise, normal and spanwise directions

Grid	N_f	N_z	Size (M)	N_s	N_{nw}	$\Delta\eta_1$ $(\times 10^4)$	SR	NWT	Δs^+	$\Delta\eta^+$	Δz^+
A	384,164	64	25	1526	15	5.9	1.05	0.0127	4	1.2	6
B	740,088	64	47	3322	120	2.3	1.02	0.113	3.5	0.8	6
B1	740,088	128	95	3322	120	2.3	1.02	0.113	3.5	0.8	3
C	1,257,162	128	161	4140	200	0.93	1.005	0.032	1.1	0.1	2
T	150,764	32	5	950	30	5.8	1.05	0.039	9.5	1.1	12

the pitchwise y-direction, so that elements are exactly copied along the periodic edges. It requires a few iterations to get the desirable mesh with good mesh quality and no abrupt jump. More than 50% of the total number of mesh elements are confined in the near-wall region.

The 2D mesh was then exported to 'Fluent 5/6' format, which was then imported into an in-house pre-processor (anuroop-PRE). This pre-processor first extrudes this 2D mesh into 3D for a given number of intervals, then calls the open-source partitioning tool METIS (Karypis & Kumar 1998) to divide the mesh into the desired number of subdomains. Finally the data is written for individual subdomains in ANUROOP format. The ghost cell information needed for the interface boundaries between subdomains is also written at this stage.

4.2.3 Grid Details

Table 4.3 provides the details of the grids used for the present simulations. The mesh parameters used to create near-wall grid are also given; Δs^+, $\Delta\eta^+$, Δz^+ indicate distances in wall units in the streamwise, normal and spanwise directions respectively for simulations with $Re = 51831$. Thus $\Delta\eta^+$ is the first grid-point distance in the normal direction, Δs^+ is the streamwise distance between nearest elements in the mid-chord region of the blade, and Δz^+ is the interval between adjacent elements in the spanwise direction (constant throughout).

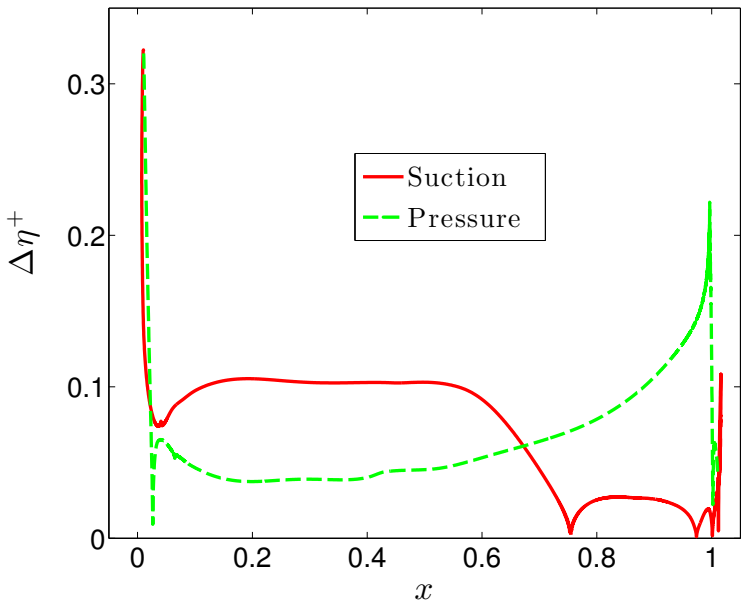

Fig. 4.5 $\Delta\eta^+$ distribution for simulation with grid C. $Re = 51831$, $\beta_1 = 45.5°$

Unlike in other grids, the computational domain of grid A includes the passage between two successive blades, rather than the flow-region around a single blade. The former has been the general approach till recently in computations of flow past bodies to describe the same physical flow in computation. A computational domain around a single blade gives more flexibility in creating a suitable near-wall mesh and hence has been used in later studies. Grids B and B1 use the same face mesh and differ only in the number of intervals in the spanwise direction (64 and 128 respectively). This was used to study the effect of the spanwise mesh. Simulations show no major difference between 64 and 128 intervals, and only results with B are reported in this thesis. The 128 intervals in grid C have been used to avoid skewness in the mesh elements because of the very fine mesh used in the face. Grid T is the test grid used for preliminary simulations at various inflow angles, different FSTI and Reynolds number.

Grid C is the finest ever grid used to-date for DNS in a turbine blade flow. Figure 4.5 shows the distribution of the first layer distance in wall units for a simulation (at $Re = 51831$, $\beta_1 = 45.5°$) performed with this grid. The grid refinement in the boundary layer ensures that the first layer distance in wall units Δn^+ is below 0.1 throughout the blade for this simulation. The results with this extra-fine grid are somewhat surprising, and also differ significantly from other grids, as will be described and explained in the next chapter.

It is to be noted that the highest resolution used earlier for simulation, performed with a 2nd-order accurate numerical method at the present *Re*, was 17 million (see Table 1.2 in

chapter 1). As the flow on the suction side is more complex, the streamwise resolutions for the suction side of the blade for different grids are shown in Fig. 4.3.

4.2.4 Computational Facilities and Runs

Simulations have been performed at the top computational facilities available in India. The cluster available Nalanda at JNCASR was used for preliminary simulations. Large simulations were performed at supercomputing facilities available at C-DAC, Pune and CSIR-4PI, Bangalore. The details of these facilities are given in Appendix A. All the simulations have been performed using only CPUs without any accelerators.

The time step employed is of the order of $10^{-5}L/U$ corresponding to CFL $\approx$ 1.0, where L and U are the length and velocity scales used in defining Re. With this step-size, one simulation with grid C takes around 10 days with 1024 Intel Xeon E5-2670 (Sandybridge) 2.6 GHz processors (22 peak TFLOPs) for the flow to progress 10 flow-times. Each processor writes its own results file that includes global cell id and variables ρ, u, v, w, P. A post-processor can read all these files and generate a single file for full domain or a section based on the global ids. Post-processing is performed using a workstation with 128 GB RAM and Nvidia Quadro K40 graphics card. Tecplot® software is used for post-processing most of the results.

4.3 Computational and Numerical aspects

4.3.1 Relaminarizing Buffer Layer near Outflow

The preliminary simulations that were performed on the blade resulted in blow-up as soon as the flow hit the outflow boundary. A closer investigation has shown that fluctuations that were built-up inside the computational domain due to physical instabilities of the flow get reflected for this problem near the outflow boundary (as the outflow could not be located much farther downstream in order to avoid excessive grid requirement for DNS), and hence the simulation crashes. A common remedy is to increase the viscosity so as to damp out the fluctuations in the vicinity of the outflow. Wissink & Rodi (2006) have used a buffer region in their DNS of flow in a turbine cascade.

In the present simulations, the viscosity is gradually increased to 10 times the physical viscosity in the buffer region defined $1.6 \leq x \leq 2$ (see Fig. 4.2). This increase in viscosity however restricts the allowable time-step in explicit time-stepping.

4.3.2 Inflow Turbulence and Wake

While some simulations have been performed with FSTI, the emphasis has been trying to understand the structure of the solution, in particular its dependence on numerical parameters such as resolution. The reason for doing this is the questions on the effect of resolution have to be sorted out before one can obtain a reliable numerical solution of the Navier-Stokes equations.

We have performed some simulations with FSTI of 2.5%, 5% and 10% on the finest Grid C. This method of specifying free-stream turbulence (FST) is the same as explained in Kalitzin *et al.* (2003) and Wissink & Rodi (2006), except that no wake disturbance is added at the inlet. The FST is the pre-computed solution of a decaying homogeneous isotropic turbulence in a box at a given time (Wu & Moin (2009); data provided by Prof. Parviz Moin, Stanford University, and kindly lent to us by Prof. O. N. Ramesh, Indian Institute of Science). This solution is first scaled to the desired intensity and then the grid on one of the periodic faces of the box is matched to the inlet grid of the computational domain by appropriate stacking. At $t = 0$, the solution on this face is superimposed on the mainstream flow at the inlet of the blade domain. These disturbances are added only to the velocity field and not to pressure and density. At each time-step thereafter, the solution on the blade is advanced by Δt, and the downstream face of the box is correspondingly moved by a distance $\times U\Delta t$. It may be noted that at each time-step the solution is interpolated inside the box, before being superimposed on the free-stream. Once $n \times U\Delta t$ (n is the iteration number) becomes greater than the box side length, the cycle is repeated from the leading face of the box.

As FST is always provided at the inlet, its intensity decays till the flow reaches the proximity of leading edge. In our exercise, it was noticed that for FST with intensity upto 10% at the inlet, the disturbances near the LE were insufficient to trigger transition in the boundary layer flow. The mean structure of the solution thus obtained was not very different from that with the clean inlet. It may thus require a higher intensity of free-stream turbulence level or a different approach to specify the disturbance levels in such transitional boundary layer simulations. Describing the appropriate initial conditions in a well-resolved DNS to get desired solution at transitional *Re* is a subject of current research.

With regard to wakes, it is well-known that they change the structure of the transition process. However these disturbances produced by a travelling row of cylinders do not really strictly mimic the very complex disturbance environment in a real turbine, where the wakes may come from more than one stage upstream and so will have gone through a complex process of being chopped by several rows of blades. It would be quite difficult to reproduce it numerically in DNS. This explains our focus on the basic problem of resolution.

4.3.3 Averaging of the Flow

Simulations are allowed to progress for a duration that corresponds to a flow that has moved about 8-10 chord lengths at the inlet velocity. The mean quantities are obtained by averaging over the samples after the flow has moved about 5 chord lengths, and also by averaging in the spanwise direction.

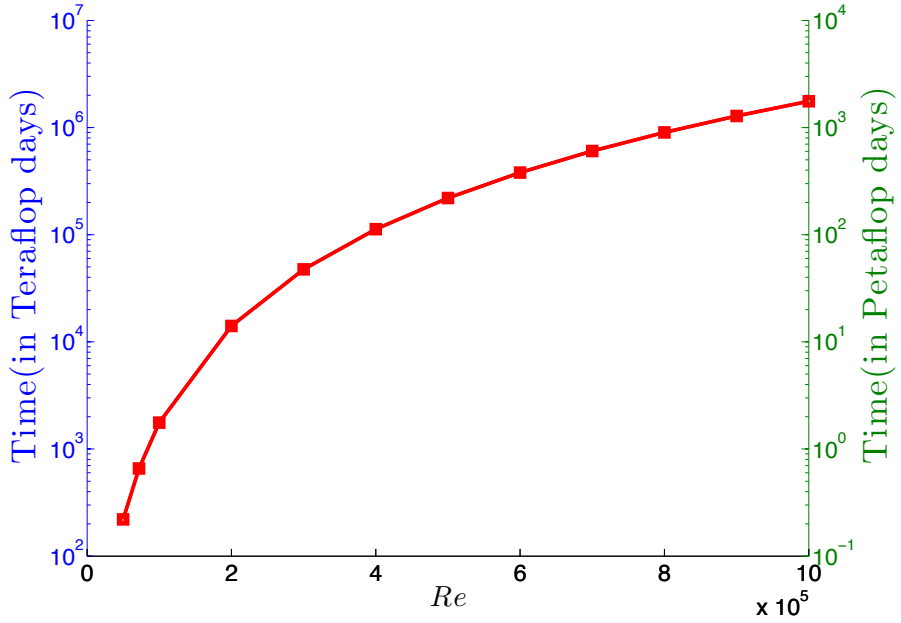

Fig. 4.6 Estimated time in Teraflop and Petaflop days for simulations at different *Re* using ANUROOP

4.4 Computing Power Requirement

The compute power requirements for a range of *Re* are given in Fig. 4.6. The time is estimated based on the experience gained with the present simulation at $Re = 51,831$. Though the *Re* for a gas turbine may go as low as 20,000 for some specific conditions during cruise, the demand of compute power for a high-lift condition at which *Re* can go to the order of a million is much more demanding. For example using the present code ANUROOP, it will take around 220 days on a petaflop machine to get fully resolved DNS results at a *Re* one-order higher than what we are currently doing. This may seem huge, but can be well-within reach if the code can be made to exploit the power of hybrid-computing such

as GPUs and MIC co-processors. A preliminary study suggests that the use of GPUs may accelerate the code upto 30 times.

Further the present calculation is made using the highest grid resolution of 160 million at $Re = 51831$. From the literature available this may seem like overkill, however grid-sensitivity in DNS is one issue that still needs to be debated in detail. The next chapter provides a flavour of grid sensitivity issues from the results that we have obtained, and explains why it is important.

4.5 Concluding Remarks

The experimental and numerical details for flow on the T106A blade are provided in this chapter. The emphasis of the present work is study of the boundary layer in detail through DNS, and hence a grid topology is adopted where separate grids are used for the boundary layer region and rest of the domain. The grid parameters are listed in detail. Mainly three grids (A, B and C) at very different resolutions are used for the grid sensitivity studies. The results are presented in the next two chapters.

Chapter 5

LPT Simulations: Fluid-dynamical aspects

This chapter describes some of the fluid-dynamical aspects of the flow on the LPT blade. The chapter begins with grid-sensitivity issues which are shown to affect even features of the mean flow. It is shown how bulk parameters such as the pressure coefficient $c_p(x)$ can be greatly affected by the choice of the grid.

The mean separation bubbles, when present, are characterized by a suitable pressure gradient parameter. The difference between the mean and instantaneous flows in this context is also highlighted.

Analyses of the present DNS results have been performed here mainly on four aspects that seemed quite striking. These analyses throw light on critical aspects of the complex flow that is particular to a gas turbine blade. The analyses also reveal aspects of the fluid-dynamical "zoo" shown in chapter 1 , in this particular case the flow past an LPT blade at high incidence. For two aspects - namely the curvature effects and relaminarization, the present DNS results have been compared with the existing theories. These comparisons assist in assessing current ideas, and may be useful to the modelling community in developing better tools.

Some of the aspects considered in this chapter require much more rigorous analysis demanding both resources and time, and are beyond the scope of the present thesis. They are presented here to give an overall flavour of the complex flow on the blade; and more detailed analyses are left to future work.

5.1 Grid Sensitivity Issues

Mean results obtained with the present simulations are found to be very sensitive, when the incidence angle is $\beta_1 = 45.5°$ (well above the design incidence angle $\beta_1 = 37.7°$). For simulations at the design incidence ($\beta_1 = 37.7°$) though, the major features of the mean flow remain unaffected irrespective of the grid used. As shown in Fig. 5.1, there is no separation bubble at the LE at this incidence. However a closed bubble is always found near the trailing edge (discussed below in section 5.3), which is consistent with findings in the literature, e.g. Sarkar (2007, 2009).

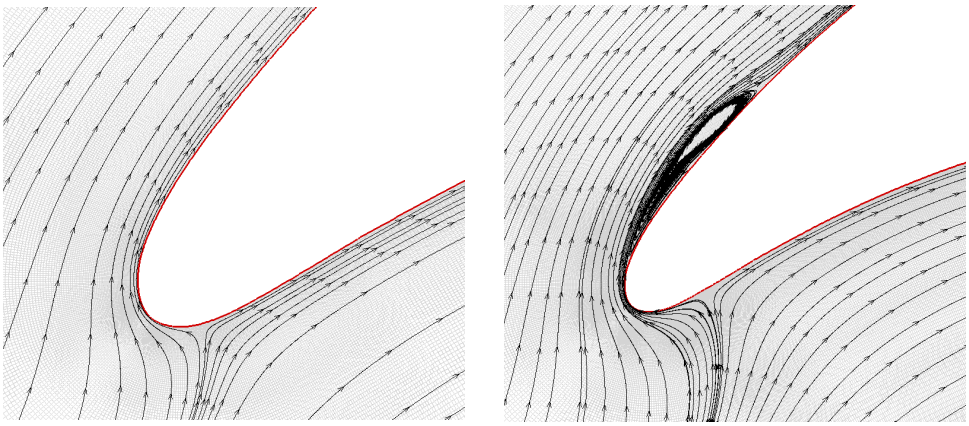

(a) (b)

Fig. 5.1 Streamlines of mean flow for simulations (Grid B). $\beta_1 = 37.7°$ (left) and $\beta_1 = 45.5°$ (right) at the LE. There is no separation for at the LE for $\beta_1 = 37.7°$ for any grid.

At the higher incidence of $\beta_1 = 45.5°$, inconsistency was found in the appearance of LE separation bubbles among different grid results. Before going in to the this issue, it is worthwhile to revisit the position in the literature on similar studies. Table 5.1 lists the experimental and computational studies on T106A at this incidence. Though there are LES and RANS studies as well (see Chapter 6), the list here is limited to DNS studies to highlight the difficulties in simulating flow at high incidence.

Table 5.1 is converted to a plot in Fig. 5.2 for easy reading. It is obvious from the plot that the observations, in particular regarding the separation bubble near the LE, are not consistent among the different investigators.

In the experiments of Stadtmuller (2002*a*), TE separation is evident from the quasi wall-shear stress measurement, however it is not clear if the flow reattaches. At the LE, no separation is reported. The quasi wall-shear stress data (for clean as well as wake inlet) also does not indicate any sign of separation. Michelassi *et al.* (2002) however suggest that the LE separation may be missing because of the relatively long distance between the measurement

Table 5.1 Separation in T106A blade flow studies

Group	Type of study[a]	Grid size	Numerical method[b]	Inlet type	Separation		Remarks
					LE	TE	
Stadtmuller (2002*a*)	Expt.	-NA-	-NA-	clean	unclear	yes	Not clear if the TE separation bubble reattaches or not
				wake	unclear	yes	
Michelassi *et al.* (2002); Wissink (2003); Wissink *et al.* (2006)	INS	17 M	2^{nd} order FV	clean	yes	yes	Streamwise resolution affects the flow. Bubble size increases with increase in fluctuations
				wake	yes	yes	
				wake[c]	yes	yes	
Ranjan *et al.* (2013, 2014, 2016)	CNS	25 M	2^{nd} order FV	clean	yes	yes	
		95 M		clean	yes	yes	
		160 M		clean	no	yes	
Michelassi *et al.* (2015)	CNS	18 M	Compact FD + Fourier	clean	yes	yes	Incoming wakes suppress LE separation bubble
				wake	no	yes	
				wake	no	yes	
Garai *et al.* (2015)	CNS	0.48 M[d]	2^{nd} order DG	clean	yes	yes	
		3.84 M	4^{th} order DG	clean	no	yes	
		30.72 M	8^{th} order DG	clean	no	yes	

[a]INS: Incompressible Navier-Stokes, CNS: Compressible Navier Stokes, equations used for solving the flow-field
[b]FV: Finite volume, FD: Finite difference, DG: Discontinuous Galerkin
[c]Large scale fluctuations are removed from the wake
[d]$(n/p) \times (n/p) \times (n/p)$ DG grid roughly equivalent to $n \times n \times n$ FV, FD grids (Nogueira *et al.* 2009)

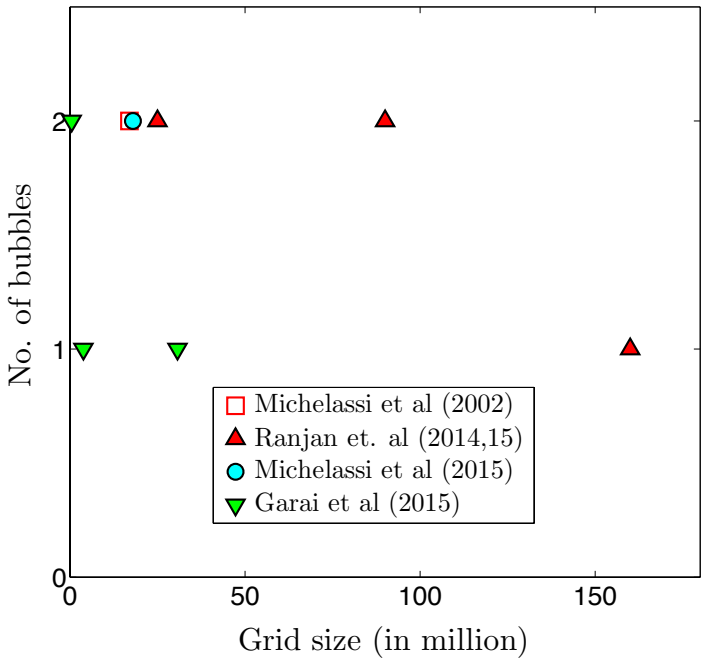

Fig. 5.2 Number of separation bubbles in the mean flow. Open symbol represents incompressible simulation

points. They pointed out the kink in the c_p plot of Stadtmuller (2002*a*) near the LE may be a sign of possible separation. They also observed that the LE separation might be affected by the uncertainties in the experimental inlet flow angle.

In the DNS simulations of Michelassi *et al.* (2002), Wissink (2003) and Wissink *et al.* (2006), the LE separation bubble is always seen for clean as well as wake inlet. The URANS and LES simulations reported by Michelassi *et al.* (2002) also show separation near the LE. They have also reported that the separated shear layer rolls up in two separate bubbles due to a K-H instability, a phenomenon also observed in our relatively coarse resolution (grids A, B, B1) studies.

The more recent DNS simulations (Michelassi *et al.* 2015; Garai *et al.* 2015) are all compressible with more complex numerical methods. For Michelassi *et al.* (2015), a small scale separation bubble is noticed near the LE on the suction side for the clean inlet simulation; however the bubble disappears when the wake is added. This, they suggest, is because the wake changes the effective inflow angle. In the case of Garai *et al.* (2015), this LE separation bubble, which is present in lower-order simulations, disappears completely at the highest order (as inferred from the skin-friction distribution).

In our simulations performed with four different grids (Ranjan *et al.* 2013, 2014, 2016), the separation bubble at the LE is present for grids A,B and B1, but disappears in the highest resolution simulation (grid C). It is to be pointed out here that the resolution of grid C (160 million grid points) is about 5 times higher than the second highest compared to all other studies at this *Re* (Table 5.1). Also for our simulations, utmost care was taken in defining the blade curve from the co-ordinates given in the report by Stadtmuller (2002*a*), to avoid any roughness due to the shape.

5.2 Mean Pressure Distribution

In the studies of Michelassi *et al.* (2002), Wissink (2003) and Wissink *et al.* (2006), where LE separation bubble is present, there is a significant deviation in the prediction of pressure on the suction side compared to experiments. The attributed reasons for this difference in c_p are uncertainty in inflow angle and compressibility effects not included in DNS simulations. They have also acknowledged the effect of streamwise resolution (Wissink (2003)) but the results reported are for a resolution (given in Table 5.1) which was claimed to be sufficient for the study at $Re = 51831$.

The blade loading (c_p) is well-predicted on both sides of the blade in the studies of Michelassi *et al.* (2015) and Garai *et al.* (2015), however they differ in the presence of an LE separation bubble as mentioned in the last section.

The plot in Fig. 5.3 shows a comparison of mean static pressure coefficients ($c_p = \frac{p - p_2}{p_{t1} - p_2}$, where p_{t1} and p_2 are total pressure at the inlet and back pressure at the outlet respectively), as obtained by the present simulation against experimental results (Stadtmuller 2002*a*). The data from Wissink (2003) for the clean inlet is also plotted in the figure, since they have also reported the existence of leading edge separation bubbles. On the pressure side, the results match very well for all the grids; however on the suction side, where the flow is rather complex, the results are not in such good agreement except those from the finest grid (C).

The results on the pressure distribution are of great interest because the downstream flow on the suction side is extremely sensitive to the pressure distribution at the LE (see section 5.3). It has been observed to our surprise that for the grid C, where the c_p match is best, the LE separation bubble disappears, but the TE separation bubble gets longer as well as thicker (as the flow remains laminar till it hits the bubble). This long separation bubble is normally identified with higher losses in a turbine blade and hence should be avoided in blade design considerations.

It is interesting that such a fundamental bulk parameter as pressure distribution can be so sensitive to resolution. To understand the reason for this difference, c_p is plotted against the

Table 5.2 Distance along the blade varying with axial chord

Pressure Side		**Suction Side**	
x/l_{ax}	s	x/l_{ax}	s
0.1	0.102	0.1	0.162
0.2	0.207	0.2	0.284
0.3	0.308	0.3	0.39
0.4	0.408	0.4	0.49
0.5	0.514	0.5	0.594
0.6	0.628	0.6	0.709
0.7	0.76	0.7	0.85
0.8	0.918	0.8	1.032
0.9	1.15	0.9	1.254
1.0	1.352	1.0	1.56

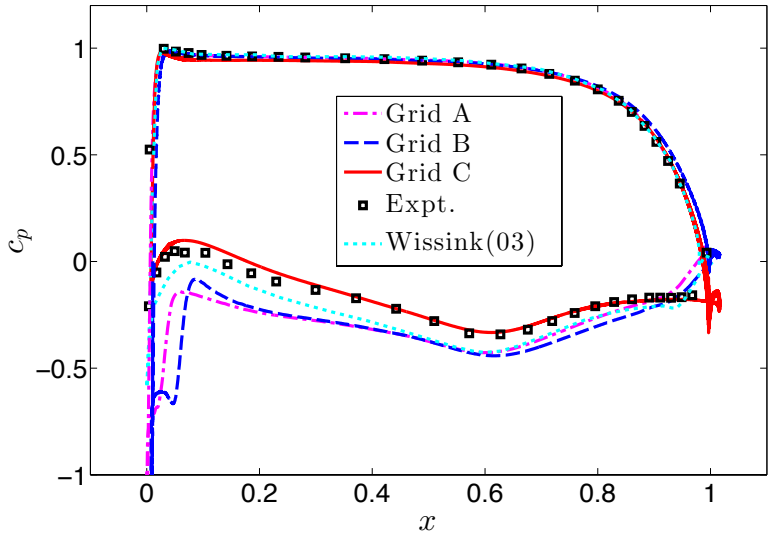

Fig. 5.3 Co-efficient of pressure on T106A blade

streamwise co-ordinates along the surface of the blade (see Fig. 5.4). The experimental data as well as data from Wissink (2003) are only available along the axial chord (x). They are here interpolated on the streamwise co-ordinates along the surface of the blade and plotted against our results. The axial co-ordinates (x) and the streamwise co-ordinates along the blade (s) are interchangeably used throughout this thesis depending on the context. Table 5.2 is hence provided where the relation between x and s is listed at 10 different locations to help the reader. $s = 0$ starts on the both sides (suction and pressure) at the leading edge co-ordinate given in the geometry file of Stadtmuller (2002*a*). It is to be noted that based on this definition, the LE stagnation point at incidence $\beta_1 = 45.5^\circ$ lies on the pressure side ($s \simeq 0.03$).

In Fig. 5.4, the small plateaus that are present near the LE ($s \simeq 0.05$) for grids A and B mark the presence of the separation bubble. The absence of this plateau in case of grid C is internally consistent with the absence of the bubble. Similarly the long flat c_p near the TE for experiment as well as grid C mark a longer separation that is not reattached on the blade, whereas just small kinks in the c_p for other studies (at $s \simeq 1.4$) suggest short reattaching bubbles.

It can be quickly noticed that the pressure near the LE on the suction side for all the simulations in which an LE separation bubble is observed, is consistently below the experimental value. This difference of computed c_p value with the experimental value is plotted in Fig. 5.5. Only in the finest grid C, c_p is slightly higher than experimental value near the LE.

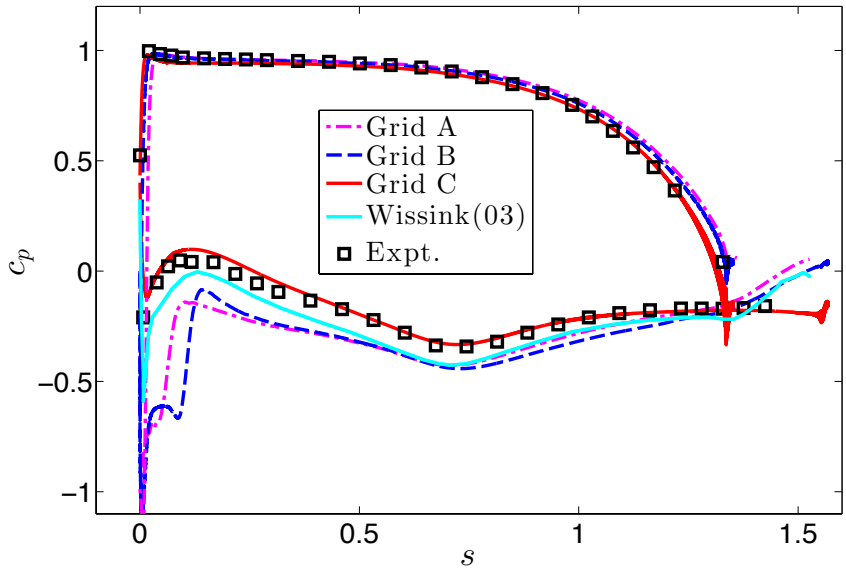

Fig. 5.4 Co-efficient of pressure on T106A blade along the blade

Our RANS/LES results presented in Chapter 6, where no LE separation bubble is noticed, confirm these observations.

The flow at this incidence ($\beta_1 = 45.5°$) has a stagnation point on the pressure side, and then turns around the nose of the blade trying to overcome the adverse pressure gradient. Flow reversal usually occurs in the this region of the boundary layer if this gradient is sufficiently large. From Fig. 5.4, it can be argued that for the separated flow cases the relatively low pressure (compared to the attached case) in the vicinity of the stagnation point, combined with the high curvature, imposes a slightly higher adverse gradient which is enough to cause flow reversal. Once the flow is reversed, the curvature again plays an important role in hindering the flow from reattaching. Several instabilities and structures in this region are seen in the instantaneous flow to be described in section 5.3. The LE separation changes the entire course of the flow and a completely different picture (compared to attached flow) emerges due to separation-induced transition. The attached flow on the other hand remains laminar till the aft region of the blade, where it separates. Both flows are internally consistent and fluid-dynamically interesting, and may represent different scenarios in which a turbine blade can operate depending on a variety of factors, including free-stream turbulence, wake impingement, surface roughness, angle of incidence and Reynolds number.

In the context of grid resolutions, it is difficult to provide precise explanation for this discrepancy in the pressure predictions, given that all three grids seem to be well-resolved in the boundary layer for standard computations. The complexity of the flow combined with

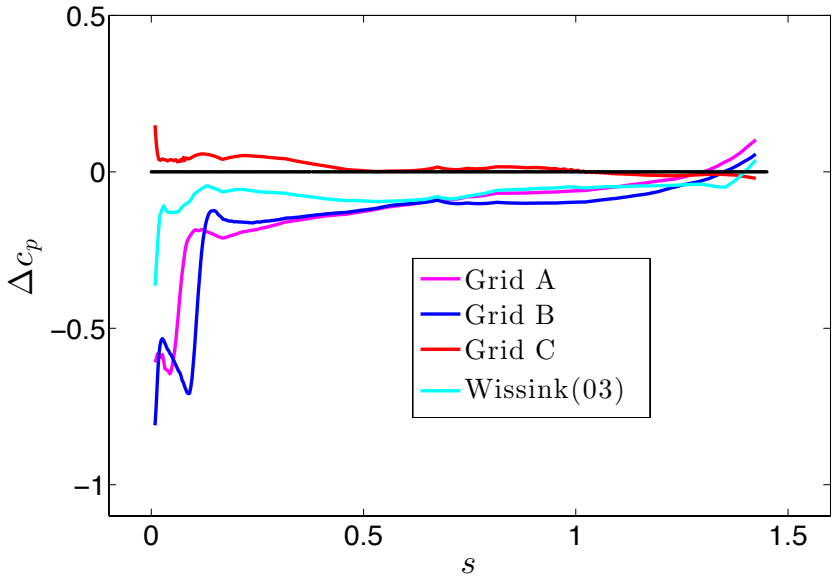

Fig. 5.5 Difference in c_p between DNS and experimental data on the suction side.

factors such as a highly curved high-lift blade, low transitional *Re*, and a high incidence, pose a big challenge to the numerical schemes in resolving the flow satisfactorily. Further, this flow is sensitive to a variety of disturbances and even a miniscule amount of noise (either physical or numerical) may trigger instability. It is to be again emphasized here that at the design incidence $\beta_1 = 37.7^\circ$, no major discrepancies were noted in studies with different resolution; as mentioned above, there is no separation bubble at the LE but there is always one at the TE. Nevertheless, we may list here the numerics factors that are possible reasons for the discrepancy at high incidence:

- Curvature of the blade
- Wall-normal resolution
- Numerical noise

We now discuss each of the factors listed above in the context of the present simulations.

It is suspected that at an incidence as high as 45.5° the high curvature of the blade near the LE is playing a major role in deciding the fate of the downstream flow. It should also be pointed out here that in the experimental report (Stadtmuller (2002*a*), the entire geometry of the blade is defined by 199 points, with only 3 points near the LE where separation may occur. Since the curvature in this region is very high, it is possible that streamwise resolution

may affect the incoming flow. The effect of curvature is discussed in detail in section 5.4, where it is shown how high curvature affects the mean flow.

The wall-normal resolution is important because the differences in computed c_p may be due to the interplay between the boundary layer and the external flow. Grid C has very high wall-normal resolution ($\Delta\eta^+ <= 0.1$) for most of the blade (as shown in Fig. 4.5), which is much higher than resolution in any other study. The streamwise and wall-normal resolutions for different grids used in our studies is listed in Table 4.3.

Numerical noise in the numerical methods adopted can be one of the reasons for the discrepancies, but it is difficult to estimate exactly for 3D Navier-Stokes computations. This aspect is also related to the choice of the computational grid. The presence of upstream wakes/FSTI only makes this issue even more complicated. Since we have not performed simulations with wakes, it is difficult to comment here on its effects on the flow.

Before closing the topic, it is worthwhile to present the work of Sundaresan *et al.* (1998) where the effect of grid resolution is convincingly presented on the relatively far simpler case of 2D lid-driven cavity flow at high Reynolds number. Their work shows the need for an extremely refined boundary layer grid to get accurate results even in the core region of the cavity. In this context, a theorem due to Shishkin (1997) is worth mentioning. He has proved mathematically that the solutions of elliptic and parabolic equations in the boundary layer do not show uniform numerical convergence (which is the property that the difference between the exact and numerical solutions goes to zero as the mesh size tends to zero). The results of Sundaresan *et al.* (1998) have been seen as a demonstration of the validity of the Shishkin theorem (Fedoseyev 2001).

Shishkin (1997) has suggested that to avoid the grid-dependence of solutions, a special kind of mesh (known as the Shishkin mesh) should be used in the boundary layer. But construction of a Shishkin mesh requires knowledge of boundary layer thickness, which is often not available in advance. The classical computational approaches require extremely large numbers of grid points to produce satisfactory computed solutions.

Some relevant questions that arise from the present study are: (1) How smooth are real turbine blades? (2) What is the disturbance level of (acoustic) noise inside a turbine and how can it be characterized and simulated in an essentially fruitful way on the computer? Unfortunately there is not much experimental data to answer these questions.

In the absence of more experimental data or convincing computational data to compare with the present DNS results and hence to address the discrepancy, we examine how best the solutions can be assessed to study some of the interesting fluid-dynamical aspects. Internal consistency checks for the simulation results are made wherever possible. Four fluid-dynamical aspects: curvature effects, separation bubbles, transition and relaminarization

are discussed separately in the next four sections. It is hoped that these analyses will offer insights into the complex flow that may involve one or more of the phenomena described above. The parameters of engineering interest in the flow are discussed in Chapter 6.

5.3 Separation Bubbles

Figure 5.6 gives visual representations of the separation bubbles at LE and TE through streamline plots for the mean velocity field at the leading and trailing edges of suction side respectively, as obtained from simulations using Grids A, B and C.

The stagnation point can be seen on the pressure side where the incoming flow at an incidence of 45.5° hits the blade. The flow then has to turn around the leading edge while trying to overcome the adverse pressure gradient. The separation bubble that thus develops is noticeable in grid A and B plots. This bubble is missing in grid C for reasons explained in earlier section.

Another noticeable aspect is the difference in TE separation in the aft region of the suction side of the blade for grid C. This is not surprising as the flow upstream of the the separation remains laminar in case of grid C whereas for other grids the flow has undergone a separation-induced transition at the LE. This large separation for grid C is further confirmed by the long plateau in the c_p plot of the experiment (Fig. 5.3).

The separation regions can also be identified from the boundary layer velocity profiles plotted in the neighbourhood as shown in Fig. 5.7. The negative velocity near the wall indicates reversal of the flow in the separation regions. In the profile near the LE, the mean velocity falls steeply just outside the boundary layer. This is due to effect of strong convex surface curvature, which is described in detail in section 5.4.

The mean skin friction coefficient (wall shear stress normalized by the far free-stream quantities, $c_f = \frac{\tau_w}{0.5\rho_\infty U_\infty^2}$) from the simulations is plotted in Figure 5.8. Once again separation is clearly marked by the negative values of c_f. The pressure side shows no separation and the results with different grid resolutions show no discrepancy among one another. The suction side, on the other hand has large discrepancies among different grid results as stated above. The results from Wissink (2003) are also plotted, where the LE separation can be seen.

The characteristics of the bubbles obtained with different grid simulations are listed in Table 5.3. Subscripts 0 and 1 indicate the positions just upstream and downstream of the bubbles at both LE and TE. Once again there is a good match between grid A and grid B, but they stand out when compared with grid C.

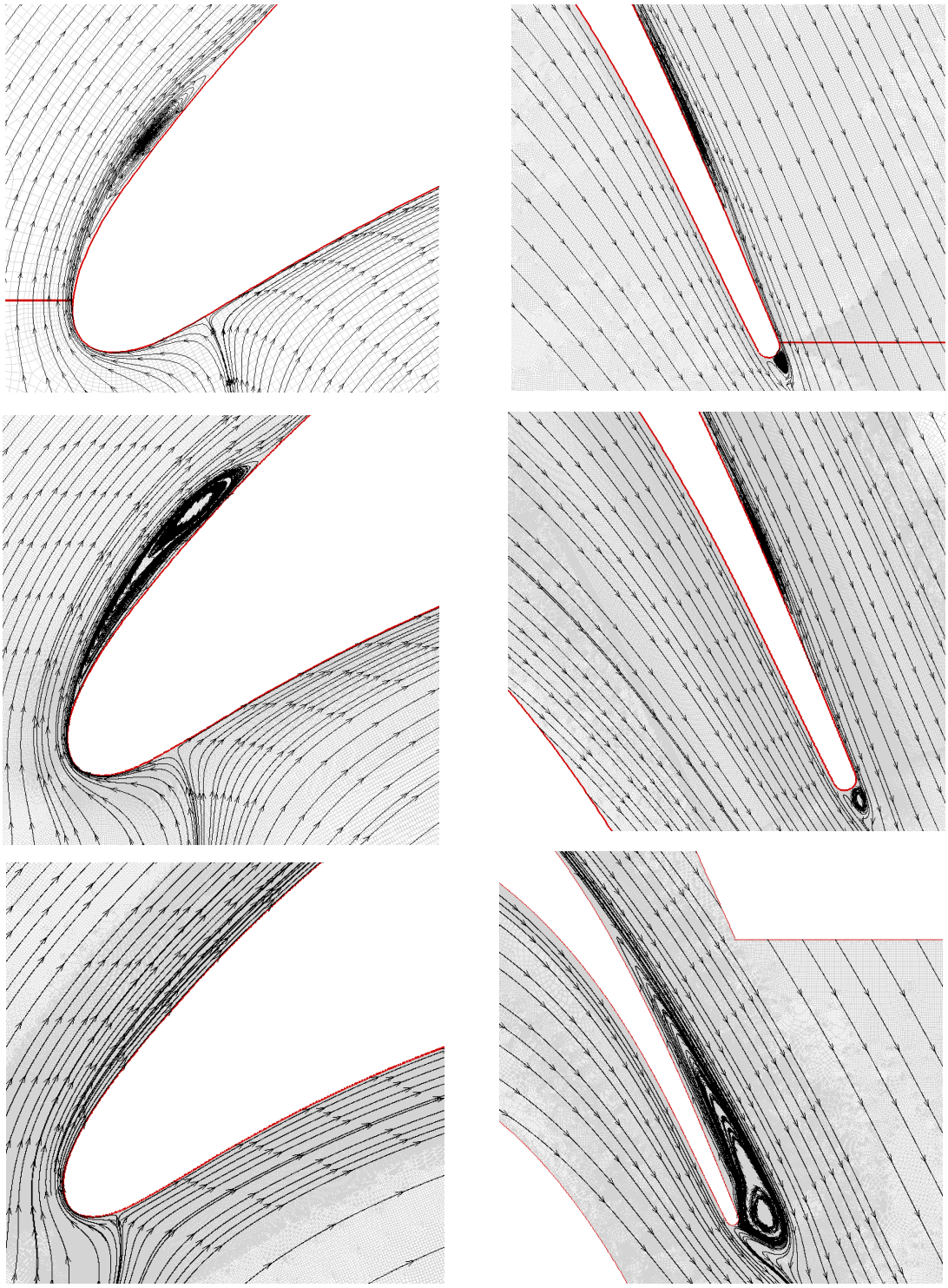

Fig. 5.6 Streamlines of mean flow for $\beta_1 = 45.5°$. All simulations were performed without any free-stream turbulence. Top: Grid A, Middle: Grid B, Bottom: Grid C. Left: LE, Right: TE

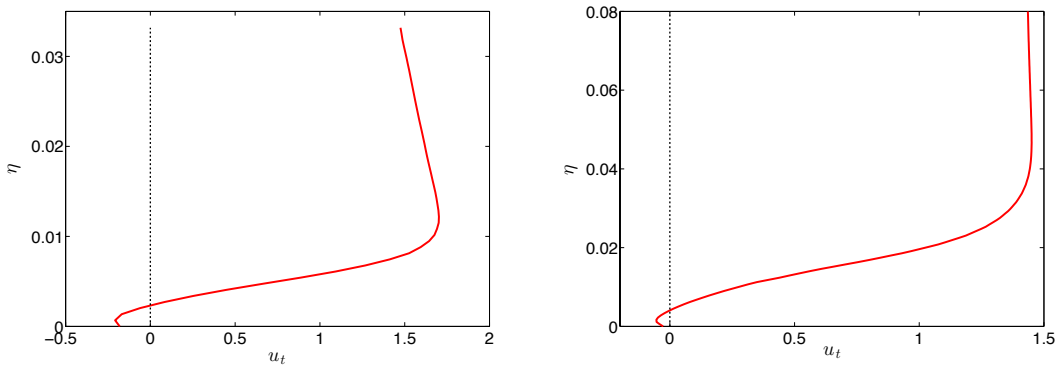

Fig. 5.7 Mean velocity profile in the boundary layer near separation bubbles (at $x = 0.025$ (left) and at $x = 0.92$ (right)). (Grid A)

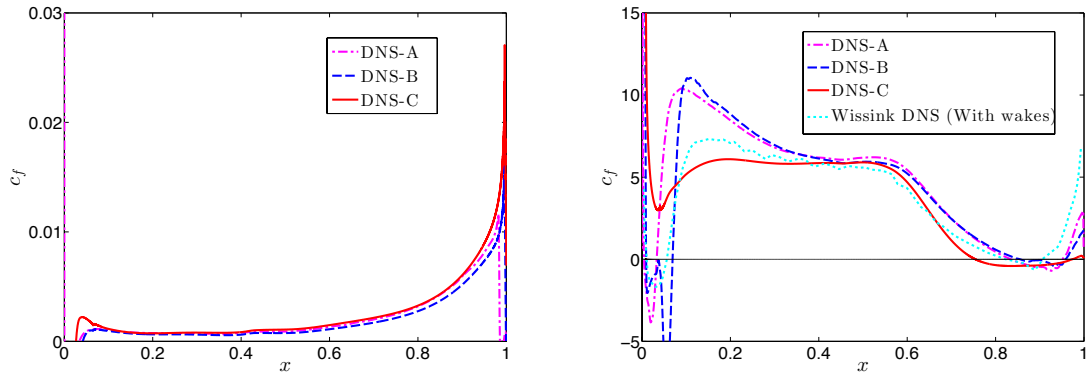

Fig. 5.8 Mean skin-friction on the blade. Left: Pressure side, Right: Suction side. Separation region is marked by negative skin-friction.

The table also includes the pressure gradient parameter $P = \dfrac{h^2}{\nu}\dfrac{\Delta u}{\Delta x}$ suggested by Diwan *et al.* (2006) to categorize the bubbles as of the 'long' or 'short' type. Here h represents the maximum thickness of the bubble (also included in Table 5.3) and $\dfrac{\Delta u}{\Delta x}$ is the a measure of velocity slope across the bubble. According to the survey done by Diwan *et al.* (2006) on many separating flows, bubbles fall in the category of short if $P > -28$, else long. Table 5.3 clearly indicates that the LE bubbles are short. However TE bubbles are short only if the upstream boundary layer is transitional (grid A and B). This is consistent with the observations on turbine blade separated flows, where bubbles are short in transitional flow separation. For grid C, where the flow stays laminar, the bubble comes under long category.

The instantaneous pictures of theses bubbles are presented in Fig. 5.9. When compared with the mean (Fig. 5.10), these instantaneous bubbles look very rich in structure as we notice a train of separation rolls or (sometimes) bubbles. The rolls are differentiated from the

Table 5.3 Characteristics of separation bubbles

	Leading Edge			**Trailing Edge**		
	Grid A	**Grid B**	**Grid C**	**Grid A**	**Grid B**	**Grid C**
x_0	0.006	0.008	-	0.823	0.845	0.755
x_1	0.046	0.071	-	0.964	0.967	1.1
U_0	1.95	1.9	-	1.57	1.55	1.89
U_1	1.61	1.56	-	.143	1.42	-
h	0.006	0.007	-	0.006	0.002	0.07
P	-8.2	-10.6	-	-1	-0.09	-126
Type	short	short	-	short	short	long

bubbles by the clear presence of separation and reattachment points in the latter. Separation rolls are structures within a bubble where streamlines are not fully reattached, but a tendency for reattachment gives rise to instability. Bubbles on the other hand are marked by separate reattachment points.

Many investigators including Wissink (2003), and Sarkar (2007) have reported multiple separation rolls observed in their simulations in the context of the effect of incoming wakes. In their DNS, Michelassi *et al.* (2002) have observed two instantaneous separation bubbles near the TE . In our simulations, we notice as many as three instantaneous bubbles near the TE, as shown in Fig. 5.11.

These instantaneous bubbles break and merge with time, and have a three-dimensional structure. The three-dimensionality of the bubbles can be noticed from the spanwise-vorticity ω_z contours (Fig. 5.18 given in section 5.5), in which the separation is marked by the positive vorticity.

Figure 5.12 shows the instantaneous pictures of the LE separation bubble as a function of time. The location as well as extent of these separation bubbles change with time. The bubbles break up and merge in time to form a single average bubble.

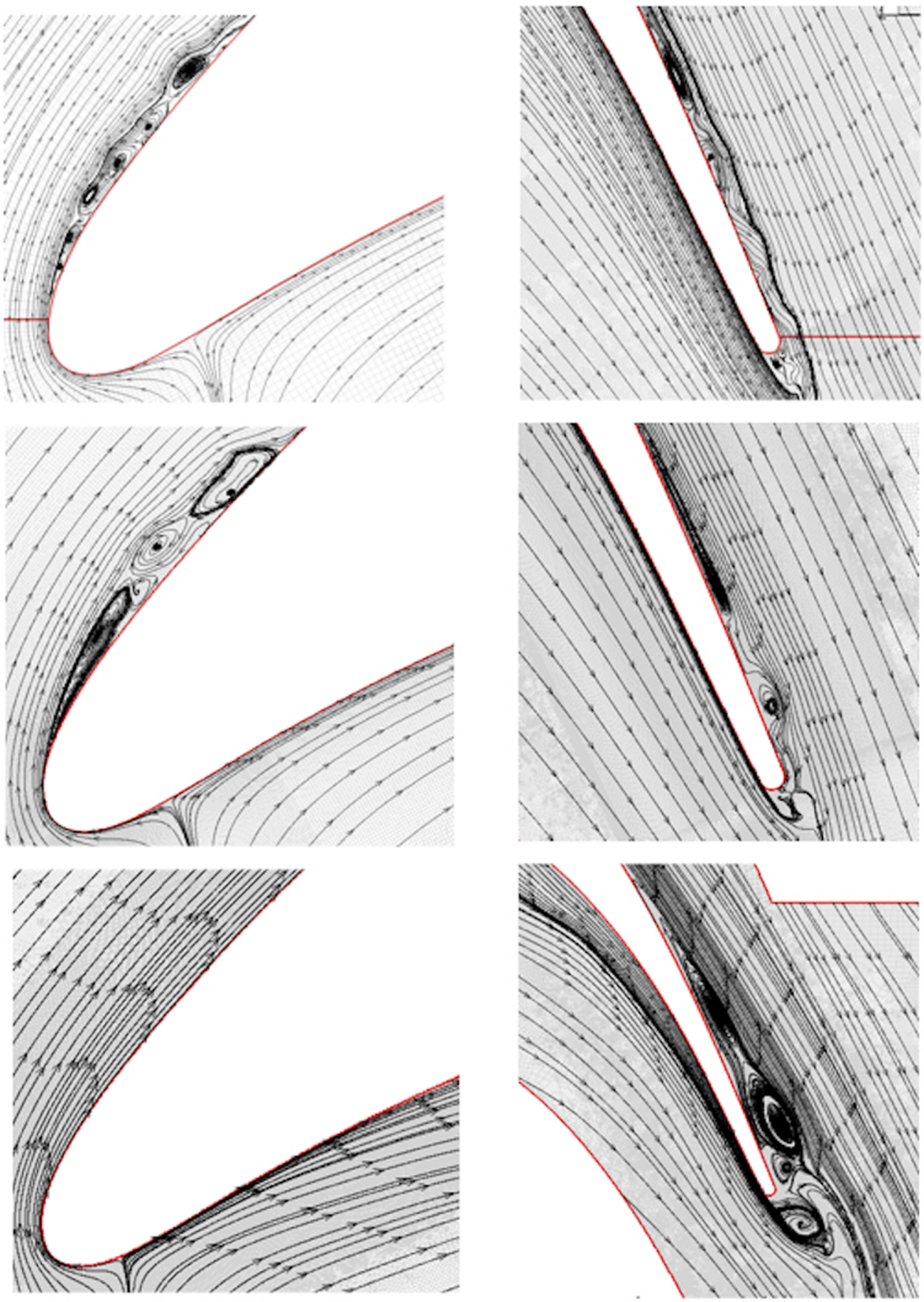

Fig. 5.9 Streamlines of instantaneous flow for $\beta_1 = 45.5°$. Top: Grid A, Middle: Grid B, Bottom: Grid C. Left: LE, Right: TE

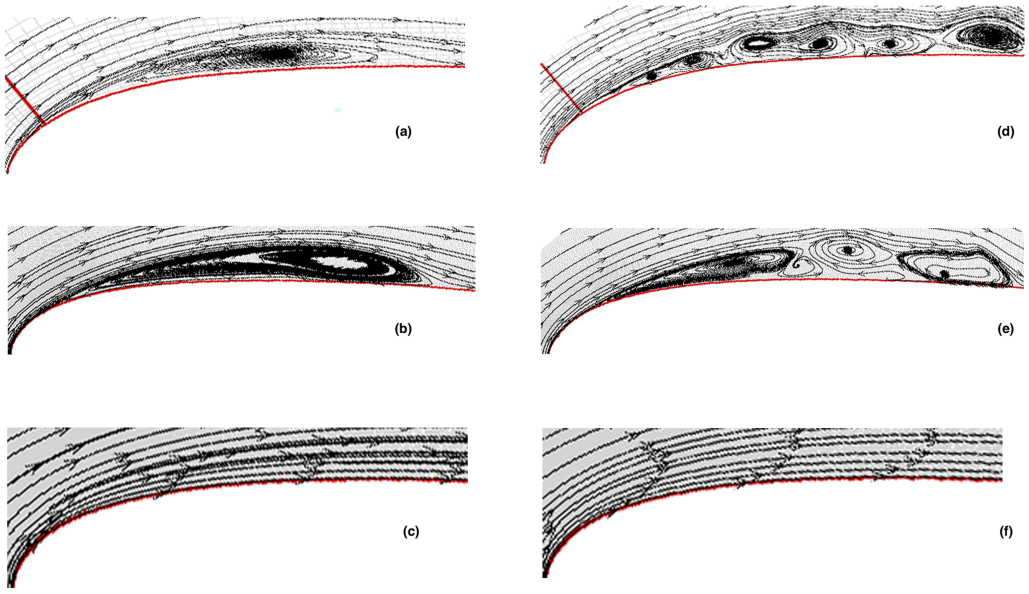

Fig. 5.10 Comparison of structures of mean and instantaneous bubbles at the LE. Top: Grid A, Middle: Grid B, Bottom: Grid C. Left: Mean, Right: Instantaneous

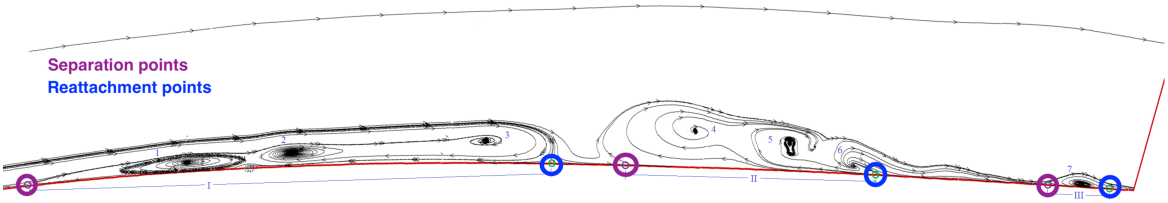

Fig. 5.11 Multiple separation bubbles at the trailing edge (Grid A)

This instantaneous instability within mean separation bubbles can have implications on the engineering parameters such as skin-friction and heat-transfer, and hence on blade design. These aspects are covered in Chapter 6.

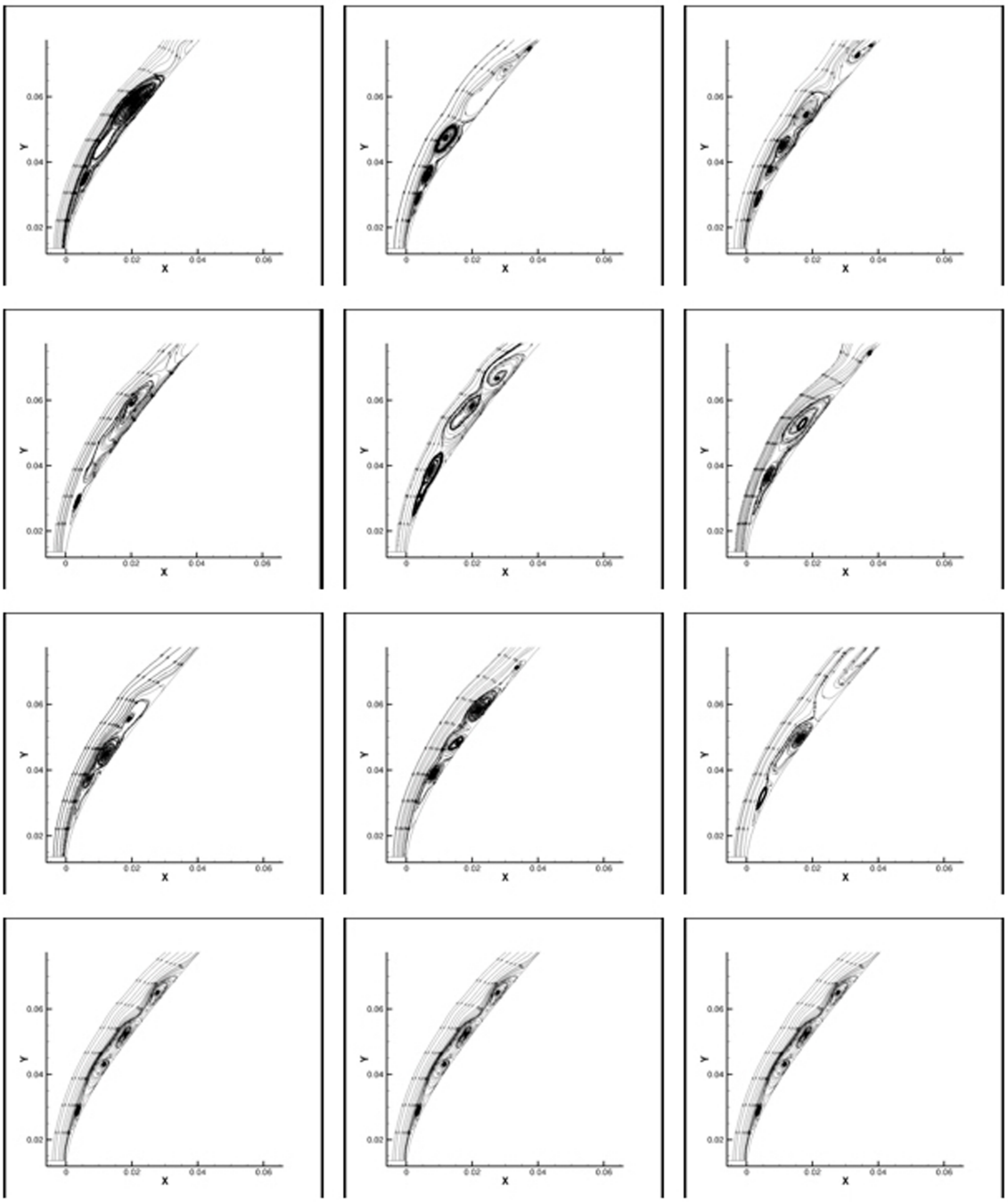

Fig. 5.12 Changing structures inside LE separation bubble between $t = 7$ and $t = 8$ (Grid A)

5.4 Curvature Effects

This section describes the the effect of curvature on the boundary layer mean flow, and also compares the DNS results against high-order boundary layer theory, which retains terms containing higher order curvature effects in the boundary layer equations.

Streamline curvature and rotation play an important role in deciding the nature of flow on turbine blades. On the convex side of the blade, the flow gets accelerated due to centrifugal force and thus the turbulence in the boundary layer gets weakened. On the other hand, turbulence in the boundary layer gets enhanced on the concave side due to curvature. The level of turbulence makes a significant impact on the due course of the flow, specially in the transitional region.

Figure 5.13 shows boundary layer velocity profiles very near the leading edge as obtained from DNS with the highest resolved grid (C). Similar profiles are also obtained in simulation with other grids. The 'curved' boundary layer profiles are due to very high surface curvature. As we go away from the leading edge, the curvature effect becomes weaker.

The red straight lines on the plots are the fit to the 2^{nd} order boundary layer theory (to be discussed shortly) where it is assumed that the velocity in the outer layer varies linearly with curvature and normal distance from the surface, i.e.

$$U = U_{0w} - \kappa\, y$$

Here $\kappa = \kappa(s)$ is the curvature of the blade at location s, and U_{0w} is the velocity at the wall according to potential flow in the inviscid outer layer, and is close to being a velocity at the edge of the boundary layer.

The curvature non-dimensionalized with blade-axial length (l_{ax}) obtained using 2^{nd} order boundary layer theory is plotted along the blade chord in Fig. 5.14 (a). Very near the LE ($0 <= s <= 0.03$), curvature is an order-of-magnitude higher than further downstream. This curvature is also compared with local geometric curvature of the surface κ_{geo}. This is calculated by the formula,

$$\kappa_{geo} = \frac{x'y'' - y'x''}{(x'^2 + y'^2)^{3/2}}$$

where $x' = \mathrm{d}x/\mathrm{d}s$ etc.

The gradients above are calculated by fitting arcs over every 3 points using the least-square method.

The otherwise smooth curve of geometric curvature has two kinks at $s = 0.008$ and $s = 0.024$. This came as a surprise because the smooth blade curve is made by importing the co-ordinates of Stadtmuller (2002*a*) using splines. This curvature is then plotted against

the axial chord along with the blade curve (Fig. 5.14 (b)). The kinks are visible where the curve changes sign (from concave to convex) and also at a point where the leading edge separation is suspected (in Grid A, B, B1 simulations).

5.4.1 Application of Higher-order Theory

In the literature, there are very few computational studies (especially RANS and LES) on turbine blades where the effects of curvature and rotation are accounted for. Recently Rinaldi *et al.* (2014) have implemented curvature corrections in $\gamma - Re_\theta$ transition model due to (Langtry & Menter 2009) to simulate flow past turbine blades. With this correction, they have reported better agreement with experiments in the prediction of transition onset, and hence improvement in the prediction of heat-transfer and pressure co-efficients on a VKI turbine blade.

One of the purposes of DNS simulations is to help improve the existing models by providing new databases and insights. In this spirit, the present DNS results are compared against the higher-order theory of Narasimha & Ojha (1967).

The classical boundary layer theory of Prandtl does not take account of changes due to curvature of the surface on the boundary layer. Based on the higher order approximations in boundary layer theory proposed by Van Dyke (1962), Narasimha & Ojha (1967) have used the full Navier-Stokes equations in orthogonal curvilinear co-ordinates and expanded in Prandtl (inner) and Euler (outer) limits. The inner expansion of the variables is:

$$\begin{aligned} u =& u_0 + \varepsilon u_1 + ...(\varepsilon = \frac{1}{\sqrt{Re}}) \\ v =& \varepsilon v_0 + \varepsilon^2 v_1 + ... \\ p =& p_0 + \varepsilon p_1 + ... \end{aligned}$$

Retaining the zeroth-order quantities gives the well-known Prandtl boundary layer equations, as:

$$\frac{\partial u_0}{\partial x} + \frac{\partial v_0}{\partial y} = 0 \tag{5.1a}$$

$$\frac{\partial p_0}{\partial y} = 0 \tag{5.1b}$$

$$u_0 \frac{\partial u_0}{\partial x} + v_0 \frac{\partial u_0}{\partial y} = -\frac{dp_0}{dx} + \frac{\partial^2 u_0}{\partial y^2} \tag{5.1c}$$

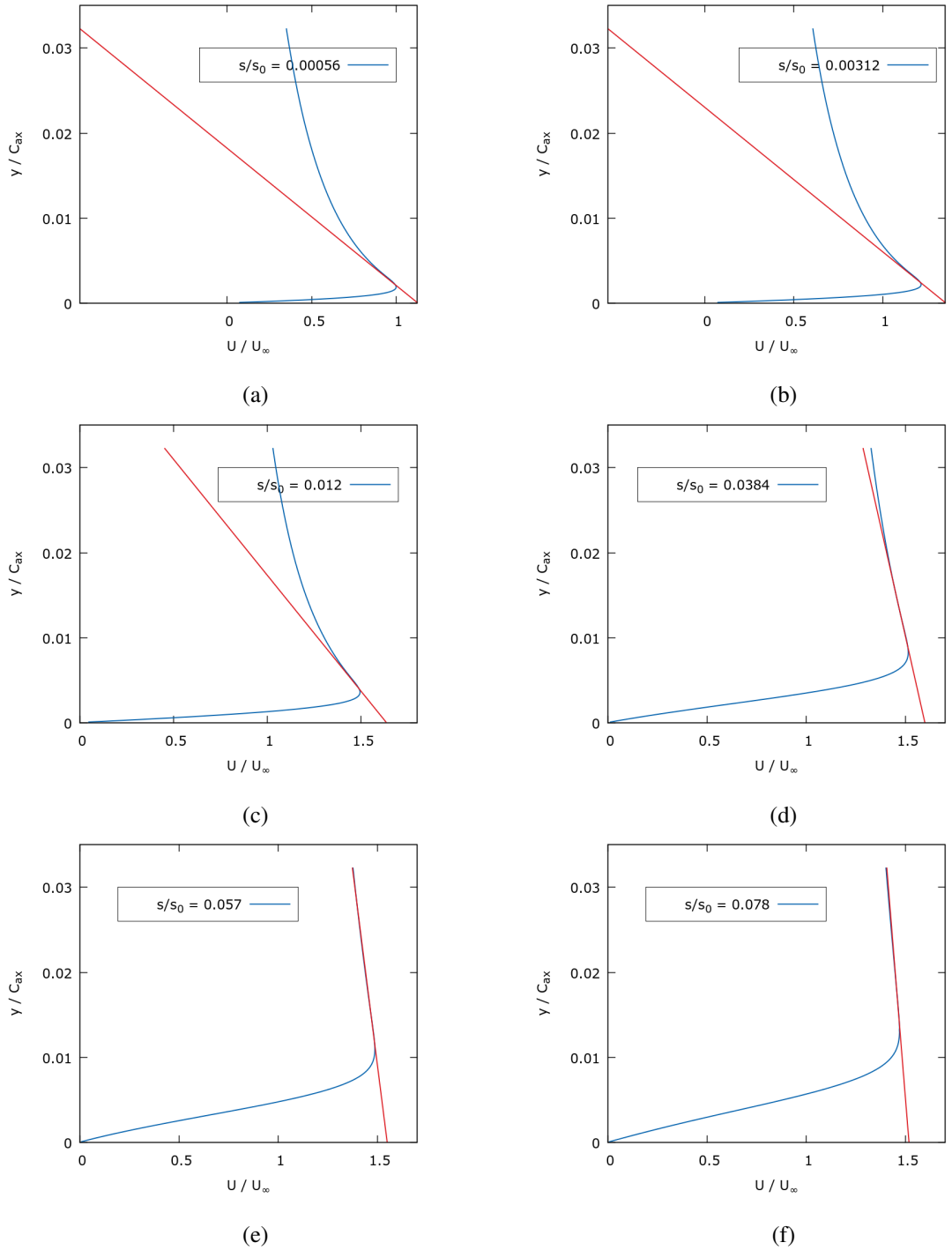

(a) (b) (c) (d) (e) (f)

Fig. 5.13 Velocity profiles near the leading edge of the suction side (Grid C). Curvature is clearly visible in these profiles. Red line shows the fit using the first order theory. For 1^{st} order boundary layer theory to be applicable, velocity at the edge of the boundary layer (U_{0s}) should linearly approach free-stream velocity using the relation $U = U_{0s} - \kappa y$

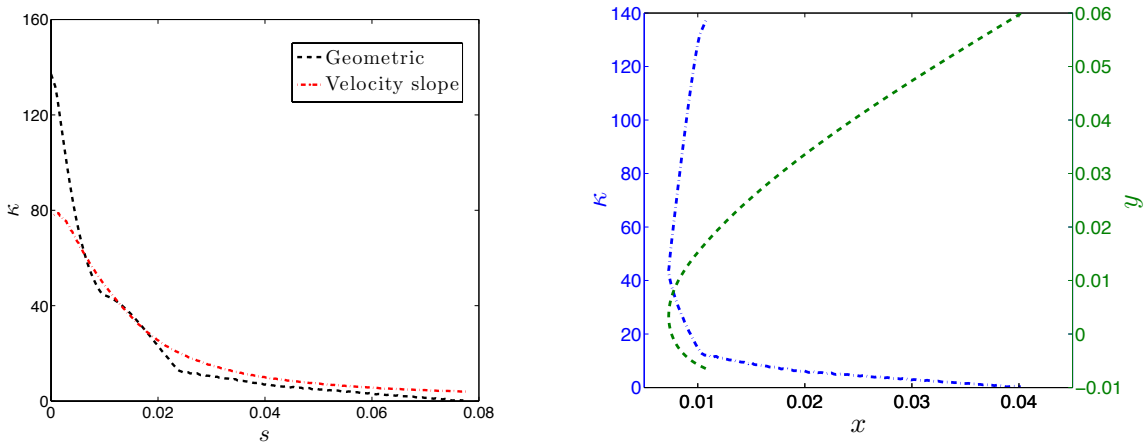

(a) (b)

Fig. 5.14 Curvature along the blade surface (left) and along the axial chord (right) near the leading edge of the suction side

Retaining the next order terms gives the 1^{st} order equations that includes curvature as well as displacement effects

$$\frac{\partial u_1}{\partial x}+\frac{\partial v_1}{\partial y}=-\kappa\,\frac{\partial(u_0 y)}{\partial y} \tag{5.2a}$$

$$\frac{\partial p_1}{\partial y}=\kappa\,u_0^2 \tag{5.2b}$$

$$u_0\frac{\partial u_1}{\partial x}+v_0\frac{\partial u_1}{\partial y}+u_1\frac{\partial u_0}{\partial x}+v_1\frac{\partial u_0}{\partial y}=-\frac{\partial p_1}{\partial x}+\frac{\partial^2 u_1}{\partial y^2}+\kappa\left\{y\Big(u_0\frac{\partial u_0}{\partial x}+\frac{\partial p_0}{\partial x}\Big)+\frac{\partial u_0}{\partial y}-u_0 v_0\right\} \tag{5.2c}$$

where κ is the local curvature.

This has to be accompanied with appropriate boundary conditions in the asymptotic limits for both inner and outer equations. Also, since the 1^{st} order equation is linear, the displacement effect can be separated from the curvature effect. For curvature effects, the above equation finally leads to the following equations,

$$\frac{\partial u_1}{\partial x}+\frac{\partial}{\partial y}(v_1+\kappa\,y\,u_0)=0 \tag{5.3a}$$

$$u_0\frac{\partial u_1}{\partial x}+v_0\frac{\partial u_1}{\partial y}+u_1\frac{\partial u_0}{\partial x}+v_1\frac{\partial u_0}{\partial y}=-\frac{\partial}{\partial x}\left\{\kappa\int_0^y u_0^2\,dy+\kappa\int_0^\infty(U_{0s}^2-u_0^2)\,dy\right\}+\frac{\partial^2 u_1}{\partial y^2}+\kappa\left\{y\,\Big(u_0\frac{\partial u_0}{\partial x}+\frac{\partial p_0}{\partial x}\Big)+\frac{\partial u_0}{\partial y}-u_0 v_0\right\} \tag{5.3b}$$

with the boundary conditions

$$u_1 = v_1 = 0, \qquad \text{at} \qquad y = 0, \tag{5.4a}$$

$$\text{and} \qquad u_1 = -\kappa\, y\, U_{0s}, \qquad \text{as} \qquad y \to \infty. \tag{5.4b}$$

where $U_{0s} = U_0(X,0)$ is the surface speed from the outer solution as illustrated in 5.13.

Narasimha & Ojha (1967) have also given a Falkner-Skan like similarity solution for the 1^{st} order equations for certain conditions. If the velocity varies as a power law with distance,

$$U_{0s} = C\, s^m$$

where C is an arbitrary constant.

For the above flow, the usual Falkner-Skan solution for the zeroth order equation is

$$f_0''' + f_0 f_0'' = \beta(f_0'^2 - 1) \tag{5.5}$$

where $m \equiv \beta/(2-\beta)$ and the primes denote differentiation with respect to the transformed co-ordinate η, and f_0 is function of only η.

Similarly it is shown that using appropriate transformations, the similarity solution of 1^{st} order equations can be obtained provided the curvature varies as

$$\kappa = \kappa_s \left[\frac{C(m+1)}{2}\right]^{\frac{1}{2}} s^{\frac{1}{2}(m-1)} \tag{5.6}$$

$$\tag{5.7}$$

where κ_s is a constant.

The equations 5.3 reduce to

$$f_1''' + f_0 f_1'' - 2\,\beta f_0' f_1' + f_0'' f_1 = \kappa_s \Bigg[f_0''(\eta f_0 - 1) - f_0 f_0'' - \beta \left\{ \eta(f_0'^2 - 1) - \frac{2}{1+\beta}(f_0'' + f_0 f_0' + \beta\eta + A) \right\} \Bigg] \tag{5.8}$$

where

$$A \equiv \lim_{\eta \to \infty} (\eta - f_0) \tag{5.9}$$

The boundary conditions in similarity variables become

$$f_1(0) = 0 = f_1^{'}(0) \tag{5.10a}$$

$$f_1^{'}(\eta) \approx -\kappa\,\eta \qquad \text{as} \qquad \eta \to \infty \tag{5.10b}$$

The solution (f_0) of the non-linear Falkner-Skan equation is needed to solve the 1^{st} order equation (linear) 5.8 numerically. Narasimha & Ojha (1967) have used already available Falkner-Skan results to interpolate and then solve 1^{st} order equations using Runge-Kutta method.

In the present work, both equations were solved simultaneously on the same grid. A shooting method was used to satisfy the boundary conditions at ∞. The effect of curvature can be seen in Fig. 5.15 where the velocity profiles with and without curvature effects are compared for $\kappa_s = 1.7$. Higher-order theory shows a significant departure from the Prandtl boundary layer theory in this case. The DNS results at the corresponding location ($x = 0.04$ on the suction side) are also compared with the higher-order theory. The higher-order theory shows a very good match with the DNS results and hence has a potential to be used in RANS/LES calculations to account for curvature effects .

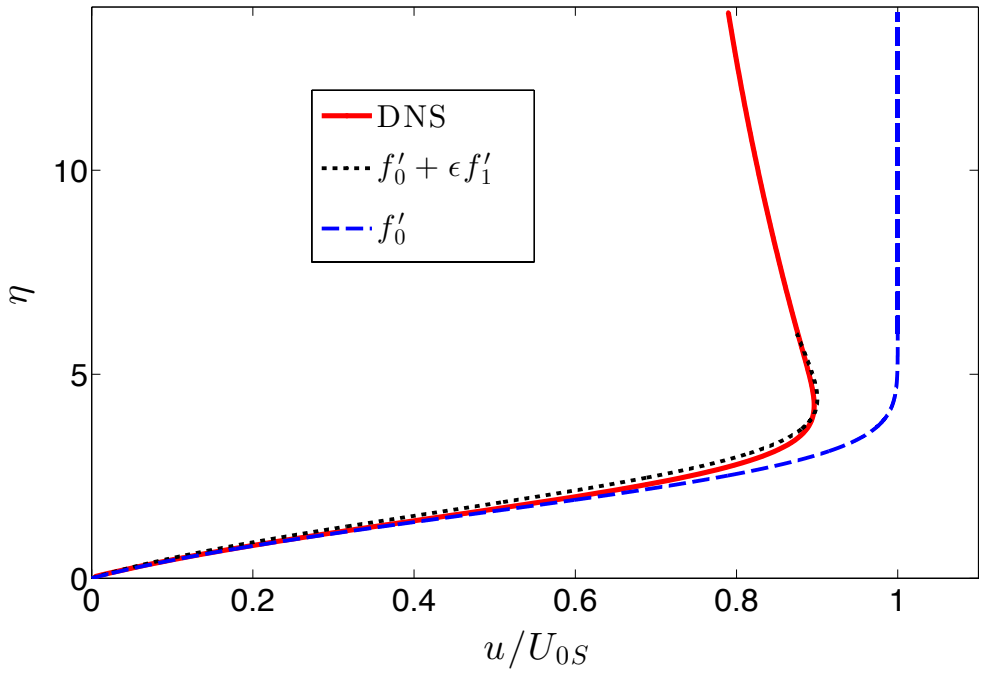

Fig. 5.15 Curvature effects: Prandtl vs Higher Order. $\kappa_s = 1.7$. DNS results are also plotted.

5.5 The Transition Zone

This discussion here is limited to the flow scenario on a turbine blade where a separation bubble at the leading edge (as we notice in the simulations with grids A, B and B1) induces transition and alters the flow downstream. In the results obtained with the finest grid C, the flow remains laminar on the suction side till the long separation zone in the aft region of the blade, where separated-flow transition occurs. Since the dynamics of this flow is relatively simple (compared to flows where LE transition occurs), it is not discussed here.

Further, since all the simulations that predict LE separation present very similar pictures (see section 5.3), the analysis presented below is performed with the results obtained with coarsest grid A .

Figure 5.16 shows contours of the total velocity in the boundary layer at $t = 7$. The levels at which the contours in Fig. 5.16 are plotted, were such that in the middle of the blade, where there is no separation $\Delta\eta^+ \approx 10$, which corresponds to the 5^{th} grid point above the surface of the blade. It is seen that there is a rapid rise from the low values just downstream of the bubble at $x = 0.046$ to higher values in the range 0.03 to 0.2 (also see zoomed view in Fig. 5.17). Furthermore, over $0.05 < x < 0.2$ the velocity field is laterally inhomogeneous, and shows streamwise patches of higher velocity, losing much of that inhomogeneity beyond $x = 0.2$. This suggests an intermittent transition zone. Different regions are marked in Fig. 5.16 and also compared with the skin-friction co-efficient. The sudden increase of skin-friction in the instanteous flow ($x = 0.1$ and $x = 0.95$) is related to the onset of transition.

To probe the issue further, Figure 5.18 presents contours (at $t = 7$) of the instantaneous spanwise vorticity ω_z at the wall. It should be noted that this is dominated by $\partial u/\partial y$ at the wall, and is therefore a good indicator of the wall stress τ_w (note that when ω_z is positive, τ_w is negative). It is seen that, going downstream, ω_z is at first positive ($\tau_w < 0$) over $0.006 < x < 0.046$, indicating that the separation bubble covers this range. Immediately downstream, however, ω_z goes negative ($\tau_w > 0$), and indeed rises rapidly, indicating the occurrence of transition onset in the neighbourhood of the last reattachment point in the separation bubble regime.

The transition zone extends roughly from $x \simeq 0.05$ to about $x \simeq 0.2$ and the onset of transition seems to be within the separation bubble.

Figure 5.19 shows the streamwise variation of $\bar{\tau}_w$, the mean wall stress. Also shown are separate predictions for purely laminar ($\bar{\tau}_{w_L}$) and purely turbulent ($\bar{\tau}_{w_T}$) boundary layers, both subjected to the same pressure gradient. For the laminar boundary layer the initial condition is taken as the velocity profile at $x = 0.05$, as given by the present DNS solution. The turbulent boundary layer is taken to originate at $x = x_t = 0.04$, as in the linear combination model for the transition zone (Dhawan & Narasimha 1958). The estimate of x_t is based on computed

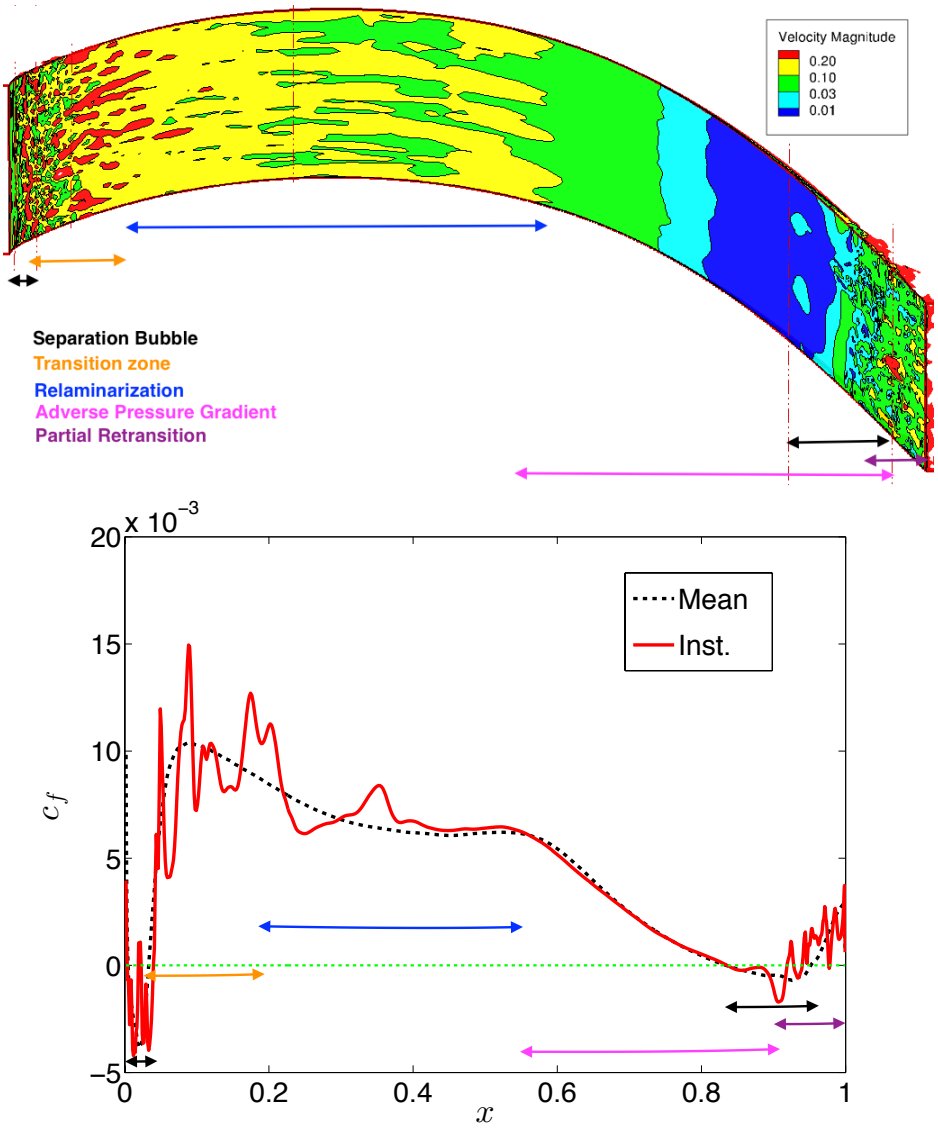

Fig. 5.16 Total velocity contours (top) and skin-friction on the blade at $t = 7.0$. Different regimes are marked. Mean skin-friction is also shown for comparison

values of $\bar{\tau}_w$, and is taken to be the streamwise station just upstream of the computed rise in $\bar{\tau}_w$ seen in Figure 5.19. Because of the sharpness of the rise and the small streamwise extent of the whole bubble at the leading edge ($0.006 < x < 0.05$), the error in estimating x_t is very small.

The linear combination model assumes that

$$\bar{\tau}_w = (1-\gamma)\bar{\tau}_{w_L} + \gamma\bar{\tau}_{w_T} \tag{5.11}$$

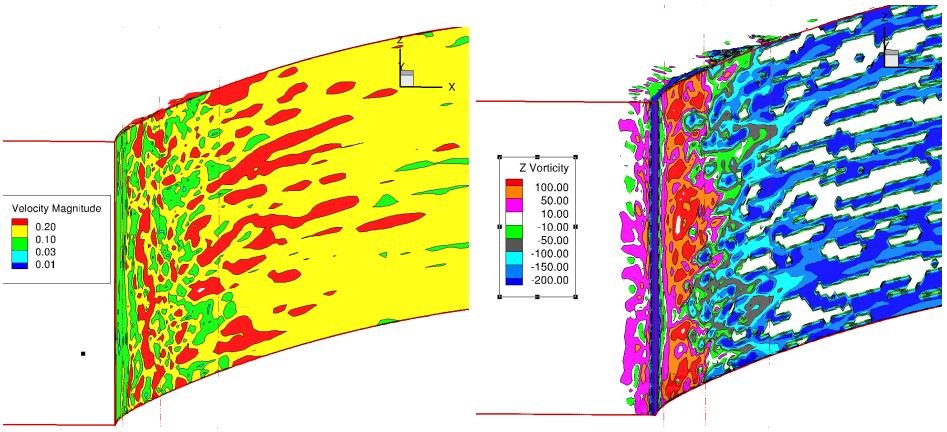

Fig. 5.17 Zoomed view near the leading edge. Left: Total velocity, Right: Spanwise vorticity (ω_z). The onset of transition is upstream of reattachment point

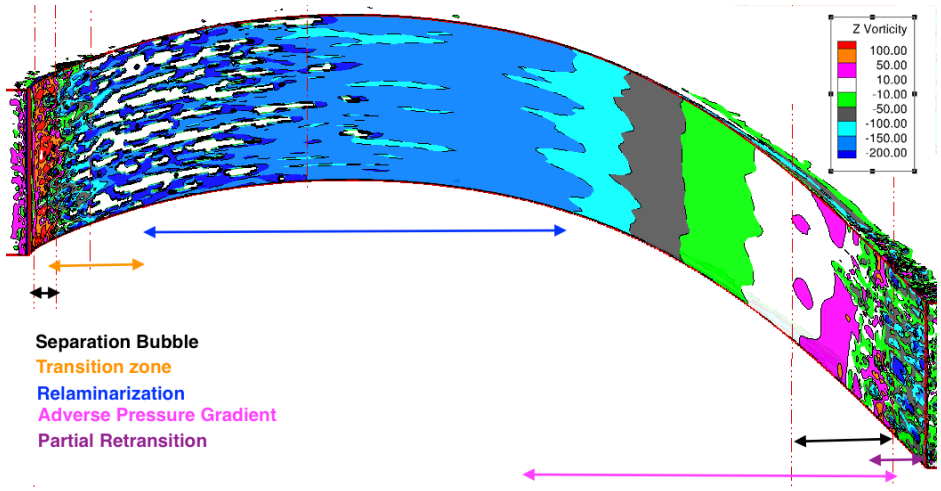

Fig. 5.18 Spanwise vortcity (ω_z) contours on the wall ($t = 7.0$)

based on the hypothesis that the flow is equivalent to that in a fully turbulent boundary layer for a fraction γ of the time, and to that in a laminar boundary layer for a fraction $(1-\gamma)$ of the time, each with its own initial condition as discussed above. This model has been found to give good estimates of $\bar{\tau}_w$ in the transition zone.

We can therefore invert eq. 5.11 to estimate γ from the DNS result for $\bar{\tau}_w$ and from predictions for $\bar{\tau}_{w_L}$ and $\bar{\tau}_{w_T}$ based on the boundary layer equations. The estimates of $\bar{\tau}_{w_L}$ and $\bar{\tau}_{w_T}$ are obtained using laminar and turbulent boundary layer modules (ILBLI and ITBL respectively) available in Boundary layer code developed at the Department of Aerospace and Ocean Engineering, Virginia Tech by Devenport & Schetz (1998).

The variation of γ so estimated is shown in Fig. 5.20. It is seen that γ rises sharply from zero in the neighbourhood of the end of the mean separation bubble, reaches a maximum of

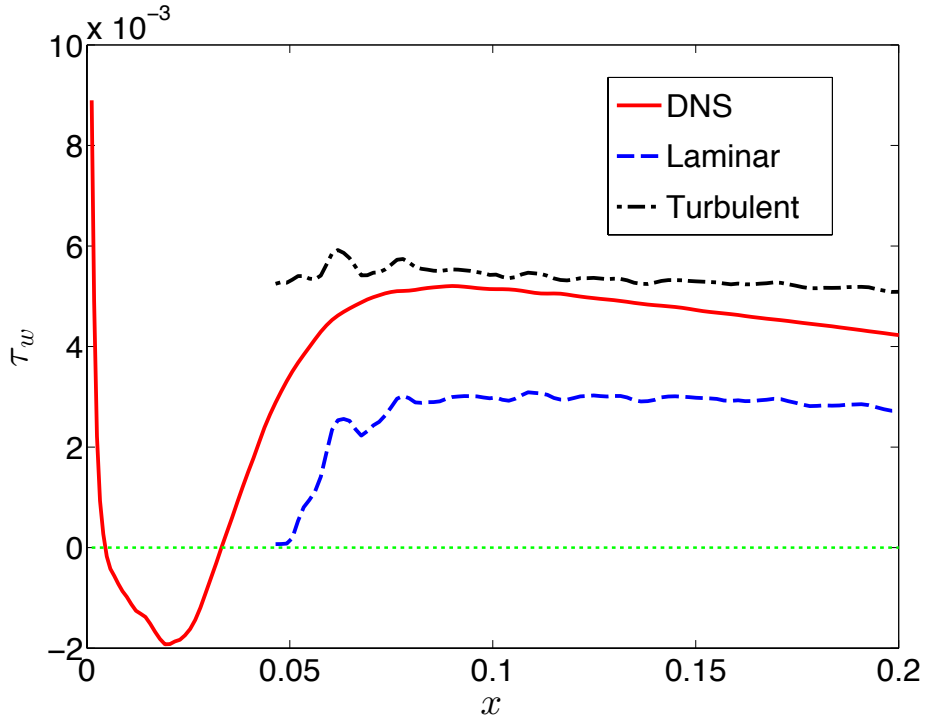

Fig. 5.19 Mean wall-shear stress as obtained from DNS against those with laminar and turbulent boundary layer calculations using same pressure profile. Both boundary layer calculations upstream of the $x \simeq 0.05$ indicate separation.

0.9 at $x = 0.1$, and thereafter slowly declines to lower values. This clearly indicates that the flow never becomes fully turbulent, although transition is nearly complete.

This is followed by a region of favourable pressure gradient, which tends to relaminarize the boundary layer. Both c_f and γ continue to drop. This regime is discussed in Section 5.6.

Further downstream the pressure gradient becomes adverse (Fig. 5.3) at $x \approx 0.6$, leading to the second separation at $x \approx 0.8$. The transition due to this separation is incomplete even as the flow leaves the trailing edge.

Figure 5.21 shows iso-surfaces of Q-variable to detect the vortices. Q is the second scalar invariant of the velocity derivative tensor and can be expressed as:

$$Q = 0.5 \times (\Omega_{ij}\Omega_{ij} - S_{ij}S_{ij})$$

where S_{ij} and Ω_{ij} are the symmetric and the antisymmetric part of the velocity derivative tensor respectively.

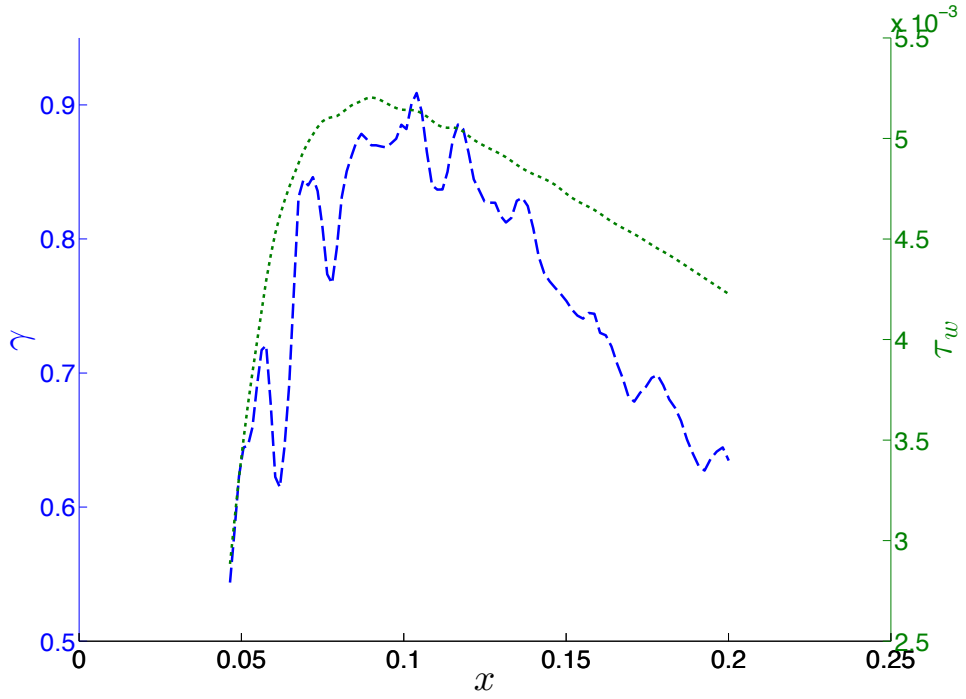

Fig. 5.20 Intermittency γ in the transition zone. Mean wall-shear stress is also plotted.

Once again, the transition zone is visible by the presence of vortical structures near the leading and trailing edges. These structures disappear in the downstream region of the relaminarizing zone.

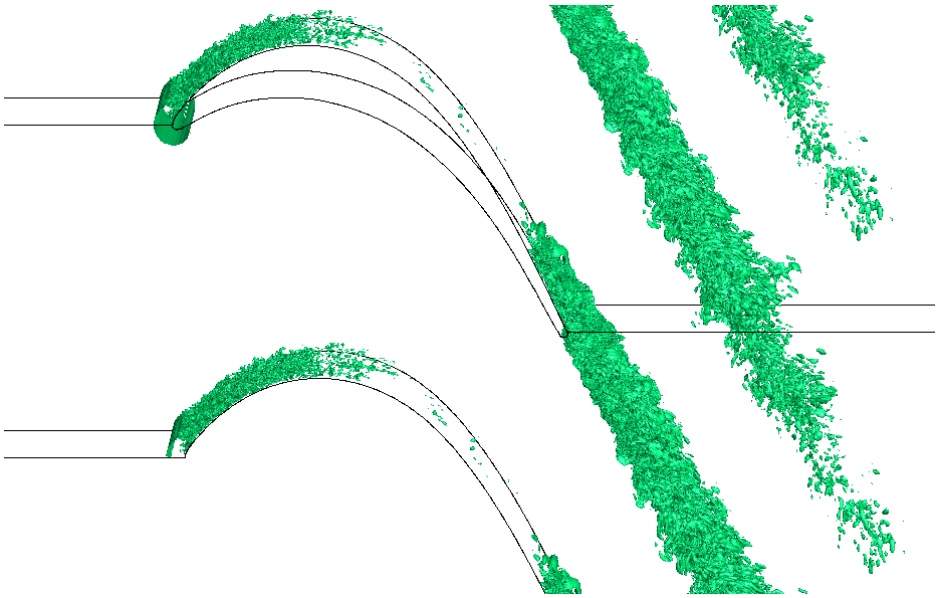

Fig. 5.21 Identification of vortex-structures using the Q-criteria ($t = 7.0$)

5.6 Relaminarization

In the flow past T106A blade at incidence angle of $\beta_1 = 45.5^\circ$, the pressure gradient is largely favourable in the first half of the suction side. The incoming turbulent flow (due to separation-induced transition or free-stream turbulence) may undergo relaminarization in this region. For example, Wilson & Pope (1954) and Wisler (LaGraff 2007) have reported experimental observations of relaminarization on a turbine blade boundary layer(see Chapter 1). It is hence worthwhile to revisit the relaminarization model proposed by Narasimha & Sreenivasan (1973) in the context of the present DNS results, where relaminarization is distinctly noticed.

5.6.1 The Two-layer Model

Narasimha & Sreenivasan (1973), NS73 have proposed a two-layer model, comprising of a viscous inner layer and an outer inviscid but rotational layer, to explain the relaminarization mechanism. This model is briefly explained as follows:

Figure 5.22 (reproduced from NS73) sketches the phases of a typical turbulent flow going through relaminarization and retransition. Relaminarization under strong favourable pressure gradient is a continuous process unlike transition. As shown in the figure, fully turbulent flow in region-I starts relaminarizing after a steep favourable pressure-gradient is imposed. In region-II, the flow is transitional and in region - III the flow is quasi-laminar. The flow retransitions to turbulence again in region-IV.

NS73 have argued that under high favourable pressure gradients, the domination of dynamic pressure on the slowly responding Reynolds stress in the outer layer leads to flow becoming quasi-laminar. The turbulent structures in the outer layer are distorted due to rapid flow acceleration. For all practical purposes, this layer can be treated as inviscid due to Reynolds shear stress being 'frozen' compared to the steep rise in dynamic pressure.

An inner viscous sub-boundary layer develops subsequently to satisfy the no-slip boundary condition. This layer originates from the decaying upstream turbulence and is maintained in a stable state by the accelerated flow on top. The dashed line in region-III depicts the separation between the two layers in this model.

The governing equations for the two layers can be derived from the boundary layer equation

$$u\frac{\partial u}{\partial x} + v\frac{\partial u}{\partial y} = U\frac{dU}{dx} + \nu\frac{\partial^2 u}{\partial y^2} + \frac{\partial \tau}{\partial y} \tag{5.12}$$

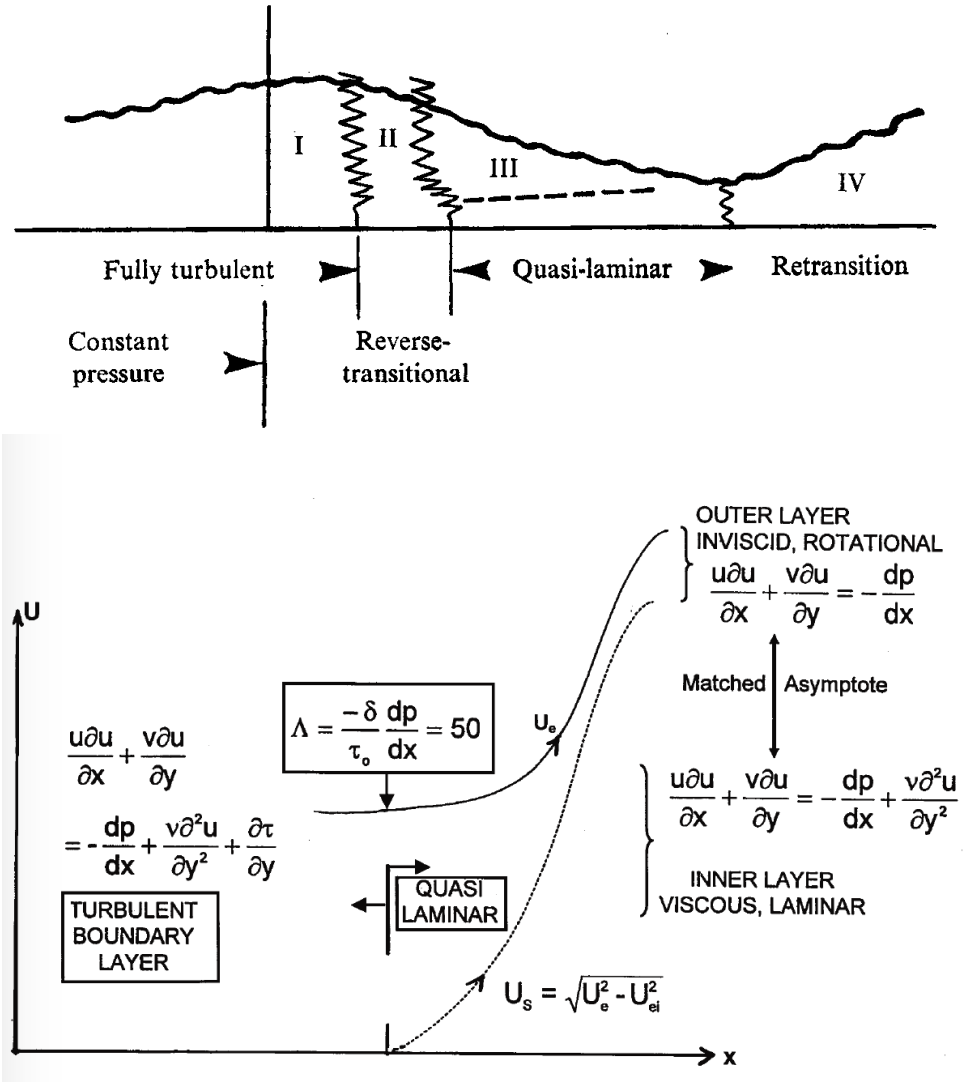

Fig. 5.22 Top: Different regimes in a relaminarizing flow. Vertical axis indicates boundary layer thickness. Dashed line in quasi-laminar region separates viscous inner layer from inviscid outer layer. Bottom: Two-layer theory. (Reproduced from Narasimha & Sreenivasan (1973))

From the above equation, two separate equations are written for the above-defined inner and outer layers, which in non-dimensionalized form using proper variables are given by:

$$\text{Outer: } \overline{u}\frac{\partial \overline{u}}{\partial \overline{x}}+\overline{v}\frac{\partial \overline{u}}{\partial \overline{y}}=U\frac{dU}{dx} \tag{5.13a}$$

$$\text{Inner: } \tilde{u}\frac{\partial \tilde{u}}{\partial \tilde{x}}+\tilde{v}\frac{\partial \tilde{u}}{\partial \tilde{y}}=U\frac{dU}{dx}+\nu\frac{\partial^2 \tilde{u}}{\partial \tilde{y}^2} \tag{5.13b}$$

Here the overbar and tilde represent inner and outer variables respectively.

These equations can be solved using the matched-asymptotic technique as also discussed in section 5.4. The matching boundary conditions are:

$$\overline{u} \to U, \qquad \overline{v} = 0 \qquad \text{as} \qquad \overline{y} \to \infty \tag{5.14a,b}$$

$$\tilde{u}(x, \tilde{y} \to \infty) = \overline{u}(x, \overline{y} \to 0) = \overline{u}_0(x) \tag{5.14c}$$

$$\tilde{u} = 0 = \tilde{v} \qquad \text{at} \qquad \tilde{y} = 0 \tag{5.14d}$$

A new code is written in Matlab to solve these equations directly and also using the approximate method described in Narasimha & Sreenivasan (1973).

5.6.2 Validation against the Bourassa-Thomas Experiment

The new code written for the two-layer model is first verified against the extreme case of steep pressure gradient before using the model for the solution obtained on turbine blades. Bourassa & Thomas (2009) present an experimental investigation of flat-plate turbulent boundary layer at $Re_\theta = 4590$ subjected to steep favourable pressure gradients over a small distance. The peak value of the pressure-gradient parameter, $K = \frac{\nu}{U(x)^2} \frac{\mathrm{d}\, U(x)}{\mathrm{d}\, x}$ thus achieved is 4.4×10^{-6}, which is much higher than the value 3×10^{-6} generally taken to be the lowest value of K at which relaminarization may be observed.

Figure 5.23(a) shows a plot of external velocity as extracted from the plot given in Bourassa & Thomas (2009). A smoothing spline of 3rd-order available in Matlab is needed to fit the velocity in the relaminarized region. This fit is used in calculating the smooth velocity gradients (and hence K) at the grid points in solving the governing equations numerically. The curve obtained using cubic fit is overlapped on the extracted velocity profile in 5.23(a). The pressure-gradient parameter K is calculated using the fitted velocity at every grid point. This is shown in Fig. 5.23(b) along with the experimental points extracted from the original paper. There is little difference between the fitted curve which is used in two-layer model and the experimental data. However due to the necessity of using a smooth and differentiable velocity field in the two-layer model, this difference is unavoidable.

For the region where the flow is turbulent and pressure-gradient is almost zero (between -2.6 and 0 in Fig. 5.23), the boundary layer is solved using an in-house incompressible turbulent boundary layer (ITBL) code with eddy-viscosity model, as given in Schetz (1993).

In the steep pressure gradient region (between 0 and 1 in Fig. 5.23), the two-layer model is used with $x_0 = 0$ as the virtual origin (where quasi-laminar flow starts) . The results thus obtained are shown in Fig. 5.24. It is noticed that in the fully turbulent region, the predictions of shape factor (H) as well as skin-friction co-efficients (c_f) are well predicted by ITBL. However, this model fails to predict these quantities in the strong pressure gradient region.

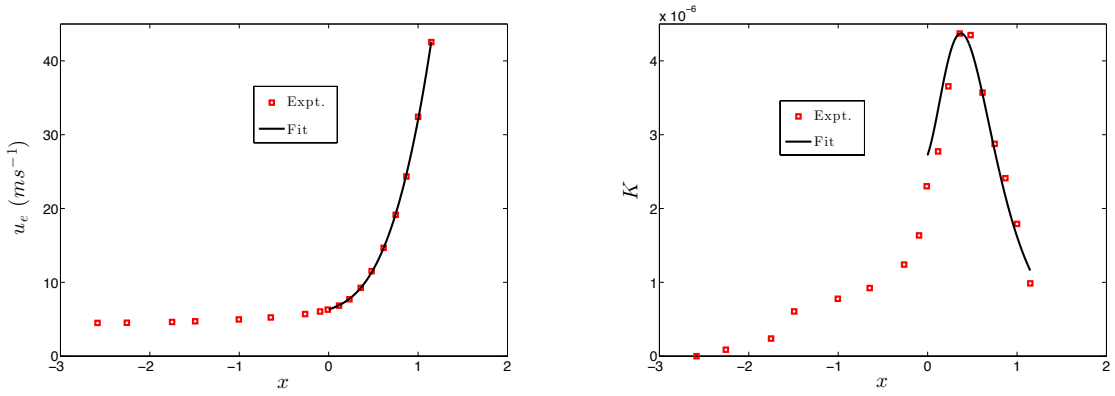

(a) (b)

Fig. 5.23 (a) External velocity along the flat plate along with polynomial fit used for two-layer theory. Points extracted from Bourassa & Thomas (2009). (b) Launder's pressure-gradient parameter K: Extracted points and as obtained from velocity fit. Note the little difference between the experimental points and the polynomial fit

The predictions with the two-layer model in this region are dramatically better. The rapid increase of shape-factor as well as the the substantial decrease in skin-friction co-efficients in the quasi-laminar region are well-predicted by this model. The little difference with the experimental data could be either due to using a fit for the velocity as described above or in choosing the appropriate virtual origin of quasi-laminar flow. The uncertainty in choosing the virtual origin which should be used in two-layer theory is due to a lack of proper definition, as acknowledged in NS73. However it is also shown for a relatively low pressure-gradient case that the choice of virtual origin does not affect the calculations significantly.

Nevertheless, allowing for with the slight difference, the two-layer model is verified for the extreme case of high *Re* high pressure-gradient flow. This model is then used for the relaminarization region in the T106A blade boundary layer predicted using DNS.

Application to T106A blade

Figure 5.25(a) shows the stretch of the T106A blade as obtained with DNS data (grid A), where the pressure gradient is favourable. The fit for the velocity is also plotted on the DNS data. The pressure-gradient parameter using this velocity is plotted in 5.25(b). The peak pressure-gradient parameter is well beyond the value at which relaminarization is experimentally observed. But unlike Bourassa & Thomas (2009), here the acceleration is not very steep and occurs over a relatively longer region.

The two-layer model is then applied on this flow and the results are presented in 5.26. The thinning of the boundary layer in the relaminarization region is well predicted in this

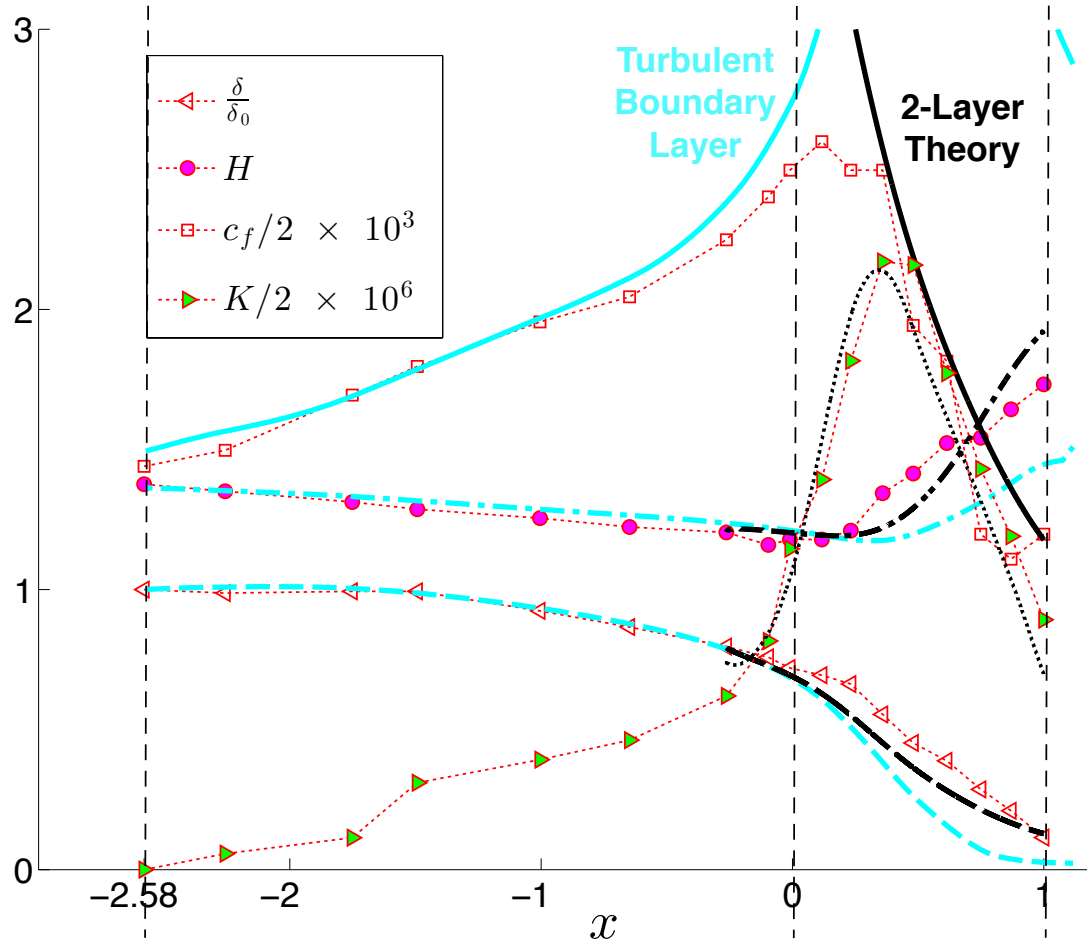

Fig. 5.24 Experimental results of Bourassa & Thomas (2009) compared with incompressible turbulent boundary layer theory (cyan in color) and two-layer model (black in color) in fully turbulent region and quasi-laminar region respectively. .

region. The prediction of local skin-friction coefficient (wall shear-stress normalized by local variables $c_f = \frac{\tau_w}{0.5\rho_e U_e^2}$, subscript 'e' represent values at the edge of the boundary layer) by the two-layer model is also remarkably close to the DNS results downstream of the relaminarization zone.

The motive of this exercise was to show the applicability of the two-layer model in predicting the boundary-layer parameters in the relaminarizing flow on a blade. This model is simple and quick, and does not require any detailed knowledge of turbulent quantities. A suitable pressure-gradient parameter, such as $\Lambda_p \equiv -\frac{dp}{dx}\frac{\delta}{\tau_0}$ (δ is a measure of total boundary-layer thickness and τ_0 is a characteristic Reynolds stress) as defined in NS73, can be used to identify the quasi-laminar zone, if any, in flow over a turbine blade. The two-layer model can then be used to get the quantities of interest very quickly. The underlying basic principle of

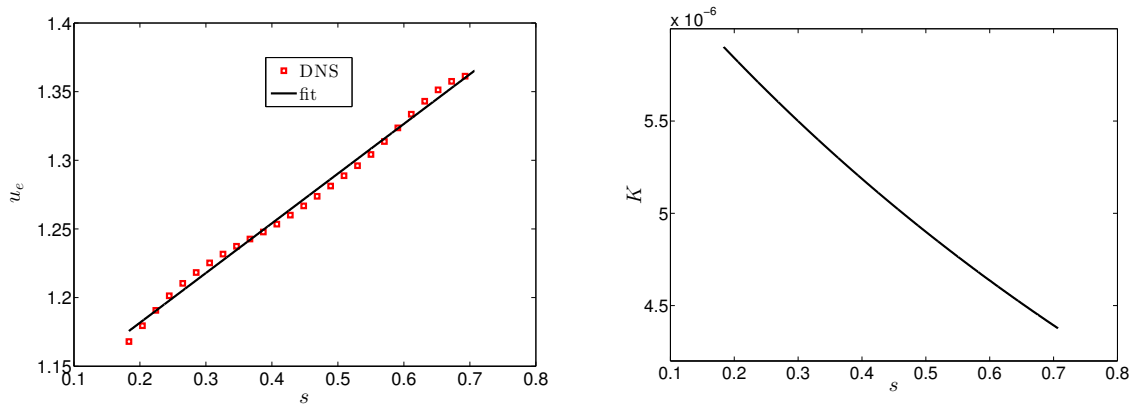

(a) (b)

Fig. 5.25 Quasi-laminar region in flow over T106 blade: DNS results. (a) External velocity (b) Pressure-gradient parameter

this model (frozen Reynolds stress and viscous inner layer) can also be implemented in the existing transition and turbulence models to predict the flow better.

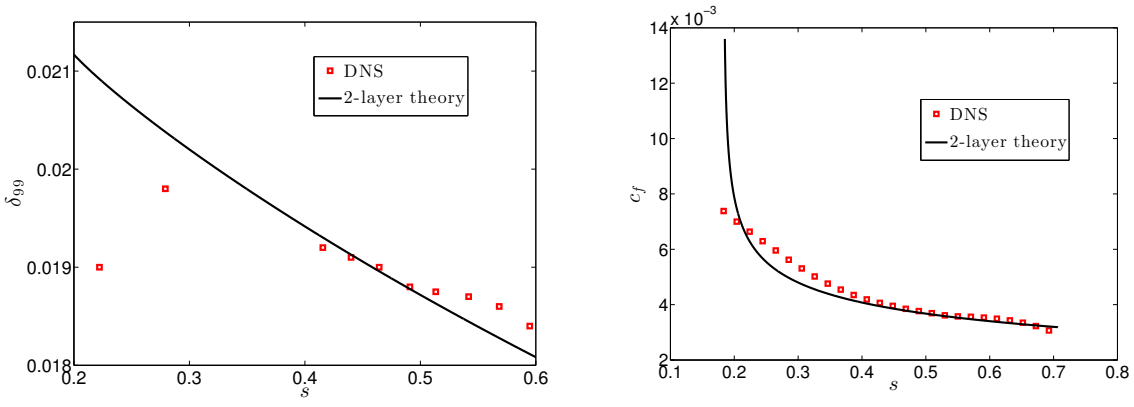

(a) (b)

Fig. 5.26 DNS Vs Two-layer model. (a) Thinning of boundary layer (b) Decrease in local c_f

5.7 Concluding Remarks

In this Chapter, the results obtained with different grids are presented. Four fluid dynamical aspects, namely curvature effects, separation, transition, and relaminarization, are described in some detail.

Interestingly previous work shows that the pressure distribution predicted by the usual methods (and also coarse DNS) shows significant departures from the experimental data.

Various explanations have also been provided for this observation. The present work shows however that DNS predictions on a sufficiently fine grid (160 M in the present case) are needed to provide satisfactory predictions. The fact that high resolution DNS is needed to get even such a basic design requirement as pressure distribution suggest that the BL flow and the outer flow are strongly coupled.

The low resolution DNS results (grids A and B) predict short separation bubbles at both leading and trailing edges. The onset of transition occurs upstream of the reattachment point of the LE bubble, and leads to a steep rise in the mean skin-friction co-efficient with the peak at $x = 0.1$. However the intermittency never crosses 0.9 indicating that the transition is incomplete. Further downstream the flow encounters high favourable pressure gradients and undergoes relaminarization with a continuing drop in mean c_f and intermittency γ. This is followed by an adverse pressure gradient and leads eventually to a TE separation bubble and retransition.

For grid C, the flow remains mostly laminar on both the sides. In the aft region of the suction side, the flow gets separated due to adverse pressure gradient. The bubble formed here is long, compared to the short bubbles present in solutions with grids A and B.

Present theories for modelling curvature effects and relaminarization are evaluated against our DNS results, and they suggest good approximate solutions.

Chapter 6

LPT Blade Simulations: Engineering Parameters

This chapter considers some engineering aspects of the simulations performed here on the T106A blade. As RANS and now LES are the engineering methods to get quick results in industry, this chapter compares the results obtained using these methods against DNS. The validity, scope and limitations of RANS turbulence models in simulating blade flows are also discussed.

The widely used commercial CFD code by Metacomp Technologies, CFD++ ® version 15.1, is used for this purpose. RANS simulations were performed with different turbulence and transition models available in this code. Simulation was also performed using the hybrid RANS-LES model available in CFD++.

Technological parameters such as skin friction (c_f) and heat-transfer (Nu) are also discussed in this chapter. It is also emphasized why it is important to account for instantaneous fluctuations apart from the mean flow for blade design considerations.

6.1 RANS and LES Simulations

6.1.1 Earlier Studies

Several approaches other than DNS, such as RANS, URANS, LES etc., have been used to study the flow past the T106 blade. Apart from these widely used methods, hybrid methods are also being currently attempted. These include methods such as LNS (hybrid RANS-LES), Detached Eddy Simulation (DES), Delayed Detached Eddy Simulations (DDES). Higher order numerical techniques such as Discontinuous-Galerkin (DG) are also becoming popular.

Since the flow on the high lift blade T106A has complex physics at low *Re*, it is one of the favoured engineering problems for study by different numerical approaches.

This section briefly summarises some of the non-DNS computational studies on the T106 blade and hence augments the list presented in Chapter 1. Table 6.1 lists selected RANS and LES studies on the T106A blade where the experimental data of Stadtmuller (2002*a*) is used. This table is not exhaustive and is given only for reference purposes. Present RANS and LES studies are also included in the table.

As mentioned in Chapter 5, the report by Stadtmuller (2002*a*) presents the first RANS study on their own experiments. This RANS study was performed to get the 'real' flow angle that should be used for DNS, as the geometric angle measured in the experiment was uncertain due to the presence of the upstream wake-generating bars. Simulations were performed with RANS solver TRACE (developed by the German Aerospace Center (DLR)) for an inflow sweep angle between 42.5° and 46.5°. The angle 45.5°, which had the best match of c_p with experimental data, was proposed as the likely real flow angle and has been subsequently used for most of the DNS simulations performed to-date. Further RANS simulations were also performed to assess the effect of free-stream turbulence levels on the solution. The turbulence level did not affect the blade loading much but it was noticed that the TE separation occurs only at low FSTI (0.8%) and did not occur at 2.2%. In our non-DNS simulations (described in the next section), however, we show that the TE separation bubble is present even at FSTI of 2.2% when the simulation is performed with the Langtry-Menter transition model or LES, but was missing when a fully turbulent case (without any transition model) was simulated. The details of the turbulence model used in Stadtmuller (2002*a*) are not given. Stadtmuller (2002*a*) also reported secondary flow affects on the T106D blade (which has 30% higher pitch than the T106A), suggesting that the flow is not necessarily two-dimensional in the mean.

Michelassi *et al.* (2002) compared 2D compressible URANS results with their incompressible LES and DNS results on the T106A blade at incidence $\beta_1 = 45.5°$. The URANS simulations were performed using the $k-\omega$ model along with a transition model proposed by Mayle (1991). LES was performed with a dynamic SGS model. RANS c_p results on the suction side seem to match with experimental data better than LES or DNS. This has also been observed in our comparisons with RANS and coarse DNS results. LE separation bubble is noticed in all three computational studies (URANS, LES, and DNS) of Michelassi *et al.* (2002). The LE separation bubble however disappears in the RANS study when simulated with a lower inflow angle of $\beta_1 = 43°$. The dynamic SGS model in the LES is able to predict the behaviour of the suction side boundary layer and is in good agreement with DNS.

Sarkar & Voke (2006) and Sarkar (2007, 2008, 2009) have done extensive incompressible LES studies on this flow, albeit at higher Reynolds numbers (7.8×10^4 and 1.6×10^5 based on inflow velocity) and at a lower inflow angle (37.7°). A moderate grid of size 2 million is used for the studies. The focus of these studies is to understand the influence of periodically passing wakes impinging on the blade. It is no surprise that no separation bubble was found near the LE, which is consistent with our DNS results at this incidence. The separation at the TE leads to transition and is found to be influenced by wake turbulence.

Recently Wang *et al.* (2014) have performed compressible LES simulations on the T106 flow using a self-developed code on a moderate grid of 2.6 million. They also have used a lower inflow angle (37.7°) and a slightly higher Reynolds number (1.1×10^5 based on exit velocity and axial chord) than in the present work. A reasonable match was found in c_p with the Stadtmuller (2002*a*) experiments except near the rear half of the suction side. Consistent with other observations, a separation-induced transition is observed near the TE of the suction side. The boundary layer reattaches before the TE, where an asymmetric Karman-vortex is shed. No separation was noticed in the vicinity of the LE. The RANS simulations reported in Wang *et al.* (2014) are however unable to get pressure distribution or separation sufficiently accurately.

6.1.2 Present Simulations

RANS, LES and hybrid simulations have been carried out here with the commercial CFD code CFD++® version 15.1 by Metacomp Technologies (Chakravarthy 1999) . CFD++ has over 10 turbulence/transition models implemented along with LES, Hybrid RANS/LES (LNS), Detached Eddy Simulation (DES) and variations of Delayed DES (DDES).

For the present fully-turbulent RANS study, the following turbulence models available in CFD++ are used: Spalart-Allmaras (SA), Realizable $k-\varepsilon$, Shear-Stress Transport (SST), $k-\omega$, Hellsten $k-\omega$ with curvature-correction, and $k-\varepsilon$-R_t. Here k and ε are turbulent kinetic energy and its dissipation rate respectively; ω and R_t represent a turbulent frequency and the undamped eddy viscosity of the flow. These models exhibit superior performance in separated flows and therefore have been used for this study. Among transition models, Langtry-Menter transition model was used as it is well validated for transitional flows and does not require any prior input about the transition onset.

The detailed description of these models can be easily found in the CFD literature. Below a brief description of each model is given for the sake of completeness. The implementation of these models is given in the CFD++ manual.

The SA model described in Spalart & Allmaras (1992) is a one-equation model mainly developed for aerodynamic flows. It solves a modelled transport equation for the kinematic

Table 6.1 Selected RANS/LES studies on T106A blade

Authors	**Simulation Type**	**Model**	Re	N_f	N_z	Grid Size[a]	ΔX^+	ΔY^+	ΔZ^+	**Remarks**
Stadtmuller (2002*a*)	RANS	-	51,800[b]	-	-	-	-	-	-	Compressible.
Michelassi *et al.* (2002)	RANS(2D)	$k-\omega$	51,800	256×144	NA	0.04				Compressible.
Michelassi *et al.* (2002)	LES	Dynamic SGS	51,800	444×144	32	2	28	1.8	6	Incompressible.
Sarkar (2007, 2009)	LES	Dynamic SGS	7.8×10^4	384×192	32	2.4	5-80	1-3.5	5-20	Incompressible.
Sarkar & Voke (2006); Sarkar (2008)	LES	Dynamic SGS	1.6×10^5[b]	384×192	32	2.4	5-80	1-3.5	5-20	Incompressible.
Wang *et al.* (2014)	LES	Dynamic SGS	1.1×10^5	390×150	45	2.4	20	1	10	Compressible.
Present	RANS/LNS	SA, $k-\varepsilon$, $k-\omega$,SST	51,800[b]	77,303	32	2.5		1.0		Compressible.
Present	LES	Dynamic SGS	51,800[b]	197,677	50	9.8		0.5		Compressible.

[a] in Millions
[b] based on exit velocity

eddy-turbulent viscosity. This model has been shown to give good results for boundary layers subjected to adverse pressure gradients. The SA model is effectively a low-Reynolds number model and has often been used in turbomachinery applications.

Realizable $k-\varepsilon$ is a two-equation model that solves a modelled transport equation for k and ε. It differs from the standard $k-\varepsilon$ model in the new formulation for the turbulent viscosity and a new transport equation for the dissipation rate (ε). The realizibility arises from the ε-equation, which is derived from an exact equation for the transport of the mean-square vorticity fluctuation. This model exhibits superior performance for flows involving rotation, boundary layers under strong adverse pressure gradients, and separation and recirculation. The $k-\varepsilon-R_t$ is a three-equation model implemented in CFD++ that also solves for the undamped eddy viscosity (R_t) besides solving for k, and its dissipation rate ε. The R_t equation accounts for non-equilibrium conditions and avoids free-stream turbulence decay under shear-free flow conditions.

Hellsten's k-ω model has a solver that uses similar transport equations for k and ω as Menter does, but with explicit algebraic Reynolds stress modelling (EARSM) as a constitutive model. This model is sensitive to pressure gradients, and model coefficients are calibrated for flow phenomena relevant to high-lift aerodynamics. Rotation and curvature effects can be included by using a correction term.

The SST $k-\omega$ turbulence model is a two-equation eddy-viscosity model that combines the best of two models known for their accurate predictions in near-wall and core regions. The $k-\omega$ formulation is used in the inner parts of the boundary layer while a $k-\varepsilon$ behaviour is implemented away from the wall using a blending function. This model is known to give accurate predictions of the onset and the amount of flow separation under adverse pressure gradients. Like SA, SST is also a low *Re* turbulence model recommended for boundary layer flows.

In the $\gamma-Re_\theta$ transition model proposed by Langtry & Menter (2009), SST $k-\omega$ models are coupled with two other transport equations for modelling transition, one for intermittency (γ) and the other for transition onset criteria in terms of momentum thickness Reynolds number (Re_θ).

LES simulation was performed using a one-equation LES subgrid scale model. This model solves a transport equation for the unresolved (subgrid-scale) turbulent kinetic energy. Following Leonard , the residual stress tensor (τ_{ij}^r) in filtered Navier-Stokes equations are split into Leonard, Reynolds and Clark stress tensors, which represent interactions among large scales, subgrid scales and cross-scales between the two respectively. The stresses are modelled using the linear Boussinesq relationship with a subgrid-scale viscosity field that

depends on local grid size. The details of the implementation are given in CFD++® 15.1 Manual .

Various hybrid LES/RANS models are now gaining acceptance because of their not-so-stringent grid requirement as in LES. Hence simulation was also performed with one such LNS model available in CFD++, using the same grid as RANS. In this model, the cubic k-ε model is used for the RANS calculations except in the regions of uniformly-refined mesh where it switches to a Smagorinsky model based LES. The Large-Energy STimulation (LEST) option in LNS, recommended for flows involving attached boundary layers, thin separation etc., is turned on for the current simulation. This option feeds the statistically-represented turbulence energy into directly-resolved scales of motion, and hence provides an automatic unsteady inlet condition for any embedded LES regions.

The flow on the blade is solved using 'Preconditioned Compressible Perfect Gas Navier-Stokes' solver as the Mach number of the flow is quite low. The flow is solved in dimensional form using the values given in Stadtmuller (2002*a*). At inflow, total pressure and temperature are specified along with the flow direction. At the outlet, back pressure is imposed using characteristics-based boundary conditions. Isothermal no-slip boundary conditions are applied on the blade surface. All the simulations were performed with the free-stream turbulence level of 2.2%.

The details of the grids used for RANS and LES simulations are listed in Table 6.1. Both simulations were performed in 3D. The computational domain (shown in Fig. 6.1) used for these simulations is bigger than that used for DNS studies with ANUROOP (Chapter 4). The dimensions in periodic (pitch-wise) direction are the same, but inflow and outflow boundaries are now located one l_{ax} upstream of the LE and two l_{ax} downstream of the TE respectively. This is to avoid reflection of any spurious waves at these boundaries as no buffer layer is used in these simulations. The spanwise distance is kept the same as in DNS ($0.2l_{ax}$), except in LES where it is reduced to $0.15l_{ax}$. This is done to get a finer mesh for LES in the spanwise direction without unduly increasing grid size. The spanwise width for the present LES was chosen based on the data of other investigators for similar flows at same or greater *Re*. For example, the number chosen here is same as adopted by Michelassi *et al.* (2002) for their LES study. Sarkar (2007) have used a slightly lower width ($0.12l_{ax}$) and states that it *"was found to be sufficient to allow three-dimensional instability and turbulence structure to develop."*

It is evident from Table 6.1 that the total grid size used here for the LES study is four times larger than the other studies listed. The face-mesh of the RANS grid is also twice as fine as used in Michelassi *et al.* (2002), with a third dimension also added.

Figure 6.2 shows the distribution of the first-cell distance in wall-units (Y^+) on the suction side of the blade. This value is maintained less than 1 for most of the blade, and hence a solve-to-wall approach is used in the simulations without invoking any wall-function.

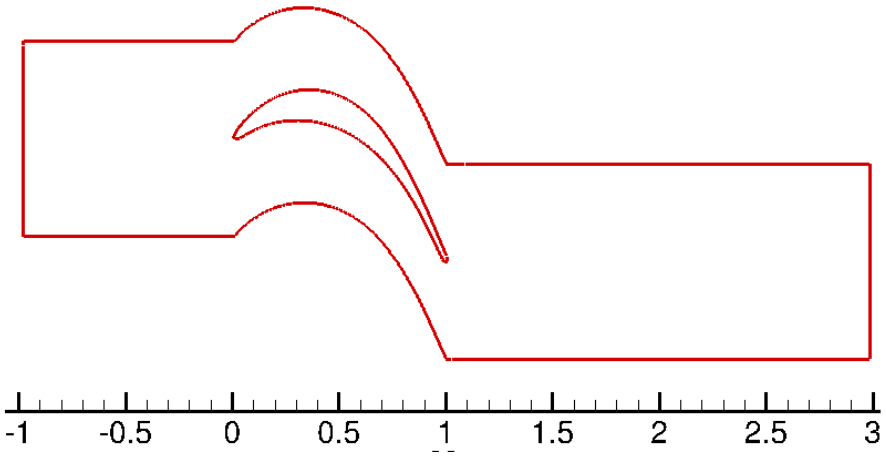

Fig. 6.1 Computational domain used for LNS.

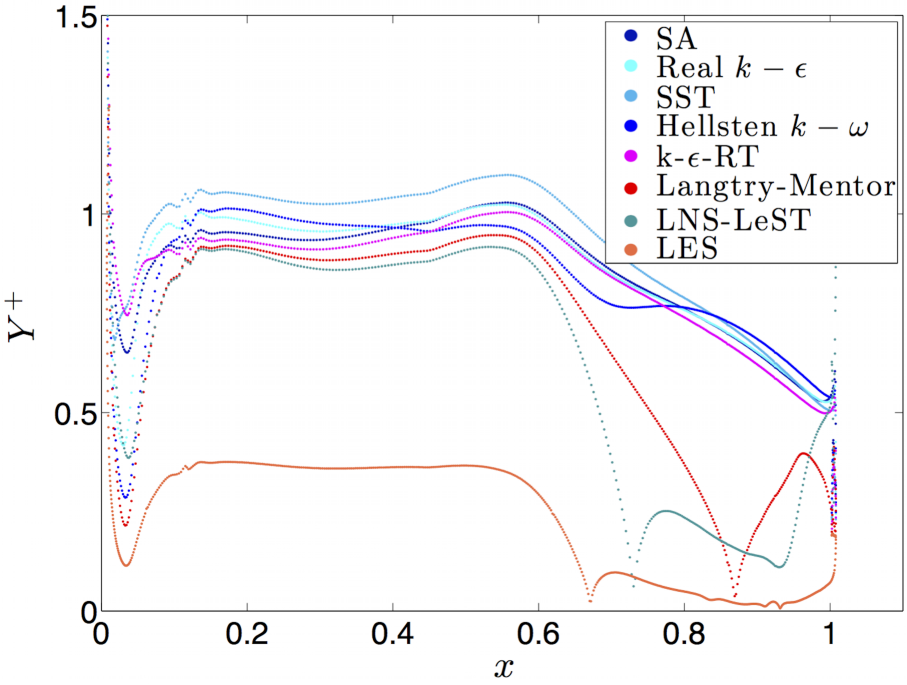

Fig. 6.2 RANS, LNS and LES: Y^+ on the suction side of the blade

Figure 6.3 shows the pressure co-effcients (c_p)as obtained with different turbulent, transition models as well as LNS and LES. As expected, the predictions with RANS is good

on the pressure side, but they consistently fail to predict the separation on the suction side in the absence of any transition model. The same trend is observed in the isentropic Mach number (M_{is}) distribution on the blade (Fig. 6.4). The isentropic Mach number is included in the experimental report of Stadtmuller (2002*a*) and is derived assuming isentropic expansion between inlet and exit as follows:

$$M_{is} = \sqrt{\frac{2}{\gamma - 1}\left[\left(\frac{P_{t1}}{P_{ref}}\right)^{\frac{\gamma-1}{\gamma}} - 1\right]}$$

Here P_{t1} is the total pressure at the inlet and P_{ref} is the back pressure at the outlet.

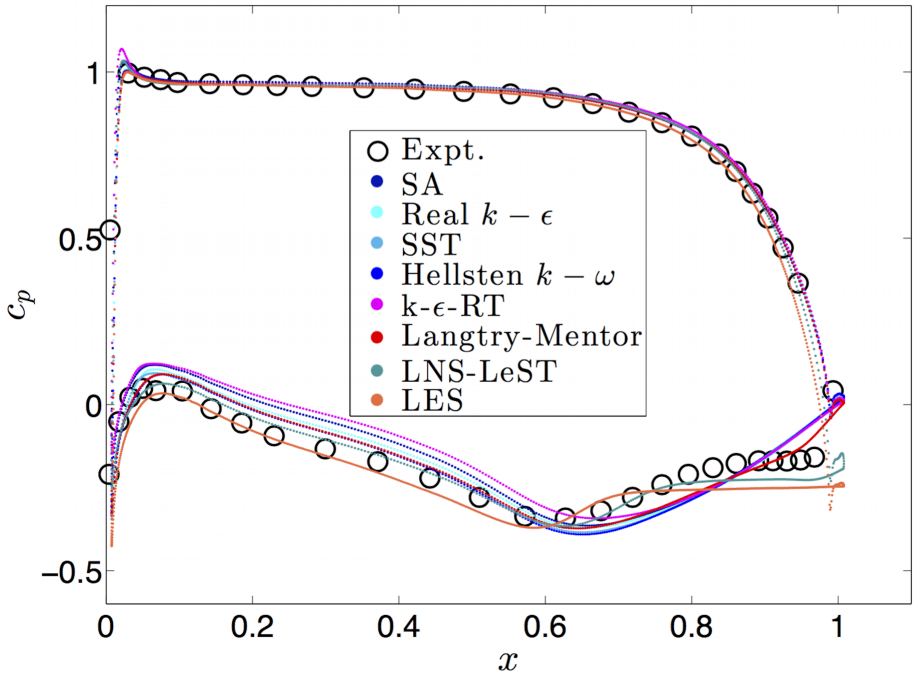

Fig. 6.3 RANS, LNS and LES: c_p on the blade

When SST $k-\omega$ is augmented with the Langtry-Menter transition model, separation is predicted near the trailing edge of the suction side as marked by the small kink in the pressure distribution, though the predicted separation point is slightly downstream of the experimental one. This separation is clearly visible in the skin-friction distribution (Fig. 6.5) and the streamline plot (Fig. 6.6). Figure 6.8 shows the intermittency distribution as obtained using this model. The onset of transition on the suction side is upstream of the reattachment point predicted by the model.

A similar view is shared by Marciniak *et al.* (2010) who have used the updated DLR-TRACE code to study the effect of turbulence models on predicting separation-induced

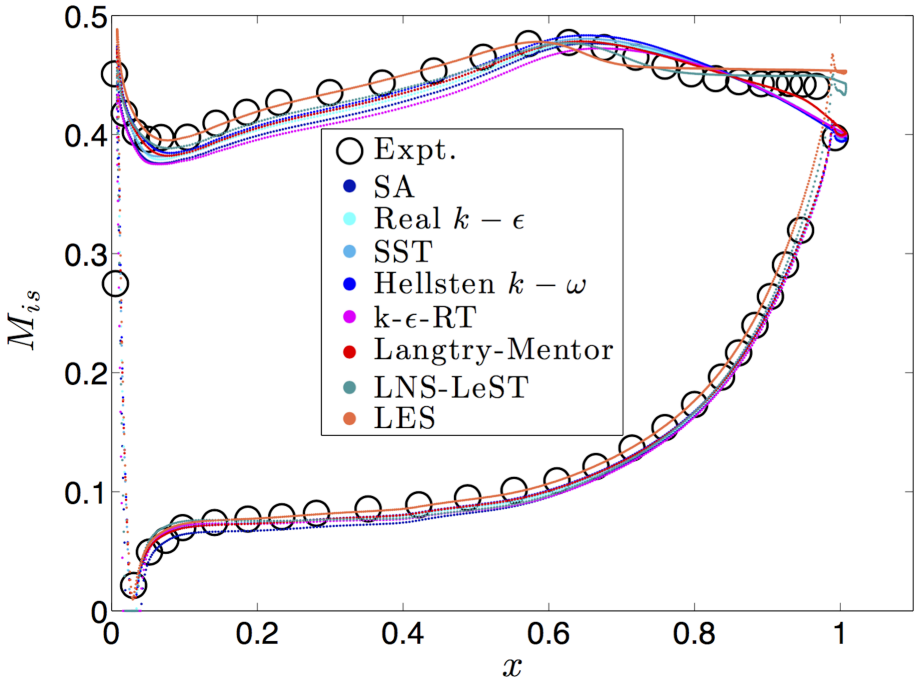

Fig. 6.4 RANS, LNS and LES: Isentropic Mach number distribution on the blade

transition at transition *Re* of 150,000 - 500,000 on the T106A blade. The fully turbulent simulation with Wilcox $k-\omega$ model fails to predict any separation at these values of *Re* . However their simulations with the Langtry-Menter transition model as well as their in-house multimode transition model predict separation adequately well. They however suggest tuning of parameters in the Langtry-Menter transition model in the context of LPT flows to predict the losses well.

The current study is performed with even lower *Re* and hence provides a stricter validation case for transition models. In this context, the Langtry-Menter transition model implemented in CFD++ has the capability to predict separation, however the difference in the pressure distribution on the suction side (see Fig. 6.3), compared to experiment, suggests further tuning of the parameters.

LES predicts a huge separation at incidence of 45.5° right from the middle of the blade on the suction side (Fig. 6.6). The flow never shows any sign of reattachment. The pressure distribution is compared with experiment in Fig. 6.3. It seems that the separation point is predicted too early, which leads to flow being fully separated. It may be because of lack of sufficient resolution (in either space or time or both) that is required for the boundary layer in LES, as the hybrid RANS-LES (also shown in Figure 6.3) predicts the separation much better.

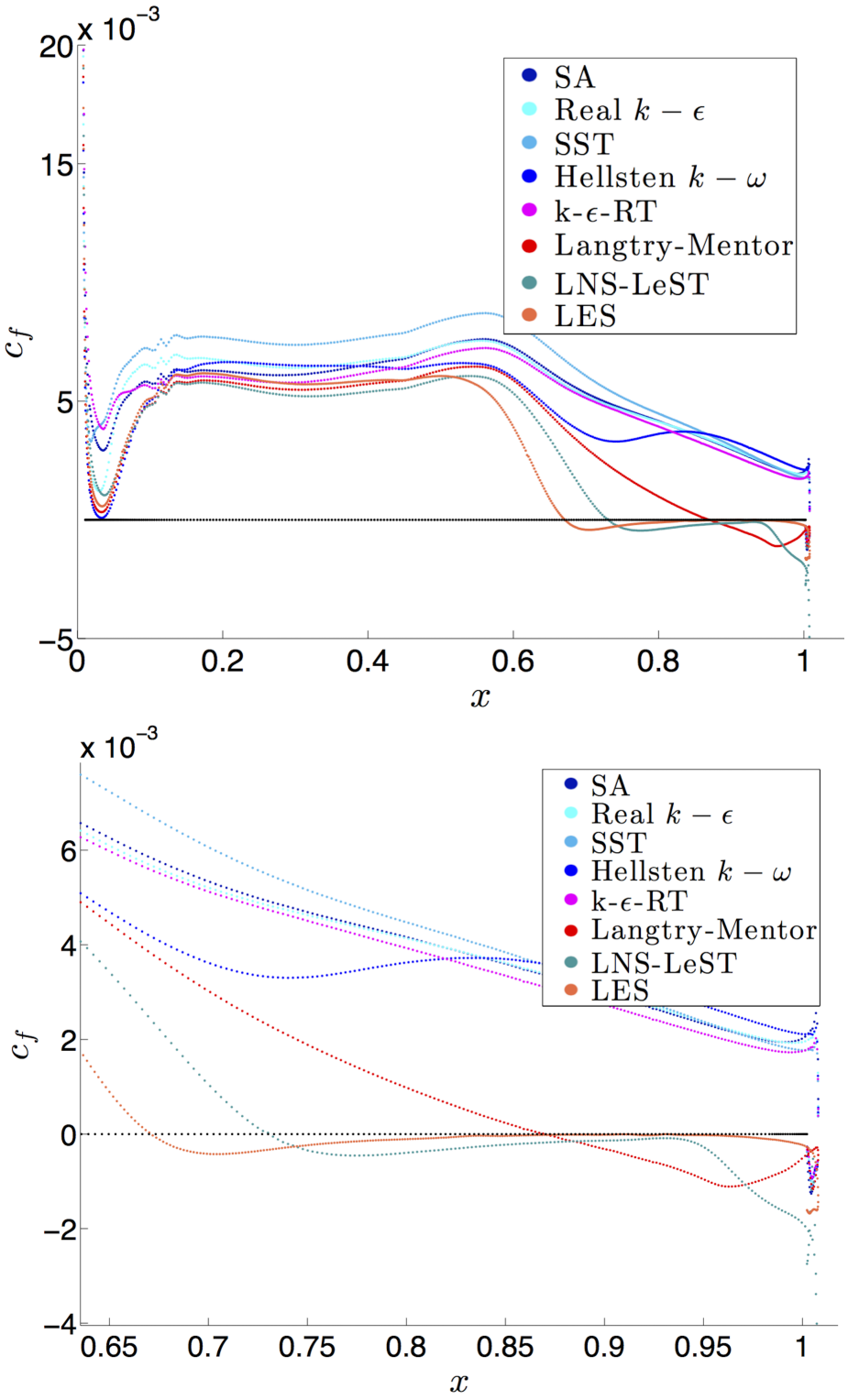

Fig. 6.5 RANS, LNS and LES: Skin-friction on the blade. Top: Full suction side, Bottom: Zoomed near the trailing edge

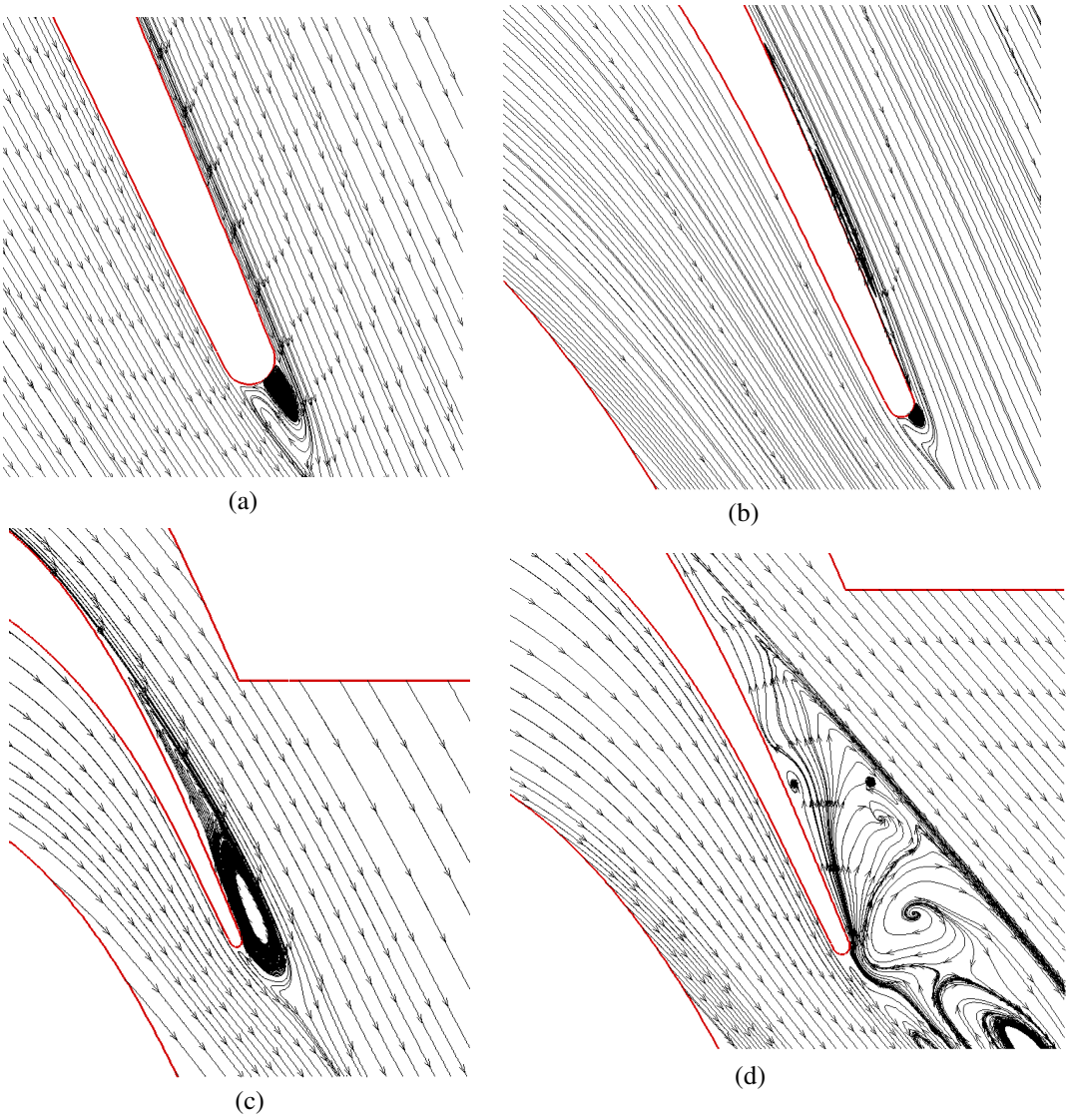

Fig. 6.6 TE Separation Bubbles: (a) SST $k-\omega$ (b) Langtry-Menter (c) LNS-LeST (d) LES

Hybrid RANS-LES or LNS gives the best possible match with experimental data compared to other RANS and LES simulations. As it can be noticed in Fig. 6.3, there is little departure from the experimental data at the end of the TE on the suction side, and the separation point is also accurately predicted. Separation points predicted by the transition model, LES and LNS are shown clearly in skin-friction plot (see zoomed view in Fig. 6.5). The same can be seen visually in the streamline plot (Fig. 6.6). LE separation is not observed in any simulation. Figure 6.7 shows the pressure and Mach contours on the domain as obtained from the LNS simulation. The separation can be identified in the Mach contours plot by the low velocity region (blue in colour).

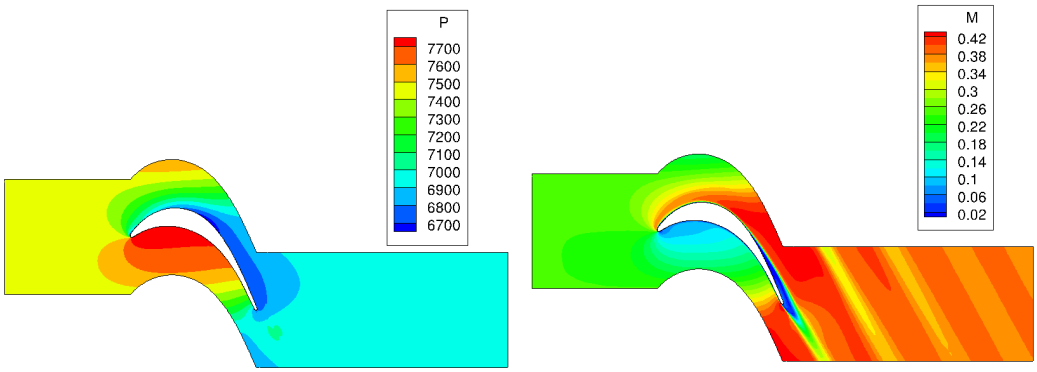

Fig. 6.7 Results with LNS. Pressure (left) and Mach (right) contours

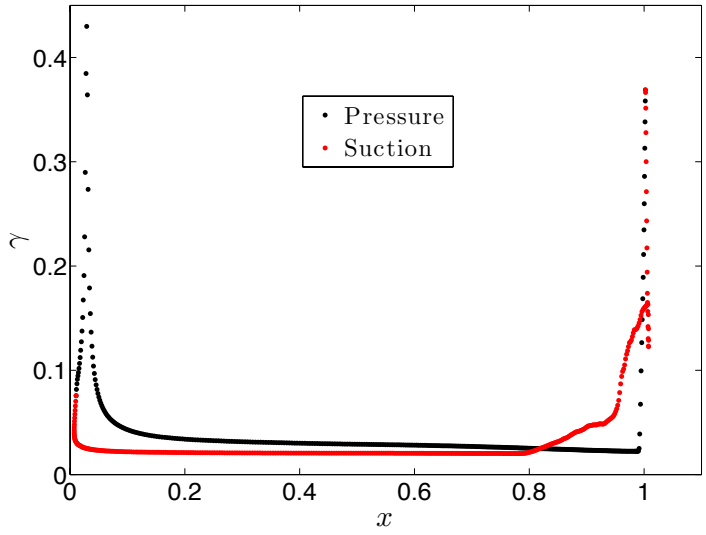

Fig. 6.8 Intermittency distribution on the blade as obtained by $\gamma - Re_\theta$ transition model

LNS results qualitatively as well as quantitively are closest to the results obtained with finest grid (C) DNS simulations. This shows a good potential as an industrial tool to study flow on an LPT blade. However, this model lacks in its present form the capability to predict some of the fluid-dynamical aspects described in Chapter 5, such as curvature effects, relaminarization and retransition for a more complex flow. Also sometimes the instantaneous field is important for a designer as the fluctuations around the mean can be very high, specially in transitional regions. This aspect is covered in the next section.

6.2 Importance of the Instantaneous Field

Fluctuations in wall stress and surface heat flux are of considerable technical interest, as large departures from the mean value can have significant effects on engineering design parameters. For example, high values of surface heat flux can (even when relatively rare) affect material properties adversely and reduce blade life.

We first examine the skin friction coefficient c_f. Mean skin-friction ($\bar{c}_f$) plots for different grids are shown in Section 5.3 of Chapter 5. Here we analyze the data obtained with grid A, where the LE separation on the suction side makes the flow complex and hence large fluctuations around the mean are observed. This section in some sense augments our findings on transition zone for this flow as described in Section 5.5.

Figure 6.9 shows the distribution of the mean value c_f along the chord, marking the peak towards the end of transition, with a continuing drop thereafter due first to relaminarization and next to adverse pressure gradient, followed by a separation bubble and an incomplete retransition. Superposed on the mean skin-friction ($\bar{c}_f$) distribution are 6 instantaneous distributions along the chord sampled at different instants, showing that the fluctuations are highest at the first transitional peak and at the beginning of the second (re)transition. Figure 6.10 shows the probability density (PDF) function of the instantaneous c_f at $x \simeq 0.08$ where intermittency $\gamma = 0.85$. It is seen that the PDF is unsymmetrical, and a Gaussian-like distribution around the mean is followed by a relatively fat tail.

Figure 6.11 shows the cumulative distribution (CDF) at 4 different locations: within the separation bubble ($x = 0.03$), in the transition zone ($x = 0.08$), at the middle of the blade in the relaminarizing zone ($x = 0.6$), and in the retransition zone ($x = 0.97$). Near the separation and transition zones, there is a tail on the positive c_f side of the PDF. This is clearer in Fig. 6.10, where the PDF also shows a longer tail on the positive c_f side. From the CDF at $x = 0.08$, it is seen that there is a probability of 10% that the $c_f > 1.5\bar{c}_f$, or $< 0.4\bar{c}_f$.

Figure 6.12 shows chordwise distribution of the Nusselt number (Nu) on both sides of the blade. The Nusselt number is defined as:

$$Nu = \frac{q_w}{(kT_w - T_\infty)} \equiv \frac{-1}{1-\alpha_T}\frac{\partial T}{\partial \eta}$$

where q_w is the heat-flux at the wall, k is the thermal conductivity of the fluid and α_T is the ratio of free-stream to wall temperature.

As expected, the mean and instantaneous values of Nu superimpose on each other on the pressure side, but are very different on the suction side, where phenomena like transition, relaminarization and retransition change the structure of the flow with time. Figure 6.13 show Nu distributions with 6 superposed samples taken at different instants. The result for

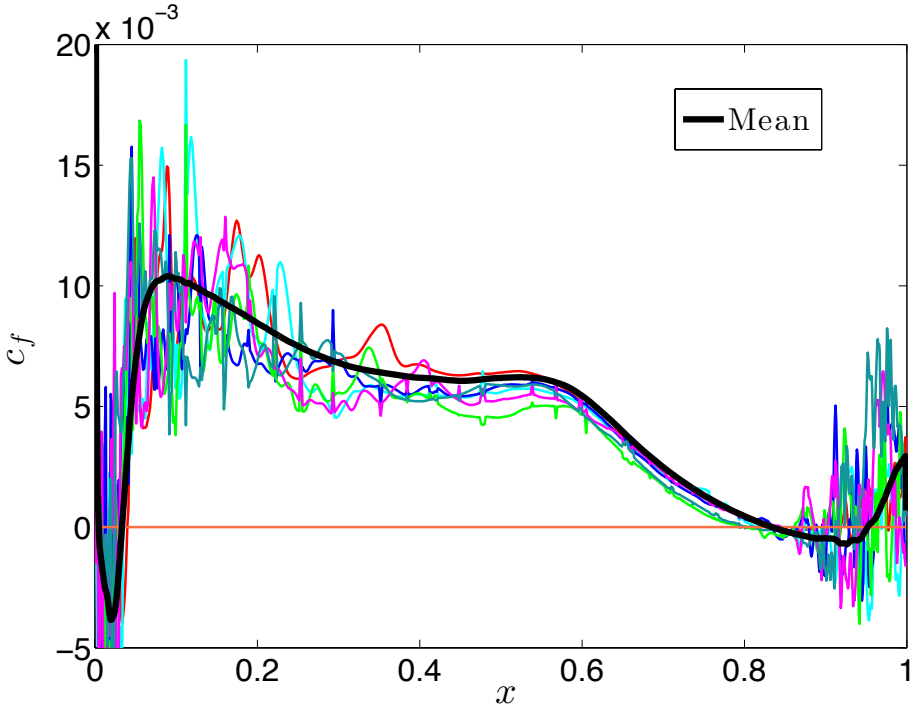

Fig. 6.9 Scatter plot for the skin-friction on the suction side

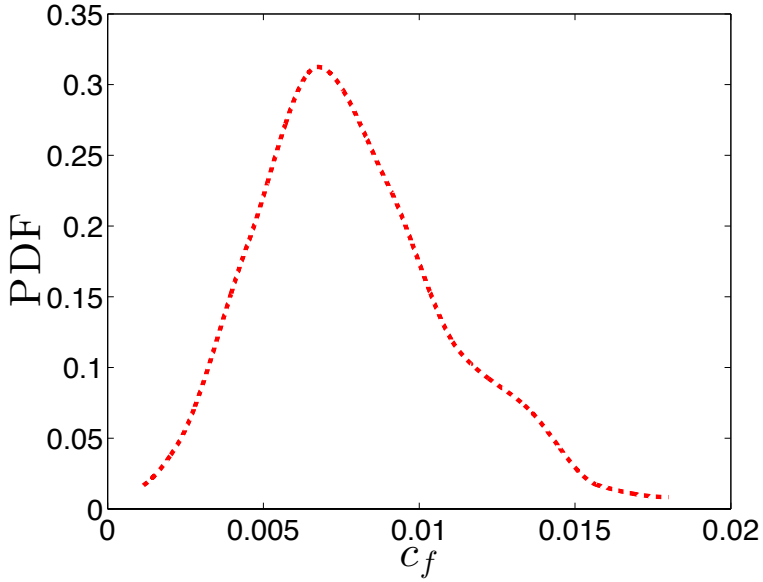

Fig. 6.10 Probability density function plot for the skin-friction at $x = 0.08$ (just after the LE separation) on the suction side

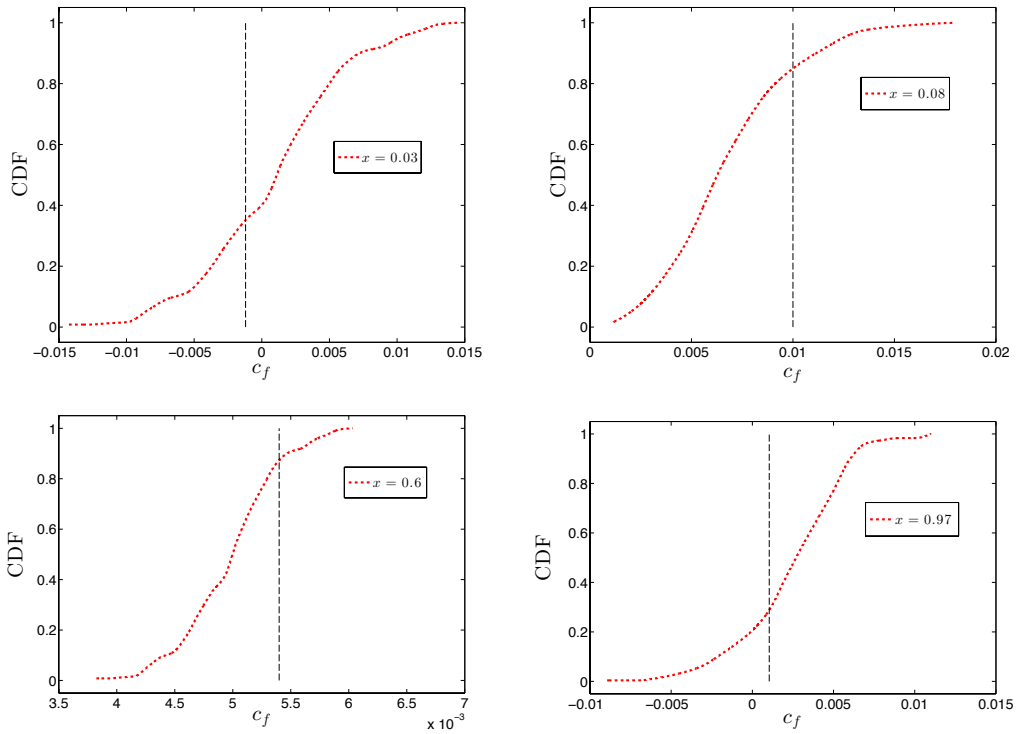

Fig. 6.11 Cumulative distribution function plot for the skin-friction at different locations on the suction side. Dashed line represents $\bar{c}_f$

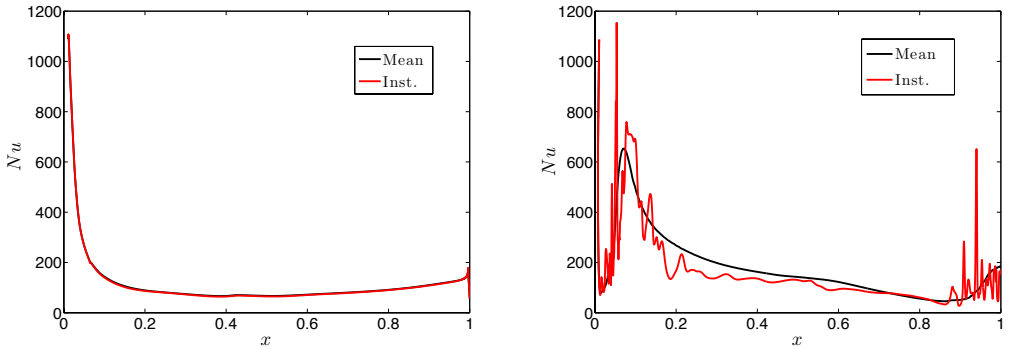

Fig. 6.12 Nusselt number on the blade. Left: Pressure side, Right: Suction side

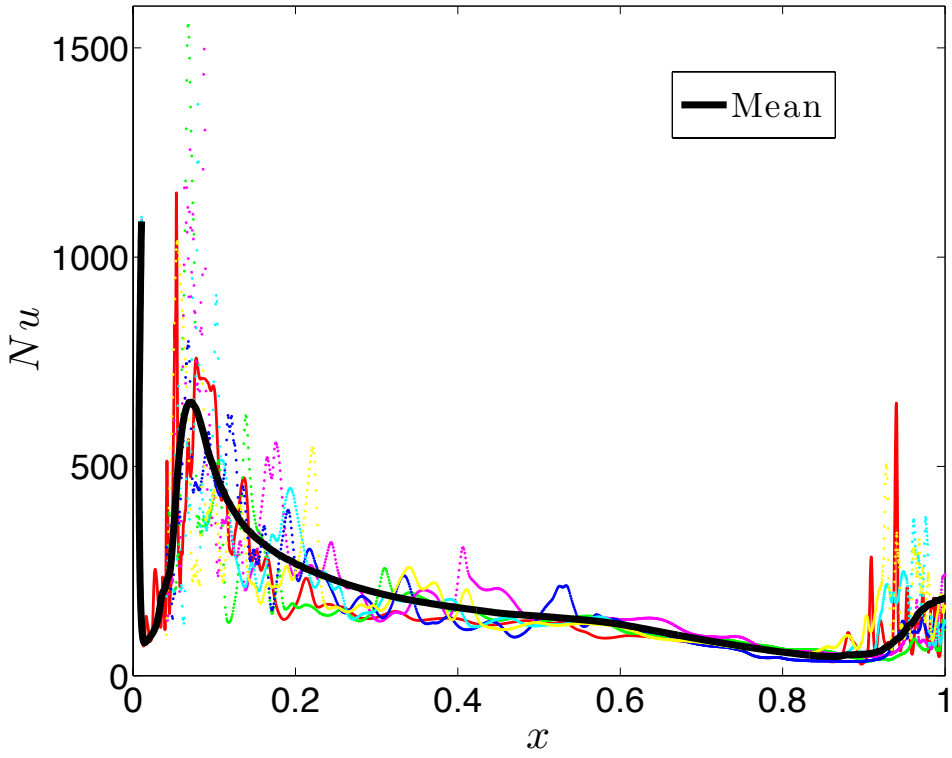

Fig. 6.13 Scatter plot for the heat-flux on the suction side

Nu is rather similar to that of c_f, except that the fluctuations are larger and the distributions spikier. Thus, around the first peak in mean *Nu* at $x \simeq 0.1$, the highest instantaneous value is nearly 2.5 times the mean; the second peak, at $x \simeq 0.95$, is about 8 times higher than the local mean.

It is interesting that both c_f and *Nu* exhibit significant fluctuations in the relaminarizing zone, as may be expected from velocity fluctuation data shown in the experiments of Bourassa & Thomas (2009). However the fluctuations tend to diminish to very low values in the adverse pressure gradient region, before flaring up again as retransition sets in.

More detailed statistics of wall stress and surface heat flux data are being generated.

6.3 Concluding Remarks

In this chapter, results obtained with RANS, LES, and hybrid RANS/LES (LNS) flow in the T106A linear turbine cascade are presented. RANS simulations are performed with a variety of turbulence models which are considered satisfactory for separating flows. But in the present set-up of flow between row of consecutive blades at low *Re* and high incidence, these

models fail to predict any separation. However RANS simulations , when performed with the Langtry-Menter transition model predict separation at the TE. The pressure distribution obtained with this simulation however is significantly different compared to experimental data on the suction side.

LES and LNS both predict separation at the TE. The prediction with LES however is upstream of the actual separation point in the experiment. This may suggest requirement of more highly resolved grids as the results with LNS are very close to the experiment. These models however lack modelling for curvature effects, relaminarization etc.

The engineering parameters of interest, such as skin-friction and Nusselt number, are analyzed for mean as well as instantaneous flows using the present DNS results. The peaks of these parameters show significant variation in time suggesting the importance of time-accurate simulations for design considerations.

Chapter 7

Conclusions and Future Work

The focus of the present thesis is the study of flow past an LPT blade mounted in a linear cascade at high incidence through boundary layer DNS. Every chapter carries at its end a summary of the conclusions reached based on the contents of the chapter. Here we offer a brief overview of the whole thesis, followed by a short list of topics that require further meticulous investigation.

7.1 Conclusion

The efficiency of a gas turbine depends greatly on managing the complex fluid-dynamical phenomena that occur on a blade. These phenomena include separation, transition, and relaminarization. To understand these phenomena, a simplified flow between two consecutive rows of blades is investigated through DNS studies, as the current turbulence models are still not considered satisfactory to study this class of flows. The fact that turbine blade Reynolds numbers are in the range 20,000 to 1 million, and that quite a few turbines operate at Re of order of 10^5, make the flow on the turbine blade accessible to DNS studies with the computing power that is currently available. With the rapid increase in computing power that we are seeing at present, it would seem that it should be possible to reach Re in the range $10^5 - 10^6$ within the coming decade.

Based on this reasoning, several attempts have recently been made to provide DNS results, especially on the T106A low-pressure turbine blade on which experimental data is available at low Reynolds number ($Re \approx 50,000$) from experiments carried out at the Universität der Bundeswehr München, Germany. However most of these simulations are directed towards flow in the passage between the blades in a row, rather than towards detailed investigation of the complex phenomena in the boundary layer whose management can lead to more efficient designs.

This thesis has the objective of filling this gap by performing a simulation that may be called 'boundary layer DNS' for the turbine blade without appealing to any turbulence model. The main governing parameters chosen for the flow are those that are particularly rich in fluid-dynamical aspects, and hence beyond the reach of current low-order approaches. The Reynolds number and incidence angle chosen for the present simulations are, 51,831 and 45.5° respectively. The flow at this low *Re* is suggestive of transitional flow, and the high incidence (compared to the design incidence of 37.7°) makes the flow susceptible to separation. A new code, called ANUROOP, has been developed de novo for this purpose. This code handles compressible flows and has a flow solver which has been well validated from Mach 0.1 (Taylor-Green vortex) to Mach 1.5 (compressible channel flow).

The present emphasis on the BL demands the design of special grids that are tailored to the problems considered, namely the very high resolution required near the wall, with the first grid point 0.1 wall unit from the surface. Also simulations have been mainly at three grid resolutions (in terms of the total number of grid points): 25 M (A), 47M/95M (B/B1), and 160M (C), the last being by far the highest resolution attempted to-date at this *Re*.

Even with this emphasis on boundary layers, our focus in this thesis is on obtaining a broad appreciation of the nature of the flow rather than a very detailed analysis of all the results (which is currently in progress). Furthermore, while two of the simulations on grid C have free stream turbulence intensity (FSTI) in the range 0-10%, no impinging wake perturbations are considered. The reason for this is that the current objective is to test the power of ANUROOP and the dependence of the solution on various numerical parameters implied in the code and, in particular, the resolution.

The main findings may be briefly summarized as follows:

The first striking result is about the fundamental engineering target of the pressure distribution on the blade. It turns out that turbulence models in general, and even LES, are not capable of satisfactorily reproducing the pressure distributions measured on T106A, especially on the suction side. Even with DNS, the low resolution codes A and B show appreciable discrepancies but the high resolution grid C gives results very close to measurements. This finding suggests why DNS could become a useful tool in design.

Secondly, near the leading and trailing edges, the effect of surface curvature is visible from the boundary layer velocity profiles, which show a maximum velocity which would roughly correspond to the location of the thickness of the BL, dropping linearly with the normal coordinate at distances beyond the velocity maximum on a convex surface. Within this region, the curvature is sometimes so high that higher order boundary layer theory has to be used. A new boundary layer code for solving higher-order theory was therefore written,

and comparisons with DNS profiles near the leading edge show excellent agreement with the theory, which departs substantially from the lowest order Prandtl boundary layer theory.

The boundary layer calculations with grids A and B reveal a complex behaviour beginning with a short separation bubble very near the LE, immediately followed by (or even triggering) a transition towards turbulent flow. This is confirmed by the steep rise in the skin-friction coefficient c_f in the transition zone. However, an estimate of the intermittency in the transition zone suggests that it reaches a maximum value of 0.9 at $x = 0.15$. Somewhat surprisingly at first, the intermittency keeps dropping downstream from its peak value of 0.9, but this provides an indication that the boundary layer may be relaminarizing as it encounters a favourable pressure gradient following peak c_f, with a Launder acceleration parameter K above 3×10^{-6}.

DNS results for a variety of other parameters during relaminarization show reasonable agreement with a two-layer theory, where there is an outer layer of rotational but inviscid flow riding over a very thin sub-boundary layer dominated by viscosity and stabilized by a favourable press gradient. This model gives a satisfactory description of the fall in skin friction c_f in the favourable pressure gradient region on the blade.

Beyond $x = 0.6$, the pressure gradient changes from favourable to adverse, but c_f continues to fall as may be expected. With the destabilizing effect of the adverse pressure gradient, the relaminarized BL first exhibits a separation bubble, immediately followed once again by another incomplete retransition towards turbulence.

The DNS results give very interesting images of the structure of rolls within the bubbles and with multiple bubbles (upto 3) within a single bubble in the mean flow. These 'mini-bubbles' in the instantaneous picture interact among themselves, merging and splitting every now and then, making the flow structure of the single mean bubble very dynamic.

At the highest resolution C, however, the LE bubble disappears and the flow remains laminar (with neither transition nor relamarization) all the way up to the TE bubble, which now qualifies to be categorized as 'long' and is marked by a correspondingly long region of nearly constant pressure.

One advantage of the present DNS simulations is that they enable computation of the probability function governing the fluctuating wall stress, with a short tail at low to negative wall-stress and a long tail marking large positive stress fluctuations. The heat-flux also shows similar behaviour, but with much stronger fluctuations from the mean values.

Several RANS, LES and hybrid RANS/LES studies on the T106A blade in a cascade were also made using the commercial code CFD++. A range of turbulence models were used for RANS simulations, however they were not successful in predicting the separation on the suction side of the blade. The SST $k-\omega$ turbulence model, when used with $\gamma - Re_\theta$ transition

model by Menter, was able to predict a small separation bubble near the trailing edge, but the match with the experimental data on the pressure distribution was not satisfactory. Hybrid RANS/LES simulations have performed much better and show promise as a reliable tool for engineering applications.

In summary, the present results show how complex phenomena, which are beyond the reach of current turbulence models, can be described by DNS studies, but a major fundamental problem in the results is the dependence on resolution. It is possible that relatively low-resolution results have enough numerical noise that they will trigger phenomena like separation bubbles and transitions, in cases where the higher resolution simulation, presumably with lower numerical noise, would not contain such phenomena. There is a corresponding need for much more detailed experimental data on BL flows on gas turbine blades over a range of Reynolds numbers and well-characterized disturbance environments, so that it can provide benchmarks for DNS calculations.

7.2 Future Work

The present work has opened up several questions that require further investigation. The major ones among these are

- Dependence of solutions on resolution. Effect of FSTI and wake
- Curvature effects on laminar and turbulent boundary layers
- Detailed comparisons with RANS / LES results, with possible suggestions on aspects that need further improvement
- A reliable and extensive experimental dataset that can address the above questions with more confidence

References

ALLANEAU, Y. & JAMESON, A. 2009 Direct numerical simulations of a two-dimensional viscous flow in a shocktube using a kinetic energy preserving scheme. *AIAA paper 2009* **3797**.

ALLANEAU, Y. & JAMESON, A. 2010 Direct numerical simulations of plunging airfoils. In *48th AIAA Aerospace Sciences Meeting Including the New Horizons Forum and Aerospace Exposition, AIAA Paper*, , vol. 728.

BHASKARAN, B. 2010 Large eddy simulation of high pressure turbine cascade. PhD thesis.

BLAISDELL, G., SPYROPOULOS, E. & QIN, J. 1996 The effect of the formulation of nonlinear terms on aliasing errors in spectral methods. *Applied Numerical Mathematics* **21** (3), 207–219.

BLAZEK, J. 2005 *Computational Fluid Dynamics: Principles and Applications:(Book with accompanying CD)*. Elsevier.

BOURASSA, C. & THOMAS, F. 2009 An experimental investigation of a highly accelerated turbulent boundary layer. *Journal of Fluid Mechanics* **634**, 359–404.

BRADSHAW, P. 1977 Compressible turbulent shear layers. *Annual Review of Fluid Mechanics* **9** (1), 33–52.

CHAKRAVARTHY, S. 1999 A unified-grid finite volume formulation for computational fluid dynamics. *International journal for numerical methods in fluids* **31** (1), 309–323.

CHOI, J., TENG, S., HAN, J.-C. & LADEINDE, F. 2004 Effect of free-stream turbulence on turbine blade heat transfer and pressure coefficients in low reynolds number flows. *International Journal of Heat and Mass Transfer* **47** (14 - 16), 3441–3452.

COLEMAN, G. N., KIM, J. & MOSER, R. D. 1995 A numerical study of turbulent supersonic isothermal-wall channel flow. *Journal of Fluid Mechanics* **305**, 159–183.

COLES, D. 1956 The law of the wake in the turbulent boundary layer. *Journal of Fluid Mechanics* **1** (02), 191–226.

DAVIDSON, P. 2015 *Turbulence: an introduction for scientists and engineers*. Oxford University Press, USA.

DEVENPORT, W. J. & SCHETZ, J. A. 1998 Boundary layer codes for students in java. *ASME Fuids Engineering* .

DHAWAN, S. & NARASIMHA, R. 1958 Some properties of boundary layer flow during the transition from laminar to turbulent motion. *Journal of Fluid Mechanics* **3** (04), 418–436.

DIWAN, S., CHETAN, S. & RAMESH, O. 2006 On the bursting criterion for laminar separation bubbles. In *IUTAM Symposium on Laminar-Turbulent Transition*, pp. 401–407. Springer.

DUCROS, F., FERRAND, V., NICOUD, F., WEBER, C., DARRACQ, D., GACHERIEU, C. & POINSOT, T. 1999 Large-eddy simulation of the shock/turbulence interaction. *Journal of Computational Physics* **152** (2), 517–549.

EMMONS, H. W. 2012 The laminar-turbulent transition in a boundary layer-part i. *Journal of the Aeronautical Sciences* .

FEDOSEYEV, A. I. 2001 A regularization approach to solving the navier–stokes equations for problems with boundary layer. In *Proc. Eighth Int. Symp. on Computational Fluid Dynamics 1999*, pp. 317–324.

FRINK, N. T. 1994 Recent progress toward a three-dimensional unstructured navier-stokes flow solver. In *AIAA, Aerospace Sciences Meeting & Exhibit, 32 nd, Reno, NV*.

GARAI, A., DIOSADY, L., MURMAN, S. & MADAVAN, N. 2015 Dns of flow in a low-pressure turbine cascade using a discontinuous-galerkin spectral-element method. In *ASME Turbo Expo 2015: Turbine Technical Conference and Exposition*, pp. V02BT39A023–V02BT39A023. American Society of Mechanical Engineers.

GASTER, M. 1969 *The structure and behaviour of laminar separation bubbles*. Citeseer.

HERBERT, T. 1984 Analysis of the subharmonic route to transition in boundary layers. In *AIAA, Aerospace Sciences Meeting*, , vol. 1.

HILLEWAERT, K. 2012 Direct numerical simulation of the taylor-green vortex at Re = 1600, 2nd international high order cfd workshop. On the WWW. http://www.as.dlr.de/hiocfd/.

HIRSCH, C. 1988 Numerical computation of internal and external flows. *Wiley series in numerical methods in engineering* .

HODSON, H. & HOWELL, R. 2007 The role of transition in high lift low pressure turbines. *LECTURE SERIES-VON KARMAN INSTITUTE FOR FLUID DYNAMICS* **2**, 3.

HODSON, H. P. & HOWELL, R. J. 2005 Bladerow interactions, transition, and high-lift aerofoils in low-pressure turbines. *Annu. Rev. Fluid Mech.* **37**, 71–98.

HOLMES, D., CONNELL, S. & ENGINES, G. A. 1989 *Solution of the 2D Navier-Stokes equations on unstructured adaptive grids*. American Institute of Aeronautics and Astronautics.

HONEIN, A. E. & MOIN, P. 2004 Higher entropy conservation and numerical stability of compressible turbulence simulations. *J. Comput. Phys.* **201** (2), 531–545.

JAHANMIRI, M. 2011 Boundary layer transitional flow in gas turbines. http://publications.lib.chalmers.se/records/fulltext/136590.pdf.

JAMESON, A. 2008 Formulation of kinetic energy preserving conservative schemes for gas dynamics and direct numerical simulation of one-dimensional viscous compressible flow in a shock tube using entropy and kinetic energy preserving schemes. *J. Sci. Comput.* **34** (2), 188–208.

VON KAENEL, R. 2003 Large-eddy simulation of compressible flows using the finite-volume method. PhD thesis, Diss., Technische Wissenschaften ETH Zürich, Nr. 15255, 2003.

KALITZIN, G., WU, X. & DURBIN, P. A. 2003 Dns of fully turbulent flow in a lpt passage. *International Journal of Heat and Fluid Flow* **24** (4), 636–644.

KARYPIS, G. & KUMAR, V. 1998 A fast and high quality multilevel scheme for partitioning irregular graphs. *SIAM Journal on scientific Computing* **20** (1), 359–392.

KEHINDE, A. 2003 Analysis of effects of upstream turbulence of on aircraft engine turbine blades. PhD Thesis, State University of New York at Stony Brook.

KIM, J., MOIN, P. & MOSER, R. 1987 Turbulence statistics in fully developed channel flow at low reynolds number. *Journal of fluid mechanics* **177**, 133–166.

KLEBANOFF, P., TIDSTROM, K. & SARGENT, L. 1962 The three-dimensional nature of boundary-layer instability. *Journal of Fluid Mechanics* **12** (01), 1–34.

L HILGENFELD, P STADTMÜLLER, L. F. 2003 Experimental investigation of turbulence influence of wake passing on the boundary layer development of highly loaded turbine cascade blades. *Flow, turbulence and combustion* **69**, 229–247.

LAGRAFF, J. E. 2007 Minnowbrook-I 1993 workshop on end-stage boundary layer transition .

LAGRAFF, J. E. & ASHPIS, D. E. 1998 Minnowbrook-II 1997 workshop on boundary layer transition in turbomachines .

LANGTRY, R. B. & MENTER, F. R. 2009 Correlation-based transition modeling for unstructured parallelized computational fluid dynamics codes. *AIAA journal* **47** (12), 2894–2906.

LIU, X. & RODI, W. 1994*a* Surface pressure and heat transfer measurements in a turbine cascade with unsteady oncoming wakes. *Experiments in fluids* **17** (3), 171–178.

LIU, X. & RODI, W. 1994*b* Velocity measurements of wake-induced unsteady flow in a linear turbine cascade. *Experiments in Fluids* **17** (1-2), 45–58.

MAHESH, K., CONSTANTINESCU, G. & MOIN, P. 2004 A numerical method for large-eddy simulation in complex geometries. *Journal of Computational Physics* **197** (1), 215–240.

MALKIEL, E. & MAYLE, R. 1995 Transition in a separation bubble. In *ASME 1995 International Gas Turbine and Aeroengine Congress and Exposition*, pp. V001T01A003–V001T01A003. American Society of Mechanical Engineers.

MARCINIAK, V., KÜGELER, E. & FRANKE, M. 2010 Predicting transition on low-pressure turbine profiles. In *V European Conference on Computational Fluid Dynamics (ECCOMAS CFD 2010), Lisbon, Portugal, June*, pp. 14–17.

MAYLE, R. E. 1991 The 1991 igti scholar lecture: The role of laminar-turbulent transition in gas turbine engines. *Journal of Turbomachinery* **113** (4), 509–536.

MICHELASSI, V., CHEN, L.-W., PICHLER, R. & SANDBERG, R. D. 2015 Compressible direct numerical simulation of low-pressure turbines—part ii: Effect of inflow disturbances. *Journal of Turbomachinery* **137** (7), 071005.

MICHELASSI, V., WISSINK, J. & RODI, W. 2002 Analysis of dns and les of flow in a low pressure turbine cascade with incoming wakes and comparison with experiments. *Flow, Turbulence and Combustion* **69**, 295–329.

MORINISHI, Y., LUND, T., VASILYEV, O. & MOIN, P. 1998 Fully conservative higher order finite difference schemes for incompressible flow. *Journal of computational physics* **143** (1), 90–124.

MUKUND, R., NARASIMHA, R., VISWANATH, P. & CROUCH, J. 2012 Multiple laminar-turbulent transition cycles around a swept leading edge. *Experiments in fluids* **53** (6), 1915–1927.

NARASIMHA, R. 1985 The laminar-turbulent transition zone in the boundary layer. *Progress in Aerospace Sciences* **22**, 29–80.

NARASIMHA, R. 1991 The dynamics of the transition zone & its modelling boundary layers in turbomachines. Lecture Notes, von Karman Institute for Fluid Dynamics.

NARASIMHA, R. & DEY, J. 1989 Transition-zone models for 2-dimensional boundary layers: A review. *Sadhana* **14** (2), 93–120.

NARASIMHA, R. & OJHA, S. 1967 Effect of longitudinal surface curvature on boundary layers. *Journal of Fluid Mechanics* **29** (01), 187–199.

NARASIMHA, R. & SREENIVASAN, K. 1973 Relaminarization in highly accelerated turbulent boundary layers. *Journal of Fluid Mechanics* **61** (03), 417–447.

NOGUEIRA, X., CUETO-FELGUEROSO, L., COLOMINAS, I., GÓMEZ, H., NAVARRINA, F. & CASTELEIRO, M. 2009 On the accuracy of finite volume and discontinuous galerkin discretizations for compressible flow on unstructured grids. *International Journal for Numerical Methods in Engineering* **78** (13), 1553–1584.

ÖZTÜRK, B. & SCHOBEIRI, M. 2007 Effect of turbulence intensity and periodic unsteady wake flow condition on boundary layer development, separation, and reattachment along the suction surface of a low-pressure turbine blade. *Journal of fluids engineering* **129** (6), 747–763.

PATANKAR, S. V. & SPALDING, D. B. 1968 *Heat and mass transfer in boundary layers*. Morgan-Grampian.

POINSOT, T. J. & LELE, S. K. 1992 Boundary conditions for direct simulations of compressible viscous flows. *Journal of Computational Physics* **101**, 104–129.

RAI, M. M. 2011 A direct numerical simulation of flow through a low pressure turbine stage. http://arc.aiaa.org/doi/pdf/10.2514/6.2011-3092.

RANJAN, R., DESHPANDE, S. & NARASIMHA, R. 2013 Numerical methodology for simulating flows over turbine blades. In *Proceedings of 14th Asian Congress of Fluid Mechanics (ACFM)*, , vol. 2, pp. 515–521.

RANJAN, R., DESHPANDE, S. & NARASIMHA, R. 2014 Direct numerical simulation of compressible flow past a low pressure turbine blade at high incidence. In *ASME 2014 4th Joint US-European Fluids Engineering Division Summer Meeting collocated with the ASME 2014 12th International Conference on Nanochannels, Microchannels, and Minichannels*, pp. V01AT02A010–V01AT02A010. American Society of Mechanical Engineers.

RANJAN, R., DESHPANDE, S. & NARASIMHA, R. 2016 A high-resolution compressible dns study of flow past a low-pressure gas turbine blade. In *Advances in Computation, Modeling and Control of Transitional and Turbulent Flows*, chap. 28, pp. 291–301. World Scientific.

RAUSCH, R. D., BATINA, J. T. & YANG, H. T. 1992 Spatial adaptation of unstructured meshes for unsteady aerodynamic flow computations. *AIAA journal* **30** (5), 1243–1251.

REED, H. L. 1985 Anon p. 209.

RINALDI, E., RASPOPOV, R. S., COLONNA, P. & PECNIK, R. 2014 Modeling curvature effects on turbulence transition for turbomachinery flows. In *ASME Turbo Expo 2014: Turbine Technical Conference and Exposition*, pp. V02BT39A039–V02BT39A039. American Society of Mechanical Engineers.

SANDBERG, R. D., MICHELASSI, V., PICHLER, R., CHEN, L. & JOHNSTONE, R. 2015 Compressible direct numerical simulation of low-pressure turbines—part i: Methodology. *Journal of Turbomachinery* **137** (5), 051011.

SARKAR, S. 2007 Effects of passing wakes on a separating boundary layer along a low-pressure turbine blade through large-eddy simulation. *Proceedings of the Institution of Mechanical Engineers, Part A: Journal of Power and Energy* **221** (4), 551–564.

SARKAR, S. 2008 Identification of flow structures on a lp turbine blade due to periodic passing wakes. *Journal of Fluids Engineering* **130** (6), 061103.

SARKAR, S. 2009 Influence of wake structure on unsteady flow in a low pressure turbine blade passage. *Journal of turbomachinery* **131** (4), 041016.

SARKAR, S. & VOKE, P. R. 2006 Large-eddy simulation of unsteady surface pressure over a low-pressure turbine blade due to interactions of passing wakes and inflexional boundary layer. *Journal of turbomachinery* **128** (2), 221–231.

SCHETZ, J. A. 1993 Boundary layer analysis. *NASA STI/Recon Technical Report A* **93**.

SCHUBAUER, G. B. & KLEBANOFF, P. 1956 Contributions on the mechanics of boundary-layer transition .

SHAN, H., JIANG, L. & LIU, C. 2005 Direct numerical simulation of flow separation around a naca 0012 airfoil. *Computers & fluids* **34** (9), 1096–1114.

SHISHKIN, G. I. 1997 On finite difference fitted schemes for singularly perturbed boundary value problems with a parabolic boundary layer. *Journal of Mathematical Analysis and Applications* **208** (1), 181–204.

SHOEYBI, M., SVÄRD, M., HAM, F. E. & MOIN, P. 2010 An adaptive implicit-explicit scheme for the dns and les of compressible flows on unstructured grids. *J. Comput. Phys.* **229** (17), 5944–5965.

SHU, C.-W. & OSHER, S. 1988 Efficient implementation of essentially non-oscillatory shock-capturing schemes. *Journal of Computational Physics* **77** (2), 439–471.

SOD, G. A. 1978 A survey of several finite difference methods for systems of nonlinear hyperbolic conservation laws. *Journal of Computational Physics* **27**, 1–31.

SPALART, P. R. 2015 Philosophies and fallacies in turbulence modeling. *Progress in Aerospace Sciences* **74**, 1–15.

SPALART, P. R. & ALLMARAS, S. R. 1992 A one-equation turbulence model for aerodynamic flows .

SPALART, P. R., STRELETS, M. K. & GARBARUK, A. 2011 Grid design and the fate of eddies in external flows. In *Quality and Reliability of Large-Eddy Simulations II*, pp. 253–267. Springer.

STADTMULLER, P. 2002*a* Investigation of wake-induced transition on the LP turbine cascade T106A-EIZ. *Tech. Rep.*.

STADTMULLER, P. 2002*b* Investigation of wake-induced transition on the LP turbine cascade T106D-EIZ. *Tech. Rep.*.

STIEGER, R. & HODSON, H. 2004 The transition mechanism of highly loaded low-pressure turbine blades. *Journal of Turbomachinery* **126** (4), 536–543.

STIEGER, R. & HODSON, H. 2005 The unsteady development of a turbulent wake through a downstream low-pressure turbine blade passage. *Journal of Turbomachinery* **127** (2), 388–394.

STIEGER, R., HOLLIS, D. & HODSON, H. 2003 Unsteady surface pressures due to wake induced transition in a laminar separation bubble on a lp turbine cascade. In *ASME Turbo Expo 2003, collocated with the 2003 International Joint Power Generation Conference*, pp. 927–935. American Society of Mechanical Engineers.

SUBBAREDDY, P. K. & CANDLER, G. V. 2009 A fully discrete, kinetic energy consistent finite-volume scheme for compressible flows. *Journal of Computational Physics* **228** (5), 1347–1364.

SUNDARESAN, S., NAGARAJAN, S., DESHPANDE, S. & NARASIMHA, R. 1998 2d lid-driven cavity flow at high reynolds numbers: some interesting fluid-dynamical issues. In *Sixteenth International Conference on Numerical Methods in Fluid Dynamics*, pp. 231–236. Springer.

SUTHERLAND, W. 1893 Lii. the viscosity of gases and molecular force. *The London, Edinburgh, and Dublin Philosophical Magazine and Journal of Science* **36** (223), 507–531.

TURNER, A. B. 1971 Local heat transfer measurements on a gas turbine blade. *Journal of Mechanical Engineering Science* **13** (1), 1–12.

VAN DYKE, M. 1962 Higher approximations in boundary layer theory. *J. Fluid Mech.* **14**, 161–177.

VENEMA, L., VON TERZI, D., BAUER, H.-J. & RODI, W. 2011 Dns of heat transfer increase in a cylinder stagnation region due to wake-induced turbulence. *International Journal of Heat and Fluid Flow* **32** (3), 492–498.

VOLINO, R. 2002*a* Separated flow transition under simulated low-pressure turbine airfoil conditions: Part 1—mean flow and turbulence statistics. *ASME Journal of Turbomachinery* **124**, 545–655.

VOLINO, R. 2002*b* Separated flow transition under simulated low-pressure turbine airfoil conditions: Part 2—turbulence spectra. *ASME Journal of Turbomachinery* **124**, 656–664.

VOLINO, R. 2003 Passive flow control on low-pressure turbine airfoils. *ASME Journal of Turbomachinery* **125**, 754–764.

VON KÁRMÁN, T. 1931 Mechanical similitude and turbulence .

WANG, Y., CHEN, F., LIU, H. & CHEN, H. 2014 Large eddy simulation of unsteady transitional flow on the low-pressure turbine blade. *Science China Technological Sciences* **57** (9), 1761–1768.

WEI, L. & POLLARD, A. 2011 Direct numerical simulation of compressible turbulent channel flows using the discontinuous galerkin method. *Computers & Fluids* **47** (1), 85–100.

WILSON, D. & POPE, J. 1954 Convective heat transfer to gas turbine blade surfaces. *Proceedings of the Institution of Mechanical Engineers* **168** (1), 861–876.

WISSINK, J. 2003 Dns of separating, low reynolds number flow in a turbine cascade with incoming wakes. *International Journal of Heat and Fluid Flow* **24** (4), 626–635.

WISSINK, J. & RODI, W. 2006 Direct numerical simulations of transitional flow in turbomachinery. *Journal of turbomachinery* **128** (4), 668–678.

WISSINK, J. & RODI, W. 2008 Numerical study of the near wake of a circular cylinder. *International Journal of Heat and Fluid Flow* **29** (4), 1060–1070.

WISSINK, J. & RODI, W. 2011 Heat transfer from the stagnation area of a heated cylinder at re(d)=140,000 affected by free-stream turbulence. *International Journal of Heat and Mass Transfer* **54** (11 - 12), 2535–2541.

WISSINK, J. G. & RODI, W. 2006 Direct numerical simulation of flow and heat transfer in a turbine cascade with incoming wakes. *Journal of Fluid Mechanics* **569**, 209–247.

WISSINK, J. G. & RODI, W. 2009 Dns of heat transfer in transitional, accelerated boundary layer flow over a flat plate affected by free-stream fluctuations. *International Journal of Heat and Fluid Flow* **30** (5), 930–938.

WISSINK, J. G. & RODI, W. 2011 Direct numerical simulation of heat transfer from the stagnation region of a heated cylinder affected by an impinging wake. *Journal of Fluid Mechanics* **669**, 64–89.

WISSINK, J. G., RODI, W. & HODSON, H. P. 2006 The influence of disturbances carried by periodically incoming wakes on the separating flow around a turbine blade. *International Journal of Heat and Fluid Flow* **27** (4), 721–729.

WU, X. & DURBIN, P. A. 2001 Evidence of longitudinal vortices evolved from distorted wakes in a turbine passage. *Journal of Fluid Mechanics* **446** (1), 199–228.

WU, X. & MOIN, P. 2009 Direct numerical simulation of turbulence in a nominally zero-pressure-gradient flat-plate boundary layer. *Journal of Fluid Mechanics* **630**, 5–41.

ZAKI, T. A., WISSINK, J. G., RODI, W. & DURBIN, P. A. 2010 Direct numerical simulations of transition in a compressor cascade: the influence of free-stream turbulence. *Journal of Fluid Mechanics* **665**, 57–98.

Appendix A

Platforms used for DNS

- Nalanda Cluster at JNCASR
  - 10 Tflops (peak)
  - 512 CPU Cores, 32 CPU Nodes
  - Each node has-
    - Dual Intel Xeon E5-2670 eight core processor at 2.6 GHz
    - 128 GB RAM
    - 500 GB storage
  - 1 GPU Node
- Platform: Param YUVA-II, C-DAC, Pune
  - 530 Tflops (peak)
  - 3600CPU + 27000 Co-Processors (MIC)
  - Each node has-
    - Dual octa-core 2.6 GHz Intel Xeon E5-2670 processors with dual 60-core Intel Xeon Phi 5110P co-processors
    - 64 GB RAM
- Platform: Supercomputer CSIR-4PI, Bangalore
  - 362 Tflops (peak)
  - 17408 CPU Cores, 1088 Nodes
  - Each node has-

* Dual Intel Xeon E5-2670 eight core processor at 2.6 GHz
* 65.5 GB RAM
* 300 GB storage

Appendix B

List of Publications and Presentations

In Collection

1. **Rajesh Ranjan**, S M Deshpande, Roddam Narasimha. "A high-resolution compressible DNS study of flow past a low-pressure gas turbine blade." *Advances in Computation, Modeling and Control of Transitional and Turbulent Flows*. Chapter 28, Pg. 291-301. doi:10.1142/9789814635165-0028

Conference Proceedings

International

2. **Rajesh Ranjan**, S M Deshpande, Roddam Narasimha. "Direct Numerical Simulation of Compressible Flow Past a Low Pressure Turbine Blade at High Incidence." *Proceedings of ASME 2014 4th Joint US-European Fluids Engineering Division Summer Meeting(FEDSM2014)*. doi:10.1115/FEDSM2014-21773

3. **Rajesh Ranjan**, S M Deshpande, Roddam Narasimha. "Numerical methodology for simulating flows over turbine blades." *Proceedings of 14th Asian Congress of Fluid Mechanics (14ACFM)*. Volume-2, Pg. 515-512, October 15 - 19, 2013, Hanoi and Halong, Vietnam

National

4. **Rajesh Ranjan**, S M Deshpande, Roddam Narasimha. “The Effects of Curvature on the Turbulent BoundaryLayer in Flow Past Turbine Blades.” *Proceedings of 16th CFD Annual Symposium (AeSICFD16)*. CP29, August 11-12, 2014, Bangalore, India

5. **Rajesh Ranjan**, S M Deshpande, Roddam Narasimha. “DNS of flow past a LPT blade.” *Proc. of 15th AeSI Annual CFD Symposium (AeSICFD15)*. CP03, Pg. 22-24, August 9-10, 2013, Bangalore, India

National Conferences and Workshops

6. **Rajesh Ranjan**, Prasanth P, S M Deshpande, Roddam Narasimha. “Two Challenging problems in CFD: Gas Turbine Blades and Cloud Flows." Invited talk, *Cutting Edge trends in CFD: Indian Efforts and Product Offerings*, October 29, 2015, AeroFi, Bangalore, India

7. **Rajesh Ranjan**, Prasanth P, S M Deshpande, Roddam Narasimha. “Cumulus Clouds and Turbine Blades: Fluid Dynamics Problems that demand Peta to Near-exa Computing.” *Scientific Applications on PARAM Yuva II, 2015*, January 8-9, 2015, C-DAC, Pune, India

Poster Presentations

8. **Rajesh Ranjan**, S M Deshpande, Roddam Narasimha. “ANUROOP: A new computational tool for tackling the ’fluid-dynamical zoo’ that resides on a gas-turbine blade." *JNCASR In-House Symposium*, January 04-06, 2015, Bangalore, India (Achieved best poster award)

9. **Rajesh Ranjan**, S M Deshpande, Roddam Narasimha. “Understanding flow past a Low pressure turbine blade". *TWAS ROCASA Regional Conference of Young Scientists on Recent Trends in Physical and Biological Sciences*, March 7-8, 2014, Bangalore, India

10. **Rajesh Ranjan**, S M Deshpande, and Roddam Narasimha. “Flow past a gas turbine blade as seen by DNS.” *Fluids days*, July 18-20, 2013, Bangalore, India